Tracked Ultrasound
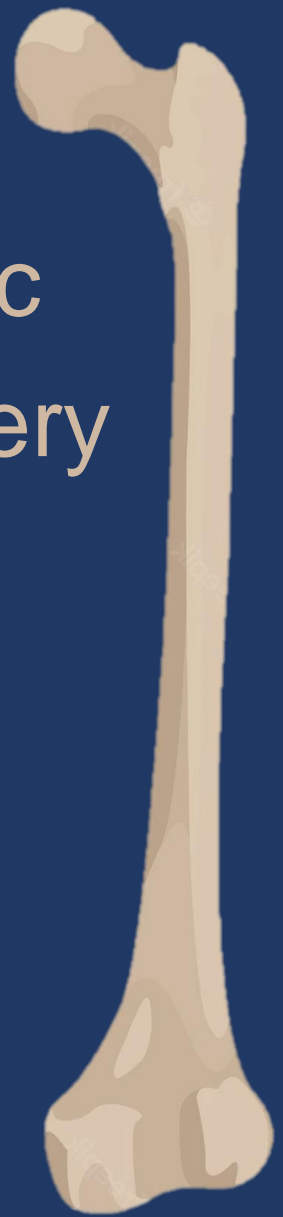
For

Pediatric Oncologic Image Guided Surgery

J.M. van der Zee

Master Thesis

Technical Medicine

21/03/2023

University of Twente   Princess Máxima Center

Master Thesis

Tracked Ultrasound: Towards Accurate Intraoperative Navigation During Pediatric Bone Tumor Resections with Soft tissue Components

J.M. van der Zee

A thesis submitted in partial fulfilment of the requirements

for the degree of Master of Science

in

Technical Medicine

Track: Medical Imaging and Interventions

Faculty of Science and Technology

UNIVERSITY OF TWENTE.

Princess máxima center
pediatric oncology

March 21, 2023

Graduation Committee

Chairman:

Prof. dr. ir. C.H. Slump
Department of Robotics and Mechatronics
University of Twente
Enschede, The Netherlands

First Clinical Supervisor

Prof. dr. M.H.W.A. Wijnen
Pediatric Oncologic Surgery
Princess Máxima Center for Pediatric Oncology
Utrecht, The Netherlands

Second Clinical Supervisor

dr. A.F.W. van der Steeg
Pediatric Oncologic Surgery
Princess Máxima Center for Pediatric Oncology
Utrecht, The Netherlands

Technical Supervisor

dr. F.J. Siepel
Department of Robotics and Mechatronics
University of Twente
Enschede, The Netherlands

Process Supervisor

E.M. Walter, MSc
Faculty of Science and Technology
University of Twente
Enschede, The Netherlands

Daily Supervisor

M. Fitski, MSc
Pediatric Oncologic Surgery
Princess Máxima Center for Pediatric Oncology
Utrecht, The Netherlands

External Member:

B. Wermelink, MSc
Multi-Modality Medical Imaging
University of Twente
Enschede, The Netherlands

Acknowledgement

Deze thesis vormt mijn inhoudelijke verdediging van mijn afstudeerstage op de afdeling kinderchirurgie in het Prinses Máxima Centrum, te Utrecht. Met het afronden van deze afstudeerstage hoop ik mijn studie Technische Geneeskunde met als specialisatierichting '*Medical Imaging and Interventions*' succesvol af te kunnen ronden.

Mijn studietraject begon in 2015 op de studie Biomedische Technologie na een afwijzing voor Technische Geneeskunde. In dat jaar heb ik lang getwijfeld over een nieuwe poging voor Technische Geneeskunde. Nu, bijna acht jaar na mijn afwijzing bij Technische Geneeskunde, rond ik mijn studie periode af en mag ik mij binnenkort officieel Technisch Geneeskundige noemen. In de zeven jaren dat ik over mijn studie heb gedaan, heb ik mij steeds meer kunnen ontwikkelen tot een toekomstig Technisch Geneeskundige. Dit heeft geresulteerd in mijn drive om de patiëntenzorg beter te maken door het inzetten van chirurgische navigatietechnieken tijdens en omtrent complexe operaties. Naast het ontdekken wat mij uniek maakt als toekomstig Technisch Geneeskundige, heb ik tijdens mijn studentenperiode meer geleerd over wat mijn kwaliteiten zijn en ben ik erachter gekomen wat ik het leukste vind om te doen.

De uiteindelijke ontwikkeling tot wie ik als persoon en als professional ben geworden heb ik gelukkig niet alleen hoeven te doen. In het afgelopen jaar heb ik de support mogen krijgen van mijn begeleiders, de onderzoeksgroep, de chirurgen van het Máxima, mijn intervisiegenoten en van mijn huisgenoten, vrienden en familie. Allereerst zou ik willen beginnen om Marc Wijnen en Lideke van der Steeg te bedanken voor de ruimte die ik tijdens mijn afstuderen van jullie heb gekregen om mijn eigen pad in te slaan en jullie hierin mee mocht nemen. Jullie hebben mij veel geleerd over het juist formuleren en richting geven van onderzoek met jullie klinische en academische kennis. Ik kijk nu al uit naar het vervolg. Daarbij wil ik Matthijs Fitski bedanken voor zijn begeleiding, zowel in het afgelopen jaar als tijdens mijn M2-stage. Ik wil je bedanken voor onze eindeloze spar-sessies, samen herschrijven van artikelen en jouw kritische meedenkende blik, maar ook het bewaren van een persoonlijke band. Ik wil Françoise Siepel bedanken voor onze fijne gesprekken op zowel persoonlijk als inhoudelijk vlak. Mede door deze gesprekken heb ik mijn eigen richting durven kiezen, waarbij jij toezag op de technische diepgang. Wat betreft mijn persoonlijke ontwikkeling wil ik Elyse Walter bedanken voor de fijne persoonlijke begeleiding gedurende mijn twee jaar aan stages. Ik heb tijdens de intervisies geleerd om kritisch naar mijzelf te kijken en waar nodig te relativeren. Tevens wil ik iedereen van de onderzoeksgroep 'Wijnen' bedanken voor de informele gesprekken bij de koffiemachine(-borrel), Máxima Retreats, de koffietjes van Iris, Barcelona, Winterberg en al onze vrijdagmiddagborrels. Ceder, Do, Rémi, Myrthe, Matthijs, Bernadette, Kevin, Rixt, Aranka, Elsie, Marett, Karleen, Koen en Tim ontzettend bedankt voor de leuke tijd.

Tenslotte wil ik mijn vrienden en familie bedanken voor jullie support en onvoorwaardelijke steun tijdens mijn studie en mijn afstuderen. Het waren de momenten waarbij ik in al mijn energie, stoom kon afblazen om vervolgens de boel weer met een frisse blik kon bekijken. Jullie zijn geweldig!

Aan allen, Bedankt!

Jasper van der Zee
Utrecht, maart 2023

Abstract

Purpose: Resection of pediatric osteosarcoma in the extremities with soft tissue involvement presents surgical challenges due to difficult visualization and palpation of the tumor. Therefore, an adequate image-guided surgery (IGS) system is required for accurate tumor resection. Ideally, an IGS system should be combined with a fast registration and re-registration methodology that minimal interrupts the surgical workflow. Moreover, the surgical decision-making may be enhanced with the use of a three-dimensional patient-specific model in combination with intraoperative tracked ultrasound (iUS). This study determines the surgical feasibility of an iUS-based IGS tool that incorporates the bone surface found with iUS as a new registration feature.

Methods: An automatic bone segmentation pipeline (Part I) and a surgical navigation system (Part II) were developed. Ultimately, the derived system was evaluated by pediatric surgeons (Part III). In Part II, a 3D model of the porcine lower limb was created based on preoperative scans. Second, the bone surface of the tibia was automatically detected (Part I) on an iUS acquisition. This acquisition was performed with a free-hand sweep over the skin. The bone surface of the preoperative 3D model was then matched with the bone surface detected by the iUS. To evaluate the registration accuracy, ten artificial surgical targets were used to calculate the target registration error (TRE). In Part III, the intraoperative performance of this surgical tool was evaluated by six pediatric surgeons and two pediatric oncologic orthopedists. The participants had to localize ten surgical targets to compute the point localization error (PLE). Finally, the user-experience was assessed with a post-procedural questionnaire.

Results: An automatic segmentation algorithm for bone segmentation was developed. Within the developed surgical system, a mean TRE of 6.78 mm (STD = 0.70 mm) and a median PLE of 8.00 mm (3.86 – 8.96 mm). The participated surgeons were more confident about their actions, and they experienced the localization as faster and easier concluding from the answers in the user-experience questionnaire.

Conclusion: This study indicates the potential and concept of an iUS-based registration methodology for an IGS system in a porcine cadaver study. Moreover, the participated surgeons and orthopedists were convinced of the clinical value of the interaction between the iUS and the 3D model.

Table of Content

List of Figures

List of Tables

List of Abbreviations

Abbreviation:	Definition:
OS	Osteosarcoma
MRI	Magnetic Resonance Imaging
CT	Computed tomography
WHO	World Health Organization
TNM	Tumor-node-metastasis
LRRC	Low recurrent rectal cancer
IGS	Image Guided Surgery
2D	Two-dimensional
3D	Three-dimensional
AR	Augmented reality
EM	Electromagnetic
CBCT	Cone-beam computed tomography
ORB	Optical reference body
US	Ultrasound
SOS	Speed of sound
iUS	Intraoperative tracked ultrasound
ICP	Iterative Closest Point
R1	Irradical
R0	Radical
DL	Deep learning
GAN	Generative adversarial network
NDI	Northern Digital Inc.
IMAR	Iterative Metal Artifact Reduction
RMS	Root-mean-square
TRE	Target Registration Error
PLE	Point Localization Error
IQR	Inter quartile range
STD	Standard deviation
ES	Ewing Sarcoma
HL	HoloLens
CNB	Core-needle biopsy

0

Purpose

"Hoe kan chirurgische navigatie de kinderchirurg helpen bij moeilijk vindbare tumoren?"

De oncologische kinderchirurgie is een belangrijk onderdeel binnen het gehele behandeltraject voor kinderen met kanker. Het hoofddoel van de chirurg is het geheel verwijderen van de tumor met zo min mogelijk schade aan omliggend gezond weefsel. Echter, deze balans tussen genezing en bijwerkingen kan erg moeilijk zijn als de tumor zich op een lastige plek in het lichaam bevindt, erg klein is of wanneer de tumor tijdens de operatie niet te voelen of te zien is. In sommige van deze gevallen kan de kinderchirurg de tumor niet in zijn geheel verwijderen. Dit kan leiden tot een zwaardere nabehandeling met cheomotherapie en/of bestraling en een verlaagde kans op uiteindelijke genezing.

Om deze tumoren beter te kunnen vinden, wordt er bij oncologische chirurgie voor volwassenen steeds vaker gebruik gemaakt van chirurgische navigatie. Bij volwassenen is aangetoond dat dit chirurgische hulpmiddel effectief is bij moeilijk vindbare tumoren. Zodoende worden deze tumoren nu effectiever en preciezer verwijderd. Echter, tonen de studies bij volwassenen ook limitaties aan van de gebruikte methode van chirurgische navigatie. Veelal wordt gebruik gemaakt van een CT-scanner in de operatiekamer, waardoor de initialisatie van de techniek lang kan duren en een eventuele noodzakelijke update van het systeem te omslachtig is. Tevens zijn de onderzochte technieken niet in staat om echografie te integreren in het navigatiesysteem. Ondanks de verbetering van minder positieve chirurgische snijranden en het makkelijker vinden van complexe tumoren, worden deze hulpmiddelen binnen de oncologische kinderchirurgie momenteel nog niet ingezet.

De aanleiding voor dit onderzoek is de ontwikkeling van een chirurgische navigatietechniek welke vervolgens in een klinische experimentele setting beoordeeld zal moeten worden. Hierbij wordt waar mogelijk gebruik gemaakt worden van echografie die de chirurg tijdens de operatie in staat stelt om zichzelf naar de tumor toe te navigeren middels 3D-modellen en beeldvorming. Uiteindelijk wordt verwacht dat de klinische implementatie van chirurgische navigatietechnieken in het Prinses Máxima Centrum, te Utrecht, de kinderchirurg zal helpen bij de chirurgische verwijdering van moeilijk vindbare tumor bij kinderen. Op termijn wordt verwacht dat de indicatie voor chemo- en/of radiotherapie na de ingreep minder vaak nodig is en de kans op eventuele terugkeer van de tumor zal verminderen. Uiteindelijk hopen wij betere overlevingskansen én een beter kwaliteit van leven te creëren bij deze specifieke patiëntengroep.

Afdeling Kinderchirurgie
Prinses Máxima Centrum
Utrecht

1

Introduction

1.1 Clinical Background

This section highlights the required clinical background.

1.1.1 Osteosarcoma

Osteosarcoma (OS) is a primary malignant bone tumor in children and young adults [1]. The annual incidence of OS is 8-11 cases per million at 10-19 years of age with an overall five-years survival rate between 50-66% in the Netherlands [1,2]. Rapid bone growth during second decade of life has a positive correlation with the development of OS and is commonly found near metaphyseal regions in the extremities with a preference for the proximal tibia, distal femur and proximal humerus. In approximately 64% of OS cases, the diseases is located around the knee, in 10% affecting the humerus and in a minority of cases in the pelvis [3].

Treatment options prior to the 1980s were deemed limited, with radical amputations as primary treatment. The introduction of multi-agent chemotherapy has improved the long-term survival of OS significantly. The five-years survival rates has increased from 10-20% up to 66%, with the introduction of the combination of chemotherapy and surgery [1,2,4,5]. Moreover, tumor mass reduction is achieved with chemotherapy and this improved local control achieved with surgery. This has led to a paradigm shift from radical amputations to more limb salvage treatments. Although treatment of OS has been improved in the last 40-years, accurate local control of the tumor poses challenges in the surgical management, especially if OS is present in the pelvis. Improved surgical treatment may improve the survival of OS even more, with primary non-metastatic OS at diagnoses.

The optimal surgical approach is determined based on local tumor extension and the involvement of neurovascular structures. The upcoming reconstruction will be defined through a shared decision-making process with the patients and their caregivers. Nowadays, limb salvage surgery is possible in ~90% of patients with OS in the extremities, although amputation sometimes remains the best surgical option for local control of OS.

1.1.2 Diagnosis and Oncological Staging

Patients with OS present with swelling that may cause movement limitations, especially if the disease is presented around the joints. In osteolytic disease, oncological fractures may occur, which often is the first clinical sign of OS. Imaging acquisition is performed after these patients are referred to the hospital. A fluoroscopy is often made and may show osseous changes of the bone. With a positive indication for OS, proven on first imaging, a magnetic resonance imaging (MRI) will be made. MRI is currently the best image modality to define soft tissue components of the tumor as well as the involvement and relation to the nerves, arteries and veins. Information about bone involvement, and skip lesions, can be provided by a computed tomography (CT) scan. [2,6]
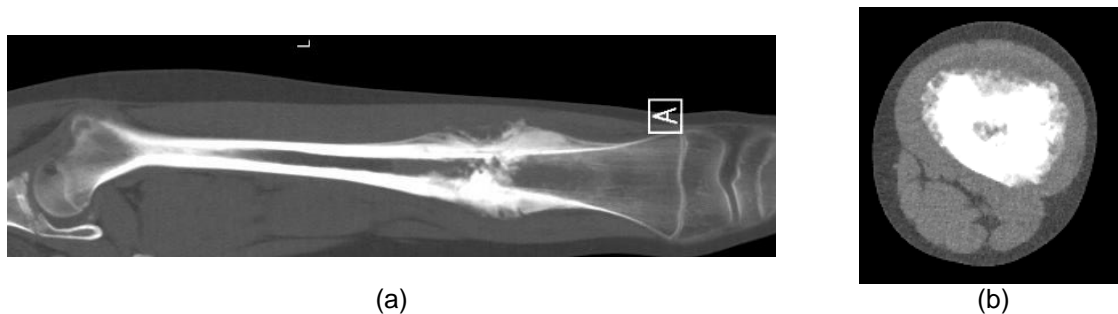
Figure 1: Radiological appearance of Osteosarcoma with soft tissue components in the distal femur shown an (a) transversal and (b) axial view on CT

Patients with a radiological indication for OS are referred to a patient-specific sarcoma institute. Pediatric patients in The Netherlands are therefore referred to the Princess Máxima Center for their final diagnosis and upcoming treatment. In addition to the radiological findings, biopsy will be performed for pathological staging of the disease. The radiologist or pediatric surgeon performs a biopsy that can be either a core-needle biopsy or a biopsy acquired during an open procedure. A core-needle biopsy is the preferred choice as potential contamination of surrounding tissue is minimized. Consequently, tumor tissue sampling should be performed carefully as tissue contamination could result in local recurrence. Therefore, the location of the biopsy is marked and the biopsy whole tract must be removed during upcoming surgery.

Histopathological staging of OS is divided into six subtypes according to the World Health Organization (WHO) 2020 classification: low-grade OS, OS not otherwise specified, parosteal, periosteal, high-grade surface OS and secondary OS [1]. Subsequently, based on the primary component of the found matrix OS can be classified as osteoblastic, condroblastic and fibroblastic according to the same WHO 2020 Classification. High-grade OS is mostly found in pediatric patients.

Presence of metastatic disease is assessed with a CT scan and a nuclear ^{99m}Tc positron emission tomography scan. Metastatic disease decreases the event-free and overall survival rate of OS. Subsequently, in case of pulmonary metastasis, a mastectomy could be indicated. Together with the pathohistological staging and the primary radiological review a tumor-node-metastasis (TNM) classification is defined as shown in Table 1 [7]. Following the TNM tumor classification and the histopathological findings, tumor staging is required and the staging classification can be found in Table 2 [7].
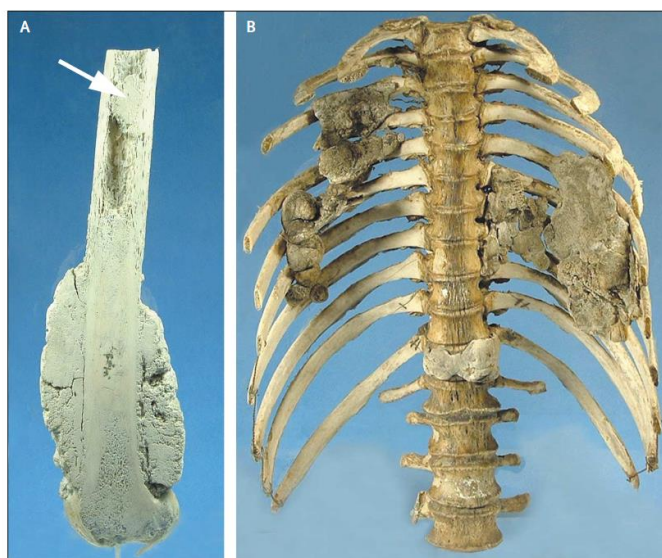
Figure 2: Postmortem preserved patient material. (a) Osteosarcoma in the distal femur with a skip lesion indicated by the white arrow. (b) Metastatic disease showing pleural and lung metastasis. [8]

Table 1: Tumor-Node-Metastic (TNM) classification of Osteosarcoma.

Tx	Primary tumor cannot be assessed
T0	No evidence of primary tumor
T1	Tumor ≤8 cm in greatest dimension
T2	Tumor >8 cm in greatest dimension
T3	Discontinuous tumor in the primary bone site
NX	Regional lymph nodes cannot be assessed
N1	No regional lymph node metastasis
MX	Distant metastasis cannot be assessed
M0	No distant metastases
M1	Distant metastases
M1a	Lung
M1b	Other distant sites

Table 2: Osteosarcoma tumor stage classification according to the World Health Organization.

Stage IA	T1	N0	M0	Low grade
Stage IB	T2	N0	M0	Low grade
Stage IA	T1	N0	M0	High grade
Stage IA	T2	N0	M0	High grade
Stage IA	T3	N0	M0	Any grade
Stage III	Any T	N0	M1a	Any grade
Stage IVA	Any T	N1	Any M	Any grade
Stage IVB	Any T	Any N	M1b	Any grade

1.1.3 Treatment

Treatment of pediatric OS in the Netherlands is in accordance with the Euromos-1 Treatment Protocol. This treatment protocol (shown in Figure 3) resulted from a multi-center international randomized study performed by a collaboration between different OS research groups: the North American Children's Oncologic Group, the German Austrian-Swiss Cooperative Osteosarcoma Study Group, the European Osteosarcoma Intergroup and the Scandinavian Sarcoma Group. Within this protocol, patients are treated with consecutive neoadjuvant chemotherapy, local therapy, adjuvant chemotherapy and if indicated postoperative radiotherapy. The main aim of neoadjuvant chemotherapy is the reduction of vital tumor mass and to prepare the surgical site for the local treatment.
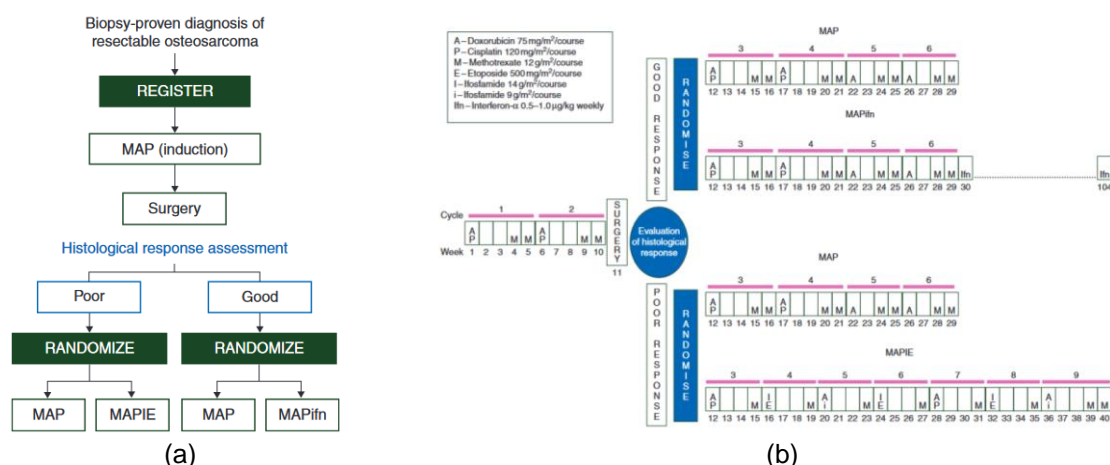
Figure 3: (a-b) Workflow of Euramos-1 treatment protocol.

Chemotherapy

Multi-agent chemotherapy is indicated for pre-treatment prior to surgery for OS. The most common chemotherapy protocol is a combination of doxorubicin, cisplatin and high-dose methotrexate (MAP)

[9]. The tumor response is closely monitored by the involved pediatric oncologist and treatment alterations may be indicated in case of poor tumor responses. Poor responses is classified if necrosis occurred in less than 90% of the tumor mass and thus a significantly part of the tumor remains vital on imaging. [10,11]

Local Therapy

The most optimal surgical option for the patient is always based on a shared decision between the oncologist and the orthopedist together with the patient and their caregivers. In this decision, the potential surgical outcome and the impacts on the quality of life are considered specified per treatment option. Importantly, each surgical option comes with a specific advantage and disadvantage that must be considered related to the patient's interest. Especially, if OS is diagnosed at time the child or adolescent is still growing, potential surgical options should compensate or anticipate on the expected growth. Managing of potential limb length discrepancy can be achieved with either an active grow endoprosthesis or an epiphysiodesis that stops the growth of the contralateral limb. In some localizations such as the distal tibia, a below-knee amputation is sometimes preferred for better functional outcome compared to technically reconstructions and arthrodesis which are technically demanding and do not guarantee a good functional outcome. Although complete tumor removal remains the cornerstone of local therapy, all potential surgical options should be considered and amputation was not related to improved survival compared to limb salvage options. [8]

Amputation

Amputation is considered as a radical treatment option, affecting the quality of life significantly. Nevertheless, amputation may be the best treatment option in some cases and children are able to adapt to the new situation rapidly. The child should be informed about possible prosthesis before and after surgery to regain limb functionality. Although artificial limbs are currently sophisticated, more proximal amputations are related to more discomfort comparing a below- and above-knee amputation. In case of non-limb amputation, the defect won't always be replaced for instance after the removal of a part of the pelvic or the removal of ribs.

Lim-salvage treatment: reconstruction

The options for limb-salvage treatment are various and the complete removal of the tumor and the tumor extent remains the most vital part of surgery. Therefore, wide surgical margins are required and states a resection margin of 3 cm for the osteotomy and 1-2 cm for the soft tissue, whenever possible [12]. However, this required resection margin poses challenges if the tumor is in close relation with critical structures. After the resection, reconstruction comes with different options based on either biological tissue, non-biological materials, or a combination of both.

This section describes a small selection for options for limb-salvage treatment specified for a distal femur tumor. Prosthesis are large metallic devices that are placed in the excised bone segment or even in the joint. Although a prosthesis replaces limb functionality and is not sensitive for chemotherapy, they are sensitive for infections and failure of the device requiring reinterventions [12]. Allografts are used either together with endoprosthesis and provides a biological replaced bone segment. The patient's own fibular is a well-chosen bone for allograft reconstruction and the combination with endoprosthesis will result in a reliable and stable reconstruction. Rotationplasty might be the most staggering option for reconstruction due to a high impact on the aesthetic appearance of a child [8]. This reconstruction removes the diseased portion of bone, shortens the lower leg, maintaining the neurovascular bundle and reattaches the lower limb in a 180º fashion to the proximal femur. In this way, the ankle joint now acts as knee joint and preserves a landing site for an artificial limb. Therewith, the child maintains function of the limb and even growth. Functional results of this reconstruction in active sports have been reported as promising and outweighs the results achieved with endoprosthesis devices [13]. Therefore, rotationality is considered to be one of the most preferred choices for the treatment of OS. [14,15]

Surgical Challenges

Although limb salvage surgery improves the patient's quality of life by maintaining the functionality of the limb, it can pose surgical challenges due to the need for negative resection margins. When these

margins are not achieved, the risk of local recurrence increases significantly [16]. Furthermore, when soft tissue components of the tumor are present, they are often difficult to visualize or palpate, which requires extensive preoperative surgical planning based on radiological imaging. Currently, more extensive surgical expertise is required due to a paradigm shift to more limb salvage treatment that may be more surgically challenging than radical amputation. Therefore, limb salvage surgery should outweigh the oncological potential of radical amputations. In addition, surgical challenges are present during arthrodesis and joint sparing surgery as the translation of the surgical planning may be difficult due to the limitation intraoperative surgical feedback. Therefore, the help of a surgical tool that gives real-time feedback of surgical actions related to the surgical planning could be clinically beneficial. Image-guided surgery (IGS) was first introduced in neurosurgery and is currently considered as standard care in the intraoperative aid in anatomical awareness for the neurosurgeon. Currently, IGS is introduced in other extra-cranial surgical disciplines such as abdominal and pelvic oncological surgery. These surgical tools could help overcome or minimize pediatric orthopedic oncologic surgical challenges.

1.1.4 Image Guided Surgery

Although intraoperative navigation in extra-cranial oncology surgery is upcoming in the last years, clinical evidence has been proven in a limited number of clinical studies in adult oncological extra-cranial surgery only, as shown in Table 3: Clinical outcome of navigated surgery on radical resection margins in adulthood oncological surgery.Table 3.

In adult abdominal oncological surgery, rectal cancer poses complex surgical challenges that lead to positive resection margins rates of 10-15% and a local recurrence rate of 6-10% after primary resection [17,18]. In case of locally recurrent rectal cancer (LRRC), surgical resection results in incomplete resection rates of 38-62% that subsequently decreases five-year survival five-folds. Therefore, the Netherlands Cancer Institute developed an abdominal surgical navigation system, as shown in Figure 4, which aids tumor localization. This navigation system was used during LRRC surgery which resulted in a higher complete resections rate in a navigated cohort (78.9%; 95% CI, 54.4%-94.0%) compared to a historical (48.8%; 95% CI, 32.9%-64.9%) cohort. Moreover, surgeons reported improved decisiveness and improved tumor localization with the aid of surgical navigation.

| (a) | (b) | (c) |
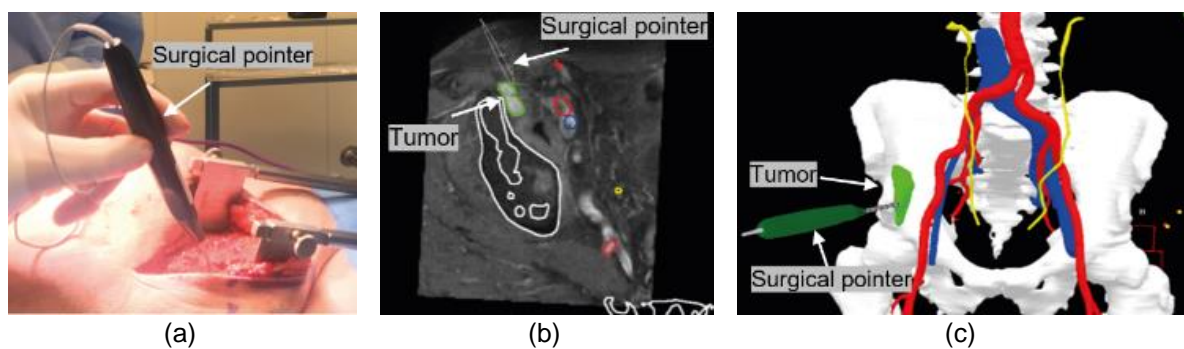
Figure 4: Surgical navigation system that aids in localization for complex resection of pelvic soft tissue. (a) In-vivo situation, real-time feedback in (b) 2D-imaging and (c) 3D-imaging. (Retrieved and adapted from Reijers et al. [19]).

In adult sarcoma surgery, resections of bone tumors with soft tissue extension are comparable to pediatric sarcomas concerning surgical challenges. Comparable to the results of abdominal image guided surgery, Bosma et al. reported more adequate resection margins (81% vs 50%) in pelvic and sacral sarcoma tumor resections with the aid of surgical navigation [20]. This observation was confirmed by Nanda et al. who reported an increased complete removal rate (73% vs 91%) in pelvic and sacral sarcoma resections with aid of surgical navigation [21].

Remarkable, the cited studies are sensitive to selection biases as the navigated group included more complex interventions compared to the non-navigated group in some studies. Therefore, the additional true clinical value of IGS might be underestimated in some of the cited studies. Although approximately 9% up to 31% resection margins were achieved, soft tissue navigation was deemed limited and further

improvement of surgical navigation is required. Potentially intraoperative real-time ultrasound combined with the navigation system could aid in the localization of these soft tissue components and improve radical resections even more.

Table 3: Clinical outcome of navigated surgery on radical resection margins in adulthood oncological surgery.

Malignancy	Anatomical Region	Authors	Radical (R0) resection rates		
			Non-Navigated Group	Navigated Group	Statistics
Bone Sarcoma	Pelvic and sacral [20]	Bosma et al. (2019)	50% (n = 34)	81% (n=36)	OR 4.14 [95% CI 1.43-12.01], p=0.03
Bone Sarcoma	Pelvic and sacral [21,22]	Nandra et al. (2019)	73% (n=539)	91% (n=23)	Not defined
Bone Sarcoma	Pelvic and Sacral [23]	Fujiwara et al. (2021)	81% (n=37)	92% (n=13)	Not defined
Bone Sarcoma	Pelvic and Sacral [24]	Latinen et al. (2017)	75% (n=12)	100% (n=9)	p = 0.383
Primary Rectal Cancer	Pelvic [25]	Kok et al. (2020)	84% (n=142)	93% (n=33)	P = 0.69
Local Recurrent Rectal Cancer	Pelvic [25]	Kok et al. (2020)	49% (n=41)	79% (n=19)	P = 0.047

1.1.5 Orthopedic Oncological Image Guided Surgery

Oncological surgical outcome in terms of overall-survival, event-free survival and the change of local recurrence is correlated with postoperative positive margins [16,26]. IGS has been proven to improve surgical precision in orthopedic surgery and oncological orthopedists would implement these surgical benefits for their clinical implementation [27]. Therefore, IGS could be used to improve oncological surgical precision with the aid of intraoperative guidance. However, the implementation of IGS in the surgical treatment of pediatric sarcoma in the Princess Máxima Center has not been done yet as it lacks on clinical evidence for this patient group. Nevertheless, IGS has proven its clinical relevance in the oncological surgical treatment for pelvic and extremities [28–32]. Within this evidence, mainly for the adult patient group, the surgical accuracy and thus patient outcome was improved. Especially, the aid of navigation techniques helps translating the surgical planning to the intraoperative decision-making. This may result in a positive effect on the paradigm shift to limb salvage surgery instead of amputation. This shift could result in an improvement of the quality-of-life of these young patients as they will preserve limb functionality.

1.1.6 Impact

Malignant bone sarcomas, Ewing Sarcoma, OS and Chondrosarcoma, are diagnosed in approximately 30 children in The Netherlands annually. These sarcomas potentially pose surgical challenges ensuring safe surgical margins for tumor extend in the soft tissue specifically. The introduction of novel intraoperative navigation system could help the surgeon during the accurate complete removal of the tumor. The use of navigation techniques in adulthood oncological surgery increased the radical resection rate from 9% up to 31%. Therefore, the implementation of surgical navigation should be considered for the surgical management of challenging OS tumor resections in this patient group.

Ideally, the novel surgical system should have a (1) fast and straightforward registration methodology, (2) accessible re-registration and (3) the combination of an intraoperative imaging tool combined with the preoperative 3D models for the localization of non-visible and non-palpable tumor extent. Altogether,

the surgical system should be easy in use with no unnecessary radiational harm to the patient and surgical team.

1.2 Technical Background

This section highlights the required technical background.

1.2.1 Visualization

Surgical navigation is widely used in neuro and orthopedic surgery workflows and relies on 2D display techniques. Preoperative imaging, in 2D, can be reconstructed to a 3D volume to obtain a 3D patient-specific model. This 3D model includes all anatomical information that the surgeon needs during surgical planning or surgery. During surgical navigation, this 3D model is shown on a 2D screen resulting in a 2D-3D model, accurate interpretation is reliant to the spatial capacity of the surgeon. In other words, the surgeon is aided by translating 2D imaging to a 3D model, but this remains to a 2D visualization. To overcome this 2D-3D switching problem a 3D glasses, known for the use in cinema's, could be added. However, the surgeon's depth perception could not be overcome solely by 3D glasses. Moreover, conventional visualization techniques (i.e., the 2D display) introduce a switching focus problem. Namely, the surgeon needs to physically switch between the surgical field and the 2D display. Altogether, the added clinical value of such techniques depends on the surgeon's 2D-3D spatial awareness translating the screen's navigational information into the surgical field.

To overcome the spatial 2D-3D and switching focus problems, augmented reality (AR) could be helpful. Within AR, 3D models can be projected while the surgeon maintains direct visual contact with the surgical field. Consequently, the surgeon will obtain a direct depth-perception of the used 3D models to obtain navigational guidance directly. This could result in a better translation of the surgical planning to intraoperative decision making, resulting in optimal resection margins with less tissue damage. However, the intraoperatively use of AR is deemed limited to technical and physical limitations. Technically, accurate feedback between the tracking system and the AR device is required. Moreover, the surgeon needs to wear the AR device that may not be physically practical throughout the surgery. Currently, the clinical use of the addition of AR to current surgical navigation techniques is limited as the technical and physical limitations should be solved before clinical implementation could occur. Therefore, using a 2D display above the surgical field is still preferable.

1.2.2 Tracking

Object tracking is an essential component during the translation of virtual 3D models to the physical patient location. For simplicity, surgical object tracking can be compared to the global positioning system in your mobile phone while driving your car to an unknown destination. Most probably you will use car navigation (e.g., "Google Maps") to obtain orientational feedback such as when to take the next exit or where the closest gas station is located. Therefore, your physical location is constantly tracked by a tracking system, in this case a satellite, which finds the location of your phone. Without your phone, the application will not be able to determine your physical location and the navigation becomes inaccurate. Ultimately, the navigational feedback can be personal adjusted to the user's needs.

Electromagnetic Tracking

Electromagnetic (EM) tracking consists of a low field generator that creates a magnetic field around the patient. In medical applications, a planar field generator is mostly used and placed underneath the patient. This generator creates a magnetic flux in the surgical field, measured by EM sensors attached to the patient and surgical tools. These sensors measure the received magnetic flux constantly and this defines the exact position and pose of the sensor in the EM field. However, as tracking depends on this magnetic flux, distortion of the magnetic field creates tracking inaccuracies. Therewith, the use of external ferromagnetic objects, oscillating saws, surgical tools and or ultrasound probes in the surgical field affects the tracking performance [33]. Different commercial EM tracking systems are available with the systems of NDI (Northern Digital Inc., Polaris Vega ST, Waterloo, Ontario, Canada) as the frequently used systems in navigated surgery. These EM tracking systems achieve positional accuracies between 0.70 and 1.20 mm [34].

Optical Tracking

Optical tracking combines stereo vision principles to obtain a stereo tactic input that can define the position and pose of objects relating to the reference frame of the optical tracker itself with high accuracy. Therefore, optical markers must be attached to physical objects and calibration has to be performed. These optical markers are retroflectors in a fixed spatial non-symmetric configuration consisting of 3 or more spheres. The optical tracking system emits infrared limit that are reflected to the tracking system by interference with these optical markers. Resulting in the ability to locate the individual spheres, that results in the localization of the object with the tracking of all involved spheres. Therefore, the optical tracking system should always keep a direct line-of-sight to the optical spheres. The integration of tracked tools requires calibration procedures. These calibration procedures are necessary for instance if the position or a pose of a specific location on the object is required. Different commercial optical tracking systems are available with the systems of NDI as the frequently used systems in navigated surgery. These optical tracking systems achieve accuracies of 0.045 mm and 0.09 mm for static or dynamic tracking, respectively [35]. Although optical tracking systems are known for high accuracies, the requirement for the direct line-of-sight might be considered as the main limitation.

Both tracking principles comes with different technical advantages and disadvantages, and these must be considered for the clinical application specifically. For this latter, an optical tracking system outweighs an EM tracking system in orthopedic surgery. Namely, external ferromagnetic tools and instruments are used during orthopedic surgery that might influence EM accuracy. Moreover, surgical accuracies reported in optical tracking are generally slightly better than in EM tracking [36,37]. Moreover, the fundamental advantage of EM tracking above optical tracking (i.e., line-of-sight limitation) won't apply for orthopedic extremity surgery. Nevertheless, in pelvic or abdominal surgery the limitation of optical tracking might become dominant and EM tracking could be preferable.

1.1.3 Conventional Surgical Navigation Workflow

The workflow for surgical navigation can be divided into the following surgical phases: preoperative planning, intraoperative preparation. In the Antoni van Leeuwenhoek Hospital, an electromagnetic surgical navigation system is developed and the whole workflow is shown in Figure 5 [38]. This workflow is comparable to other navigational workflows and requires the following procedures:

First, defining anatomical landmarks for registration as artery bifurcations, bone surface or other anatomical landmarks. Secondly, the 3D models are intraoperatively used to guide the surgeon to the anatomical region of interest. Surgical planning is done in collaboration with the surgeon to discuss which structures are required for the surgery such as critical structures, arteries, nerves or ureters, that should be avoided during surgery. Moreover, the combination of different image modalities could increase anatomical information in this surgical planning. Currently, most surgical navigation workflows require a cone-beam CT (CBCT) scan in the surgical planning due to excellent visibility for vessels and bone. However, the soft tissue appearance on MRI could be more beneficial for intraoperative use. Therefore, image registration between different image modalities combines the best of both worlds and could be beneficial for soft tissue localization.

The intraoperative preparation consists of patient registration. Within this phase, the derived digital surgical planning will be matched to the physical patient. Therefore, preoperatively defined anatomical structures, are matched with the same features found in the pre-incisional phase. In current workflows, a CBCT patient registration occurs that requires a pre-incisional CBCT acquisition. This includes the anatomical features present in the surgical planning and a patient reference body that the tracking system can find intraoperatively. For optical tracking, an optical reference body (ORB) is fixated into a rigid structure (i.e., bone), of the patient with two Kirschner wires. For electromagnetic tracking, an electromagnetic sensor can be placed either on the skin or in the same manner comparable to optical tracking.

The intraoperative guidance consists of the actual navigated surgery. The tracking system, either optical or electromagnetic, tracks the physical location of the patient and the surgical tools. The navigation system uses the computed transformation matrix, computed during the patient registration, to couple the actual live position of the patient with the surgical planning. Consequently, the surgeons can use the navigation with a tracked surgical tool suc as an ultrasound (US) probe, drill, saw or surgical pointer, in combination with the surgical plan (i.e., the preoperative derived patient-specific 3D model). Finally, the system gives intraoperative navigational feedback comparable to a laparoscopic intervention. The

performed patient registration should be robust although intraoperative positional change of the patient or patient reference is inevitable that affects the accuracy. Therefore, intraoperative re-registration is required to retrieve the desired clinical accuracy. This re-registration needs to be fast with minor interruption of the surgical workflow. Current patient registration methodologies, such as the CBCT registration, requires approximately 15 minutes interrupting the surgical workflow significantly [25]. Faster patient registration methods, or intraoperative updates of the current registration, are required for continuous usage of surgical navigation throughout surgery.
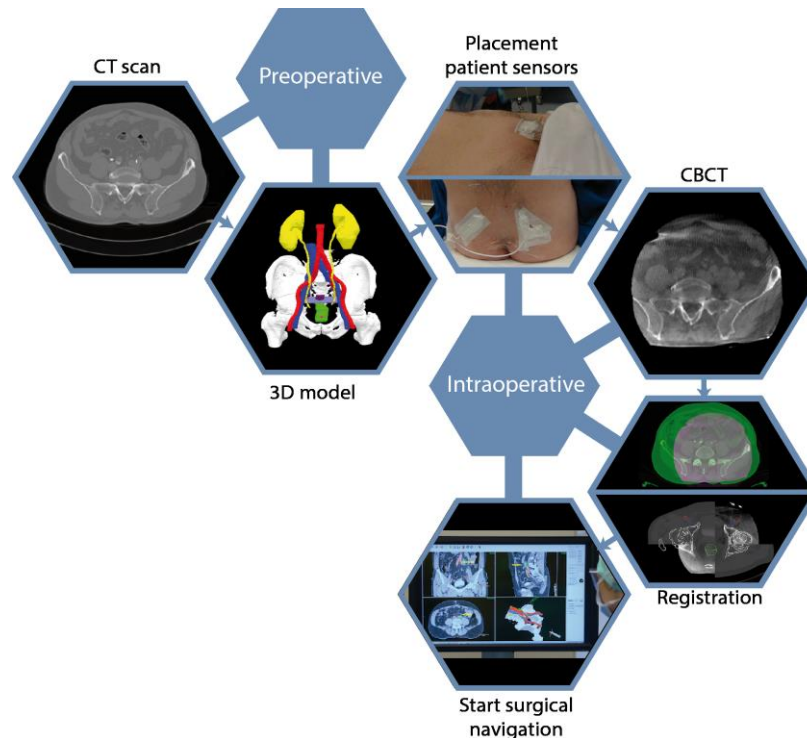
Figure 5: Surgical Navigation Workflow (Retreived from Noltes [38])

1.1.4 Limitations of Conventional Navigation

The CBCT patient registration is most often integrated in commercialized intraoperative navigation techniques. As a fact of the CBCT patient registration, the surgeon will be interrupted for approximately 15 minutes and the patient is being prepared for the CBCT acquisition [25]. Consequently, this conventional CBCT patient registration results in the following limitations [39]:

1. Extensive workflow interruption required for patient registration.

Initialization of the navigation system requires the setup of the whole system, including image acquisition with CBCT. The image acquisition involves the already sedated patient and the surgical staff should prepare the patient for acquisition. Therefore, the whole image acquisition interrupts the workflow of the surgeon and normal surgery can proceeded after succeeding the image acquisition. Ideally, image acquisition should be performed quickly without the interrupting the surgeon.

2. Fast and accessible re-registration, or update of current registration, cannot been performed.

Accurate navigation is required throughout the surgery, especially prior tumor resection. If registration takes place before the primary incision in the current surgical workflow and this might decrease the reliability of the system over time. If inaccuracies occur, the surgeon could not rely on the system and misinterpretation could therefore result in adverse surgical decision making. Moreover, two orthopedists of the Princess Máxima Center reported inaccurate navigation in their current clinical practice and remarked this as a major limitation of current navigational workflows. Ideally, a more straightforward system with less patient interaction is required to remain an accurate surgical system throughout the whole surgery. In current practice, the orthopedist decides to continue surgery without navigation, due to the extensive interruption for re-registration.

3. Radiation exposure for both the patient and potentially the surgical staff.

Image acquisition involves harmful radiation exposure for the patient and the surgical staff. Significantly more radiational exposure is used during a 3D CBCT than for a single fluoroscopy. Consequently, this requires more radiational precaution and the surgical team must leave the operating room during image acquisition and leaving the patient alone. Ideally, alternative imaging modalities without radiational exposure, such as US, are more practical in the surgical workflow, especially for pediatric patients.

4. No integration of other image modalities within the surgical system.

The surgical management of OS with soft tissue components requires the localization of both rigid and non-rigid tumor components. The rigid components, the bone tumor, can be accurately localized with surgical navigation due to minor tissue shifts between preoperative planning and the intraoperative situation. However, the soft tissue components are not completely fixated to rigid structures, causing tissue shifts. Therefore, the integration of real-time imaging, such as US, could be potentially helpful in the localization of this tumor extent, ensuring safe surgical margins.

To overcome these stated limitations, the implementation of tracked US could be of potential value for the improvement of conventional patient registration techniques. Therefore, the derived system ensures straightforward patient registrations together with real-time image acquisition combined with the 3D model during the actual surgery.

1.2.5 Tracked Ultrasound

US is considered as a bed-side imaging modality that is widely accessible in clinical routines. This image modality is preferable for clinical application requiring fast diagnostics and prevention of unnecessary radiational harm compared to CT. The physics behind US imaging are ultrasonic sound waves with frequencies above 20 kHz that can't be heard by human beings. These longitudinal sound waves are introduced into the patient and propagates differently for different tissues. Resulting in different transmissions and reflections due to tissue specific acoustic properties. For instance, if a homogeneous tissue attenuates a sound wave minimally, a low amount of energy loss due to scattering occurs resulting in low absorption and reflection and thus signal. Consequently, if the sound wave propagates trough different tissue types, with different acoustic properties and acoustic impedance's, the wave got scattered on the interference of one tissue to another. This interference reflects the sound wave that will be detected back by the probe. Thus, large acoustic impedance's differences will result in a large amount of scattering and a high signal. Moreover, the absorption fraction of the emitted sound wave is wave frequency dependent. High frequencies result in a high amount of absorption and thus wave energy loss and minor reflection can be detected by the transducer. Deep tissue imaging requires therefore a low frequency with minor absorption than image acquisitions of superficial structures that requires high frequency. [40,41]

Ultrasonic waves in US probes are produced by the vibration of piezoelectric crystals in the transducer that was first described by the French physicists Pierre and Jacques Curie in 1880. These ultrasonic sound waves are created by piezoelectric crystals in the transducer [40,41]. The emitted sound wave produced from one single transducer will eventually results in a single scan line. Resultingly, this single scan line is mostly plotted as the amplitude as function of the depth and this one-dimensional manner of acquisition is called A-mode. Unlike A-mode, the amplitude can be expressed as pixel intensity resulting in a brightness signal, called B-mode. Moreover, these reflected signals must be reconstructed to a B-mode image. Therefore, the speed of sound (SOS) of tissue is required to compute the depth of the reflected target [42]. Therefore, the depth (d) is computed with the measured time between propagation and reflection (t) multiplied with the SOS (s) divided by two:

$$d = t \cdot \frac{c}{2} \qquad (1)$$

In medical ultrasound imaging, the SOS is assumed to be 1540 m/s as the average in human tissue. Although this average SOS, different velocities are found for fat, muscles, and bone with SOS of 1450

m/s, 1600 m/s and 4080 m/s, respectively. Therewith, as the SOS in fat is lower than the fixed SOS by the US machine, sound is detected later than expected and the signal will be reconstructed deeper.

Tracked-US combines image acquisition with real-time pose and position tracking data. Resultingly, each frame is captured together with the position and pose of the probe during acquisition. This data acquisition, consisting of consecutive tracked 2D images, can be reconstructed to a 3D volume. The computed 3D volume of the total acquisition may now be compared or registered to other derived imaging data such as CT and MRI, which are conventionally captured in a 3D volume. Therefore, Tracked-US may be potential during patient registration as it is able to find rigid physical anatomical features on Tracked-US. A schematic diagram for tracked-US is shown in Figure 6. In case the data acquisition is performed inside the operating room, this technique is called intraoperative tracked-US (iUS).
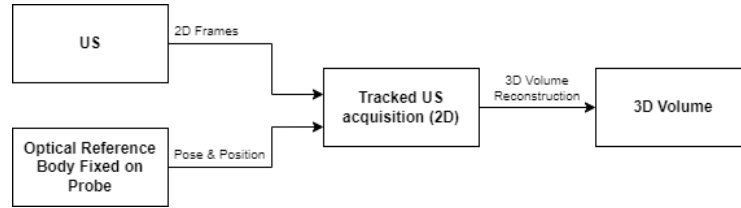
Figure 6: Schematic diagram for tracked-US

Ultrasound may serve as an alternative to the imaging modality for patient registration. Therefore, US based navigation system was first described in 2003 by Amin et al. [43]. The authors used the bone surface as registration feature. The bone surface was found with a tracked-US and used to register the preoperative CT with the intraoperative patient location. The proposed system resulted in an accuracy of 1.27 mm, which showed clinical potential accuracies.

1.2.6 Registration Techniques

The acquired IGS system requires constant tracking of several components such as patient, surgical pointer, US probe. An optical tracking system captures real-time the pose and positional data of the components, tracing the attached optical reference bodies. This tracking data acquisition is primarily expressed in the coordinate frame of the optical tracker. Transformation between two coordination frames requires both translation and rotation, shown in Figure 7a-b, respectively. The mathematical transformation between a coordination frame (A) to another (B), is expressed by a transformation matrix expressed by equation 2.

$$ {}^{B}T_{A} = \begin{bmatrix} {}^{B}R_{A} & {}^{B}t_{A} \\ 0 & 1 \end{bmatrix} \tag{2}$$

This matrix incorporates all translation ($ {}^{B}t_{A} $) and rotational ($ {}^{B}R_{A} $) operations required to express the position of tracked components to a coordination frame, shown in Figure 7c.

Translation, as shown in Figure 7a, describes the translation between two frames. Given the origin of frame A expressed in frame B, with the same orientation, the following definition can be described to express a point (**P**) from frame A (${}^{A}\mathbf{P}$) into frame B (${}^{B}\mathbf{P}$).

$$ {}^{B}t_{A} = \begin{bmatrix} {}^{B}t_{x} & {}^{B}t_{y} & {}^{B}t_{z} \end{bmatrix}^{T} $$
$$ {}^{B}\mathbf{P} = {}^{A}\mathbf{P} + {}^{B}t_{A} \tag{3}$$

Rotation, as shown in Figure 7b, describes the rotation between two frames. Given frame A expressed in the rotated frame B, with the origin located at the same location, the following definition can be described:

$$ \mathbf{x}_{A} = r_{xx}x_{B} + r_{xy}y_{B} + r_{xz}z_{B} $$
$$ y_{A} = r_{yx}x_{B} + r_{yy}y_{B} + r_{yz}z_{B} $$
$$ z_{A} = r_{zx}x_{B} + r_{zy}y_{B} + r_{zz}z_{B} \tag{4}$$

Resulting in the following matrix-vector notation:

$$\begin{bmatrix} x_A \\ y_A \\ z_A \end{bmatrix} = \begin{bmatrix} r_{xx} & r_{xy} & r_{xz} \\ r_{yx} & r_{yy} & r_{yz} \\ r_{zx} & r_{zy} & r_{zz} \end{bmatrix} \begin{bmatrix} x_B \\ y_B \\ z_B \end{bmatrix} = {}^B R_A \begin{bmatrix} x_B \\ y_B \\ z_B \end{bmatrix} \tag{5}$$

Therefore, the whole IGS system consist of several components primarily expressed in the optical tracker coordination frame. Therefore, the position of different components can be defined by each of these frames following:

$$^B\mathbf{P} = {}^B\mathbf{R}_A \,{}^A\mathbf{P} + {}^B t_A = {}^A\mathbf{P} \;\; {}^B T_A \tag{6}$$
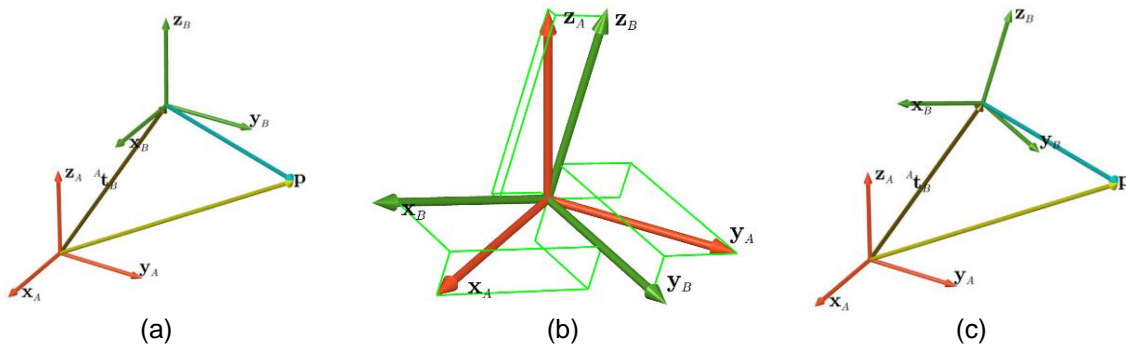
Figure 7 (a) Translation between frames A to B. (b) Rotation between A to B with respect to the same origin. (c) Transformation between frames A to B. (Retrieved from van der Heijden [44])

Iterative Closest Point Registration

During patient registration the link between the digital planning and the physical location of the patient is defined, to achieve intraoperative guidance as shown in Figure 4. Therefore, comparable features should be digitally found in the physical world to capture those linked to the physical position of the patient. Ultimately, registration allows for real-time guidance of surgical tools in the physical surgical field together with the preoperative derived 3D models.

Iterative Closest Point (ICP) algorithms are used to register two-point clouds together [45]. Therefore, the algorithm finds the best possible match of these point-clouds in an iterative manner, as shown in Figure 8a. Different transformations are iteratively estimated defining the most optimal match with minimal distance errors between the two point-clouds. This manner of registration is the commonly used rigid transformation algorithm to align 3D point-clouds together in a stable and robust manner [46,47]. In surgical application settings, the ICP registration method is used for patient registration in navigation strategies in neurosurgery. Therefore, the neurosurgeon will pinpoint anatomical landmarks, such as the nasion, with a tracked pointer that are correlated to registration landmarks on the 3D model. Patient registration is performed with the ICP registration linking the physical and digital points together. The bone surface is used for orthopedic applications and the ICP registration matches the two point-clouds representing the whole bone surface together as shown in Figure 8b. Although the ICP registration results in optimal results, the algorithm appears to be sensitive to outliers and converging to local optimal solutions [47]. Therefore, optimization procedures could be indicated to obtain an even more accurate registration [48].

(a)   (b)
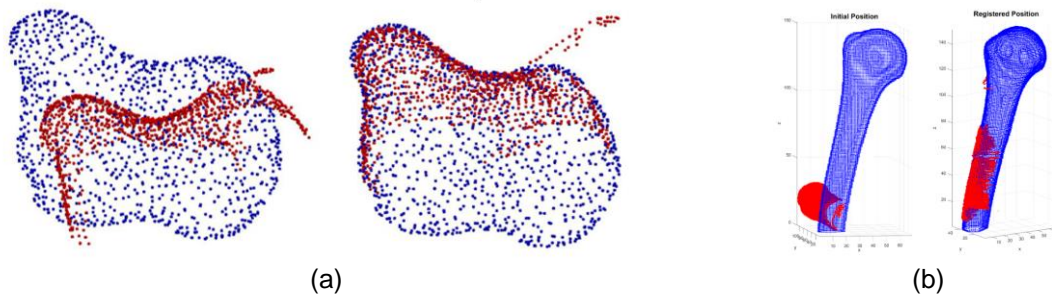
Figure 8: (a) Model-to-model registration that registers the moving model in red to the position of a fixed model in blue that contains the lowest distance between the two surfaces (Adapted from Brößner et al. [49]). (b) An iUS-based femur bone surface registered onto the preoperative derived bone model (Adapted from [50]).

1.2.7 Relevance for Childhood Cancer

Irradical (R1) resection upstages the tumor with an increase of therapeutic load for the patient that should be avoided in all cases. Although the developed extensive 3D preoperative planning workflow ensures efficient surgical planning in the surgical department of The Princess Máxima center, intraoperative guidance is currently not provided [51]. Intraoperative navigation potentially results in the essential correlation between the preoperative planning and intraoperative decision making during complex tumor resections. Therefore, the embedment of this new surgical tool within the surgical department will help the pediatric surgeon with the following improvements:

- Decreasing the risk of irradical resections and consequently decreases the therapeutic load for the patient with improvement of Event Free-and Overall Survival of pediatric patients diagnosed with bone sarcomas.
- Navigating the surgeon to the tumor more efficiently with less tissue damage.
- Decreasing the number of surgical complications such as tumor rupture and blood loss.

Validation of this novel surgical navigation technology in orthopedic oncologic surgery facilitates image-guided tumor resection in other pediatric malignancies such as open abdominal surgery in the surgical treatment of hepatoblastoma, neuroblastoma and nephroblastoma. Image guided surgery may be of an extensive added clinical value in soft tissue tumor resection as tumor visualization and intraoperative feedback of surgical movements in relation to the tumor masses is currently missing. Ultimately, intraoperative navigation during tumor resections in open abdominal surgery will increase the surgeon's dexterity and minimize the risk for irradical resections.

Clinical implementation of this novel intraoperative navigation technique might increase the surgical outcome by lowering the risk of irradical tumor resection. Consequently, this will improve the Event Free- and Overall Survival of pediatric patients diagnosed with bone sarcoma after clinical implementation of this novel intraoperative navigation technique.

2

Research Aim

Within this thesis, the aim is to …

*Improve the **intraoperative translation** of the **preoperative surgical planning** using an **image guided surgical system** together with a **bone-based registration methodology** during **the surgical treatment of pediatric bone tumors with soft tissue components.***

By means of this, the current study will focus on the development and validation of an image guided system that improves the surgeon's spatial awareness during the intraoperative translation of the preoperative surgical planning. The implementation of such surgical tools may address complex tumor localization during the surgical treatment of OS and potentially reduce positive resection margins, minimize unnecessary tissue damage, improve surgical confidence and increase intraoperative decisiveness. Therefore, four critical clinical requirements on the surgical system are considered that must be realized before clinical implementation takes place:

1. Straightforward initial patient registration within 7.5 minutes [52]
2. Registration accuracy <5 mm
3. Accessible re-registration performed in the surgical wound bed
4. Positive evaluation of the ease of use of the surgical system assessed with a self-developed post-procedural questionnaire fulfilled by participated surgeons on a five-points Likert scale

2.1 Research Objectives

Current study will be subdivided into three main objectives with the correlated research question.

Objectives:

1. Develop an algorithm for automatic segmentation of the bone surface on US.
2. Develop an iUS-based navigation system, that complies with the surgical treatment for OS, and evaluate surgical accuracy in a simulation validation study.
3. Validate the developed iUS-based navigation system in a simulated OS surgery using a porcine cadaver and evaluated by end-users.

Research Questions:

1. To what extent is an algorithm capable in accurate automatic bone segmentation on US frames?
   a. What is the coverage percentage?
   b. What is the distance error?
2. What is the target registration error of a self-built iUS-based navigation system?
3. What is the surgical usability and feasibility of the developed navigation system in a simulated OS surgery?
   a. What is the point localization error?
   b. What is the user-experience of the developed iUS-based navigation system in a simulated porcine cadaver study assessed by pediatric surgeons and orthopedists?

2.2 Thesis Outline

The main aim of this thesis is twofold. First, a surgical navigation system must be developed that complies with the clinical workflow for the surgical treatment of OS. During this development phase, the clinical needs must be fulfilled and will be continuously monitored by the involved pediatric oncological surgeons and orthopedists. Second, the developed surgical navigation system will be evaluated by the end-users. This validation will be performed in a porcine cadaver study that simulates the surgical treatment of OS. Consequently, this thesis is subdivided into three parts:

Part I focuses on the development of a deep learning (DL) algorithm for the automatic segmentation of the bone surface on US. During this part, a pre-trained DL network is used for the application of US bone segmentation and trained on image data derived from volunteers. The derived algorithm serves as prerequisite for 3D volume reconstruction of the bone surface required in the next part.

Part II focuses on the development of an iUS-based navigation system, that complies with the surgical treatment for OS, and evaluate surgical accuracy in a simulation validation study. Therefore, the previously derived segmentation algorithm is used together with the surgical navigation setup. Within this setup, an optical tracking system and porcine cadavers are used to compute the target registration error of the developed system. The derived system during the current part is used for the experimental validation study in the next part.

Part III focuses on the validation of the developed iUS-based navigation system in a simulated OS surgery using a porcine cadaver. The derived system has been evaluated by the end-users to gain an 'hands-on' insight in the clinical usability and feasibility of the developed surgical system. The results of the user-experience evaluation are considered as primary objective to assess the applicability of the developed system and to discuss possible implementation in the Princess Máxima Center.

To conclude, the relevance of the derived results within the pediatric oncologic surgery are discussed in chapter 5. This chapter outlines the required improvements that must be done before the system reaches clinical applicability. Moreover, this chapter gives clinical perspectives based on the feasibility of further improvements and potential clinical embedment of current system in the surgical treatment of different pediatric malignancies.
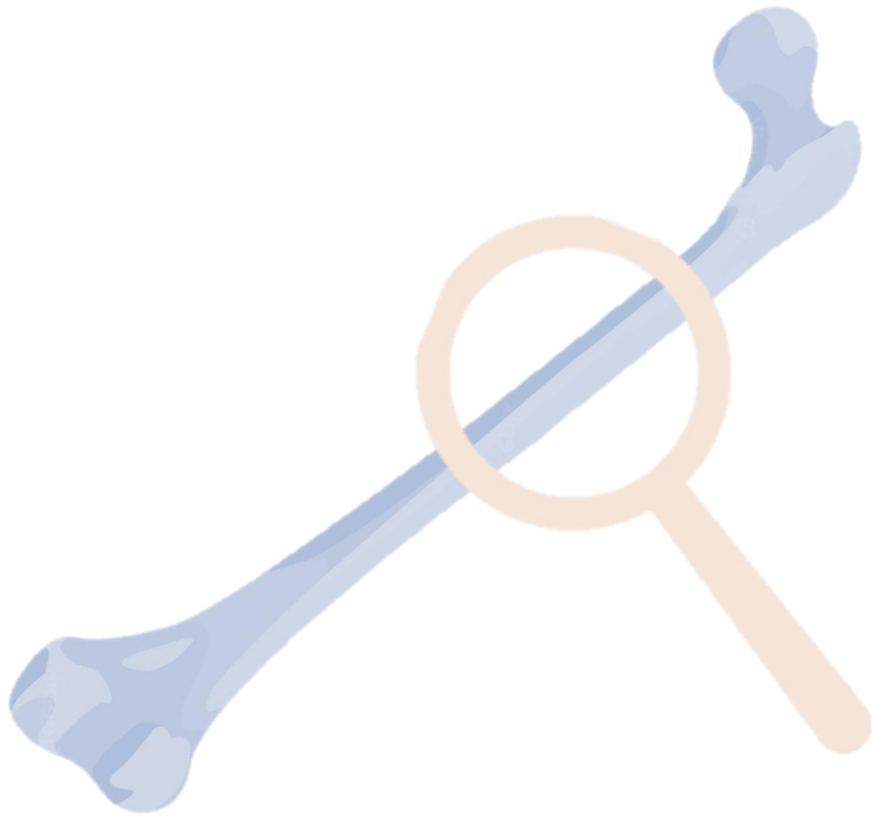
Part 1:

Automatic Segmentation

"The Automatic Detection of the Bone Surface on Ultrasound "

3

Automatic Bone Segmentation

3.1 Introduction

Patient registration in image-guided surgery (IGS) is inevitably related to the correlation of anatomical structures between the digital 3D planning and the physical patient. Localization of superficial anatomical landmarks, such as the nasion for navigation in neurosurgery, are often used in point-based registration strategies. However, in orthopedic oncologic surgery, no superficial bone structures are present during the initialization of the technique that may be suitable for point-based patient registration. Therefore, conventional intraoperative cone beam computed tomography (CBCT) based patient registration is the preferred choice for bone-based patient registration.

Nevertheless, CBCT registration poses limitations such as the availability of an intraoperative CT, radiational harm to the patient and surgical staff, significant interruption of the surgical workflow and re-registration which requires another subsequently significant interruption of the surgical workflow. Although CT is considered as the preferable imaging technique for patient registration, US is widely considered a fast bed-side medical imaging technique highly sensitive to bone structures which may be suitable for patient registration. Therefore, the combination of US together with a tracking system results in intraoperative tracked US (iUS) that might serves as a potential imaging technique to find anatomical structures. The anatomical structures suitable for patient registration found on iUS could either be the bone surface, deep located bone landmarks or vessel bifurcations.

The physics of US is based on the conductance of US beams through tissue and different impedances create a tissue-specific pattern [53]. The bone appearance on US is unique due to a significant impedance difference between the soft tissue and the relatively hard bone surface as shown in Figure 9. Subsequently, a specific acoustic shadow effect occurs behind the bone surface. Recently, the use of this specific bone appearance for automatic segmentation has been developed to classify joint pathologies, hip dysplasia development, fractures, joint kinematics and epidural guidance [54]. Although the applications are numerous, automatic bone segmentation could be challenging due to other hyperechoic structures such as overlying muscles and fascia. These soft tissue layers create similar hyper-intensity pixels that may affect the differentiating between bone and non-bone structures by the network. Subsequently, US is known for a large degree speckle noise that should be incorporated in any image analyzing algorithms. Therefore, algorithms should be robust for these physical limitations of US.
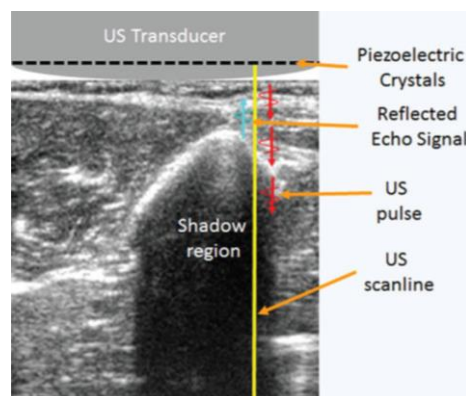
Figure 9: Bone appearance on ultrasound (Retrieved from Hacihaliloglu et al. [55]).

With iUS characteristic bone landmarks of the extremities can now found during the intraoperative preparation phase. These bone landmarks serve as registration features that are comparable to those used with navigation in neurosurgery. Niu et al. used manually assigned bone landmarks located at the femur and tibia with A-mode tracked US to track movement of the femur in relation to the tibia [56]. Although these features could be helpful for patient registration purpose, this introduces observer variability between features found on US compared to CT. Secondly, involving more bone features (e.g., bone surface) results in a point-cloud instead of some bone points alone, increasing the registration accuracy. Therefore, the specific acoustic characteristic of the bone appearance can be used to develop automatic segmentation algorithms with B-mode US. Moreover, automatic delineation derives a 3D point-cloud of the bone surface that potentially serves as registration feature.

Automatic bone segmentation algorithms could either based on deep learning and conventional approaches. Conventional segmentation methods consist of varying approaches such as phase-based, intensity-based, morphological-based, dynamic programming and connected-component analysis. In the pre-phase of this study, a phase-based approach combined with a bone probability map according to approaches found in literature [57–62] and shown in Appendix F. The developed pipeline succeeded for the delineation of bone segments. However, the segmentation was not robust and too sensitive for the soft tissue components, resulting in inaccurate over-segmentation. Moreover, the workflow required a high computational load, resulting in long segmentation times. Therefore, the potential for alternative approaches was required.

Deep learning (DL) is becoming more prominent in real-time interpreting US imaging [63]. Also, for the automatic delineation of the bone surface, DL is promising with the U-Net architecture as the most prevalent used architecture [50,64–69]. The U-Net architecture is a fully convolutional architecture designed explicitly for biomedical image segmentation by Ronneberger et al. [70]. In this study, an automatic segmentation pipeline will be developed that may be used in subsequent fast 3D volume reconstruction of the bone surface found on US. The main aim of this part is to evaluate the capability of DL for automatic bone segmentation in terms predicted bone surface and the distance error.

3.2 Method
This section describes the development steps required for the automatic bone segmentation algorithm.

3.2.1 Network
The network architecture used in this study was based on a pre-trained 3D U-net DL network developed by M.A.D. Buser from our research department. This DL architecture was primarily developed for the automatic segmentation of nephroblastoma (i.e., Wilms tumors) on MRI scans. To adapt the architecture for current application, a transition from 3D to 2D was provided. Training and validation were performed on a NVIDEA T1000 graphical card and Python (version 3.9) with the open-source Spyder interactor.

3.2.2 Data Acquisition
Data acquisition was derived using the Hitachi Aloka with the linear L441 probe (Hitachi Medical, Tokyo, Japan) and US parameters as shown in Table 5. Image data acquired by the Hitachi Aloka was streamed to a computer workstation with a frame grabber (Epiphan System Inc, Ottowa, Canada) and saved as .png files. The number of images (n = 1084), anatomical region and image dimensions are listed in Table 4. The effect of different US parameters on the appearance of the bone surface on US is shown in Appendix E. The Institutional Ethics Review Board waived the necessity for additional informed consent for the patient data since the treatment was not influenced. Additionally, informed consent was obtained of the two adult volunteers.

Table 4: Dataset information.

Subject:	US Machine:	Anatomical Region:	Number of acquired US frames
Resected proximal tibia	Hitachi Aloka	Proximal Tibia	319
Volunteer #1	Hitachi Aloka	Tibia and fibula	238
Volunteer #2	Hitachi Aloka	Radialis and Humerus	527

Table 5: Ultrasound parameters with the L441 Linear probe of the Hitachi Aloka

Parameter:	Value:
Frequency	9 MHz
Depth	6 cm
Dynamic Range	90 dB

3.2.3 Image Pre-Processing

The image dimensions of every frame in the data set must be equal to obtain a homogeneous dataset that is compatible with the kernels used in the U-Net network. Altering the input dimensions can be achieved by inter- or extrapolation operations that changes pixel values to obtain a decreased or increased dimension, respectively. In this study, a segmentation algorithm was built that might be used for an IGS-application. Therefore, the desired output dimension together with the pixel locations should be equal to the input and thus inter- or extrapolation was discarded. An alternative manner for image pre-processing is zero-padding. This operation increases the image dimension by adding layers of zero valued pixels at the outer regions of the input image. This pre-processing step can be inverted after prediction, remaining an output equal to the input. For this reason, zero padding was used on the whole data set to obtain image dimensions equal to 384X384 pixels. To decrease the computational task load during training, the image was downscaled by a factor of two, to obtain an image dimension of 192X192 pixels. The complete workflow for the pre-processing steps is shown in Figure 10. For application in a surgical navigation system, the derived network should be applicable for input data that has not been downscaled. Moreover, to fit an input that is compatible to the kernel, zero padding is used to obtain an input equal to 304X304 pixels.

Figure 10: Image pre-processing

3.2.4 Data Labelling

Dataset labelling was performed by a Technical Physician, master student, who was trained in recognizing the bone surface on US images, as shown in Figure 12a-b. Delineation of the bone surface was performed after adjustments were performed on the input data to create a homogeneous dataset, as described in the previous section. The Image Labeler tool provided by the Computer Vision Toolbox in MATLAB (R2022b) was used for data labelling. Within this tool, the user can manually select several points on the bone surface and create a smooth line.

3.2.5 Data Augmentation

Data augmentation can be applied to improve the heterogeneity (i.e., diversity) of training's data and potentially increase the performance of the network. Resultingly, data augmentation could lead to less overfitting due to an increased fraction of image variability of the trainings data. The manner of augmentation depends on the dataset and can be applied in two approaches. First, the amount of

training data will be extended with the addition of augmented frames. Second, augmentation will be applied to a fraction of the whole training data without the addition of frames. In this study, large homogeneity was found between consecutive image frames within US sweeps, regardless to the fundamental noise of US. Augmentation of a fraction could correct for this large fraction of homogeneity and was therefore applied for this latter.

Different augmentation methods were applied to the training set to evaluate the effect on the network's performance. Data augmentation for this purpose should be limited to the physical behavior of the interaction of US and bone surface reflections [71]. Zaman et al. observed network improvement after applying a Gaussian blur filter (sigma = 1.1) and a vertical, left-right, flip or combined as shown in Figure 11. Both rotational and horizontal, up-down, flip operations were considered impractical as the unique bone feature will be decreased [71]. Therefore, a Gaussian blur, vertical flip and a combination was applied to a quarter of the trainings set per operation.

Figure 11: Data augmentation methods: (a) original ultrasound frame, (b) applying a Gaussian blur filter and (c) a vertical flipping operation.

3.2.6 Hyper-Parameter Optimization

Hyper-parameter optimization was performed concluding a batch size of 4, an Adam optimizer with a learning rate of 1e-04 were found to be optimal and chosen for this application. This network was trained and tested with B-mode US images with an 80:20 train:test split, respectively.

3.2.7 Evaluation Metrics

The main aim of the development for current application is the detection of bone surface. In other words, if the bone is detected by the network correctly, the overall performance should not be punished by potentially over segmentation. In DL evaluation metrics, the Hausdorff distance and the Sørensen–Dice Score are conventionally used to evaluate the network's performance [72]. However, in current practice, this may be impractical as these metrics use the comparison between areas of the predicted and labelled skeletonized segmentations in the whole frame, as shown in Figure 12c. Current network compares two lines representing two bone surfaces in the periphery of the label. Therefore, the Hausdorff distance inevitably will result in a measurement between the end and starting points of the two lines or with a noise component. Moreover, the Dice score could be coarse, although the local segmentation may be acceptable. Therefore, other evaluation metrics had to be defined to evaluate the correspondence between these two lines while discarding potential over segmentation. Guo et al. suggest several evaluation metrics for comparison of automatic centerline detection of arteries found on CT [73]. In this study, two metrics were considered helpful for the evaluation of the network's performance:

- Coverage percentage. The percentage of detected pixels covered by the label within an acceptance interval of 1.46 mm around the label (2 pixels).
- Bone surface distance. The median absolute distance between the label and the closest detected pixel.
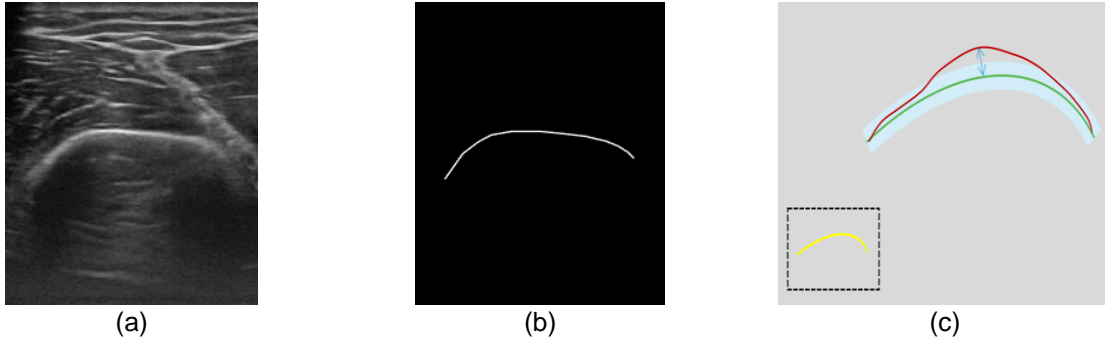
Figure 12: (a) The initial US image of the proximal humerus of a volunteer. (b) The mask with the labelled bone surface. (c) Evaluation metrics with the label in green, the area of acceptance in blue, the predicted in red and the over-segmentation in yellow.

Statistics

The derived data was tested for normality using a Saphiro-Wilk test in SPSS Statistics version 28 (IBM SPSS Statistics, New York, United States of America) [74]. The null hypothesis for normal distribution gets rejected if the p-value<0.05 and the median values were computed.

3.2.8 Independent Test Set

In addition to test set, the network was tested on an independent dataset also. This dataset included 920 US images acquired from the distal tibia, proximal and distal femur, ribs, sternum and distal humerus of two adult volunteers. These structures were in accordance with possible iUS-based navigation techniques during for the surgical management of OS. The number of acquired US frames per bone structure and per volunteer is listed in Table 6. Informed consent was obtained of these two volunteers and image acquisition was performed with the Hitachi Aloka and the L441 linear probe.

Table 6: Independent data set.

Anatomical Structure	Volunteer #1	Volunteer #2	Total Images
Distal femur	91	88	179
Proximal femur	73	52	126
Distal humerus	84	57	141
Sternum	66	57	123
Rib	108	111	219
Distal Tibia	59	72	132

3.3 Results

The results for an optimal and sub-optimal performance are shown in Figure 13a-b. Although the sub-optimal performance shows locally optimal detection of the bone surface, major over segmentation components were present. The evaluation metrics regarding the detected bone surface is shown in Figure 13c.

The network was primarily tested with the stated hyper-parameters and without data augmentation applied. This resulted in potential optimal performances for the internal test set already, as shown in Figure 14a. Three data augmentation operations were applied and the results for the median coverage percentages are shown in Figure 14b-d. The performance of the network for the distal femur was observed to be relatively poor in all situations. The effect of data augmentation on the performance resulted in an improvement of the performance for the independent test set, especially. Therefore, the performance of the network on the independent test set was leading, defining the final network.

(a)   (b)   (c)
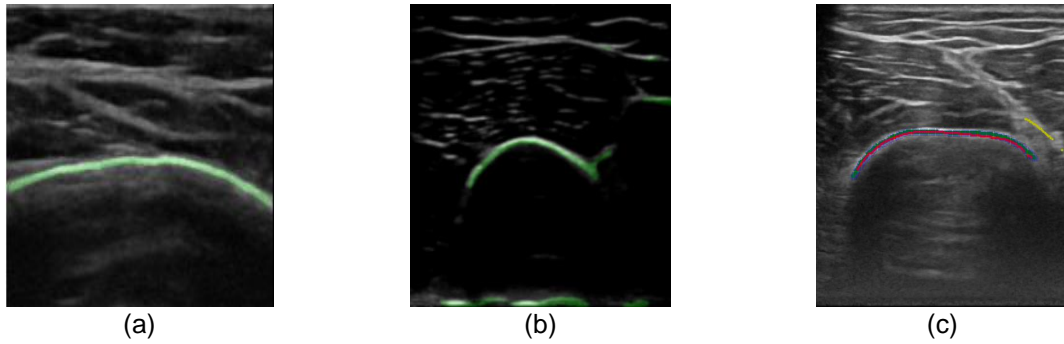
Figure 13: (a) Optimal detected bone surface. (b) Sub-optimal detect bone surface. Local proper detection, with some over segmentation components (c) The predicted bone surface (in red) after automatic segmentation by the network. The annotation is shown in green with the range of acceptance in blue. Over segmentation occurred for this specific case and this is shown in yellow as part of the fascia was considered as bone.

The best overall performing network was obtained with an epoch size 20, application of both Gaussian blur ($\Omega = 1.1$) and a vertical flip as shown in Figure 14d. The null hypothesis was rejected in a fraction of the results, and therefore it was assumed that the data was not normally distributed. This network resulted in a median coverage percentage of 100% (100% - 100%) coverage percentage and a median distance of 1.18 mm (0.98 – 1.23 mm) for the internal test set. The results for the independent dataset, specified per bone structure, can be found in Table 7. The results for these bone structures reported a cumulative median coverage percentage of 96% (92% - 98%) and a median distance error of 1.57 mm (1.38 – 1.83 mm). The effect of different hyperparameters on the network performance can be found in Appendix H.

(a)   (b)

(c)   (d)
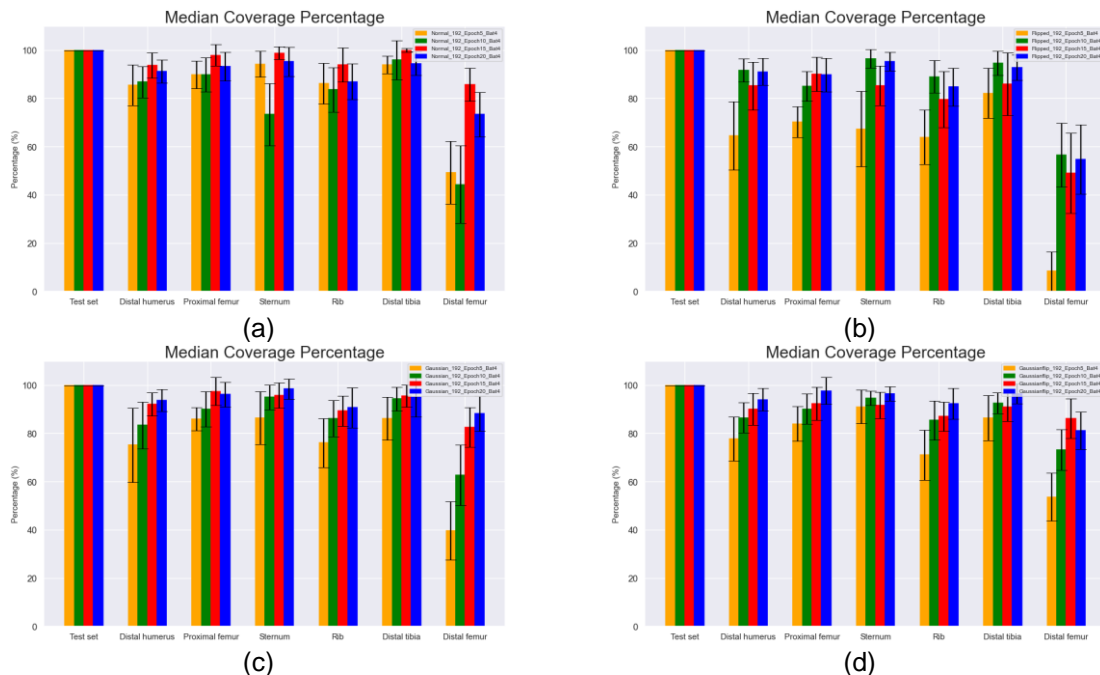
Figure 14: The results of network prediction on the median coverage percentage applying different data augmentation operations and epochs for the different test sets. (a) No augmentation applied, (b) vertical flip operation, (c) Gaussian blur operation and (d) both a vertical flip and Gaussian blur.

Table 7: Validation results for the test and the independent dataset. The evaluation metrics are the coverage percentage of the predicted bone surface and the distance between the predicted and labelled surfaces.

Data set	Coverage Percentage (%)			Distance (mm)		
	Median	25th percentile	75th percentile	Median	25th percentile	75th percentile
Test set	100.00	100.00	100.00	1.18	0.98	1.23
Sternum	97.82	95.01	100.00	1.44	1.07	1.73
Rib	92.62	96.07	97.62	1.45	1.15	1.84
Distal humerus	97.65	90.24	100.00	1.69	1.32	1.97
Distal femur	90.96	83.59	97.52	2.26	1.82	2.69
Proximal femur	95.00	87.50	100.00	1.68	1.40	1.95
Distal tibia	96.55	93.31	100.00	1.21	1.00	1.43

3.4 Discussion

The potential of automatic segmentation of the bone surface on US frames was evaluated with a pretrained 3D U-net network specialized for automatic segmentation of nephroblastoma on MRI scans. The developed network reached potentially optimal performance for 3D volume reconstruction for patient registration applications within a median distance error of 1.57 mm. Training was performed with a relatively small training set with a high risk for similarity that could have affect the performance on non-trained data.

The training set consisted of US sweeps with a significantly large degree of similarity within the consecutive sweeps caused by the acquisition speed of approximately 1cm/sec. Therefore, data augmentation was used to increase the variability of the training set to correct for this similarity within the sweeps. In this study, data augmentation was evaluated by mirroring the image, applying a Gaussian blur filter and/or a combination of both operations to a quarter of the training set per operation. Although the used data augmentation approaches in this study, more data augmentation methods were suggested in literature. Importantly, the typical physical appearance should be maintained and therefore all rotational operations were discarded [71]. The effect of rotation and vertical flipping was evaluated and the observation in literature was proven as shown in Appendix G. Rotation and vertical flipping showed a decrease of correct predicted bone surface while increasing the rotational angle. The maximum rotational angle of 180 degrees rotation, a vertical flip, showed the poorest performance.

Tirindelli et al. have proven the use of data augmentation and suggested deformation, simulating reverberation artifacts and adjusting the Signal-to-Noise Ratio as novel augmentation operations [71]. However, after the addition of one or all three suggested operations, the improved performance did not outperform the operations similar to those used in this study. Moreover, increasing the training set's variability could have been done using a generative adversarial network (GAN) for data augmentation [75]. Subsequently, Zaman et al. evaluated the application of GAN for bone segmentation based on US frames [50]. The authors observed an increased heterogeneity of anatomical features such as altering the pixel intensity of the muscles alone instead of adjusting all pixel intensities. Although this increase of heterogeneity could not be obtained by standard data augmentation, GAN augmentation did not outweigh the increased performance with standard data augmentation. Nevertheless, the authors observed a slightly better performance with the addition of GAN in combination with standard augmentation. Nevertheless, the use of GAN could be beneficial, the development of such networks requires a large training set. Therefore, the use of a bone segmentation specific GAN is limited and currently no accessible pre-trained GAN was available in literature to the author's knowledge.

The influences of the probe orientation on bone appearance have been noticed during US acquisition. The brightness of the bone surface changed by altering the angle of the probe in relation to the bone surface changes. This was resulted as the specific echogenicity character of bone will be reduced if the imaged bone surface is not perpendicular to the probe. Consequently, US beams travel in a non-perpendicular way to the bone surface and the acoustic energy is transmitted more effectively through the bone surface, resulting in less reflection [69]. Therefore, the transducer should always be orientated perpendicularly to the bone surface, providing a significant bone contrast on US frames. Nevertheless, involving more US frames derived in a non-perpendicular orientation in the training set could have

resulted in a less sensitive network for those probe orientations. Current trainings data included US frames acquired in a perpendicular manner mostly. Therefore, the derived network may underperform in case of an oblique probe-to-bone orientation and the overall performance might be user-dependent. In practice, including more orientations will lead to a more robust network regardless of the operator.

According to a scoping review of Pandey et al., evaluation metrics for the validation of automatic bone segmentation were abundant [29]. The authors concluded that the Dice-score and the mean distance error were the most frequently used metrics for pixel classification and distance calculation, respectively. In this study, the coverage percentage and median distance were defined as primary metrics comparable to Pandey et al.'s observation [69]. First, although the Dice-score and coverage percentage are not precisely the same, they both provide information about the segmentation performance. The coverage percentage is not sensitive for false positives such as over-segmentation in non-bone areas. Moreover, it was stated that the Dice-score was too sensitive for minor mistakes by the network that would not affect the performance for the specific application described in Chapter 4. The application requires optimal performance for the detection of bone surface without over segmentation linked to the bone surface (i.e., leaking). Second, the median distance error used in this study gives information about the distance error of the predicted with respected to the labeled surface. This metric is comparable to the metrics found in literature [69]. Unfortunately, the used evaluation metrices lacks for the quantification of potential leaking of the network. Nevertheless, neglectable leaking was observed after visual inspection of the results. Further research should implement an evaluation metric to quantify potential leaking components.

The bone structures in the independent test set were chosen based on potential embedment of this segmentation algorithm in an iUS-based surgical navigation system during the surgical management of OS as described in Chapters 4 and 5. For this clinical application, an iUS-based surgical navigation system should be registered at the healthy part of a bone structure affected by bone sarcoma. For instance, in case a tumor is located in the distal femur, the iUS sweep is performed at the proximal femur requiring accurate bone segmentation in this specific bone segment. Although, comparable results were found for different bone structures, remarkable poorer performance was reported for the distal femur. After visual inspection of the results acquired for the distal femur, the network had difficulties to accurately predict the start and end points. This could be caused by either under segmentation during the manual segmentation or over segmentation by the network. The appearance of the distal femur on US showed relatively large, curved components suppressing the characteristic bone appearance at these challenging distal parts. Therefore, both under segmentation during manual segmentation and correct prediction by the network was observed and concluded by the operator. The influence of these curved components on the performance should be further evaluated in future work.

This study has some limitations that need to be acknowledged. First, the used dataset consisted of iUS sweeps derived from three objectives, resulted in a dataset sensitive for similarity between consecutive frames with an iUS sweep. Therefore, further research should include more iUS sweeps of more objectives. Nevertheless, the performance of the network was already useful with this relatively small, around 1000 US frames, data set and the importance for increasing the amount of image frames was not proven in this study. Second, the adult volunteers involved in this study would not represent pediatric patients. Therefore, further improvement should be limited to pediatric patients or volunteers as the amount of fat and muscles potentially effecting the network is different between adults and children. Third, the additional value of pre-processing of the input data was not evaluated. Further research should improve the addressed technical shortcomings to improve the derived bone segmentation.

3.5 Conclusion

The initial network was retrained and validated using a dataset consisting of US frames of the tibia, femur and humerus, resulting in a median coverage percentage of 100% (100% - 100%) and a median distance error of 1.18 mm (0.98 – 1.23 mm). Subsequently, an independent dataset including the tibia, femur, ribs and humerus, was used for further validation and resulted in a cumulative median coverage percentage of 96% (92% - 98%) and a median distance error of 1.57 mm (1.38 – 1.83 mm). The current network should be improved by increasing the data set resulting in better performance and less over-segmentation in some frames. Nevertheless, the sequential computation of 2D bone segmentations may be used for accurate 3D reconstructions of the bone surface.
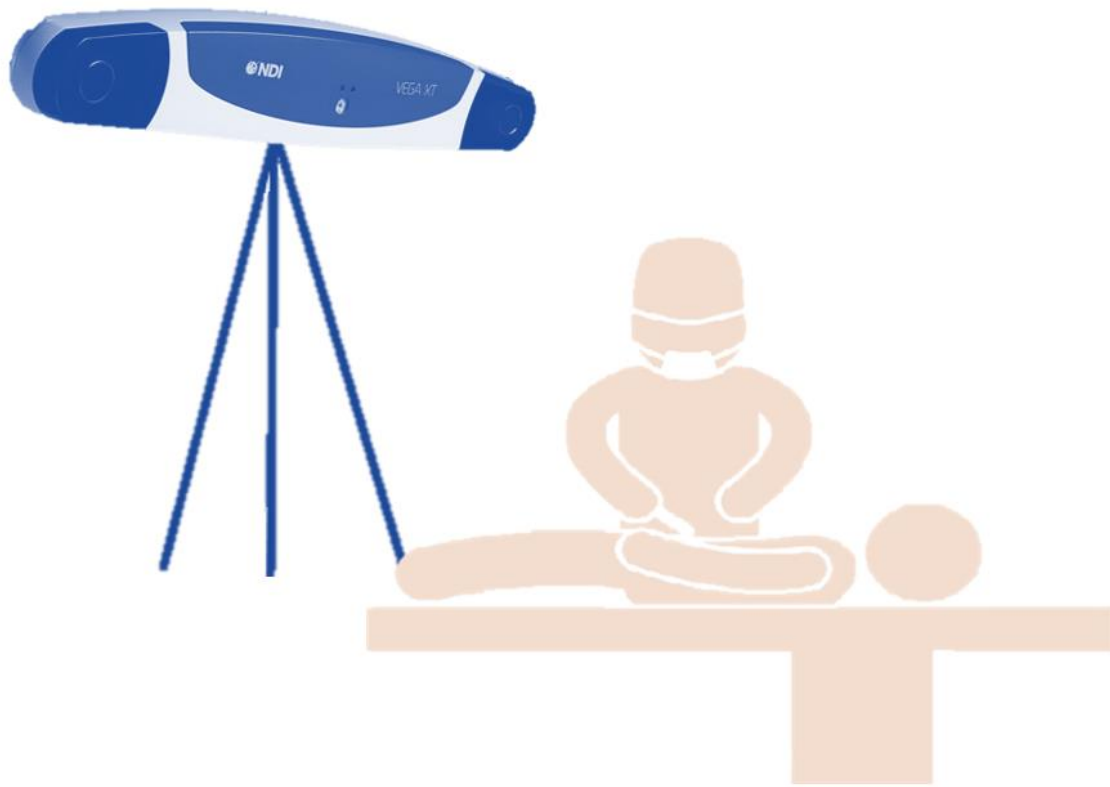
Part II:

Image Guided Surgery System

"The Development of a Tracked Ultrasound based Surgical Navigation System"

4

Ultrasound Navigated Surgery

4.1 Introduction

Radical resection remains the cornerstone in pediatric oncological surgery. In recent years oncological surgeons benefit from the advantages of image-guided surgery (IGS) as a surgical tool, proven in both orthopedic and neurosurgery [4]. Using IGS in oncological applications may improves surgical and oncological outcomes and reduces surgery time. Importantly, it may aid in safer oncological margins while maintaining as much healthy tissue as possible, minimizing morbidity [5]. Commercialized IGS systems for orthopedic surgery, often includes patient registration during the intraoperative preparation phase, to match the virtual planned 3D model with the physical patient. This registration methodology requires the invasively fixation of Kirschner wires into the bone, followed by an additional three-dimensional (3D) CBCT scan. Within this patient registration, the surgical workflow is interrupted significantly, and the patient is exposed to additional radiation [31]. This scan requires a free path during the rotation and adequate positioning of the device is required. Moreover, both the patient and the surgical staff will be exposed to harmful radiation exposure. Altogether, image acquisition of the CBCT-based patient registration requires approximately 15 minutes [25]. Eventually, this extensive image acquisition procedure results in an inaccessible re-registration in case the registration got lost during surgery. Resultingly, the surgeon must balance between ongoing surgery without navigation or interrupting procedure to regain accurate navigation. The involved orthopedists reported this inaccessible re-registration as major limitation during current practice and most often continue without re-registration.

Alternative registration methods might result in faster registration, less interruption of the surgical workflow, and decreased radiation exposure for the patient. Also, if registration becomes inaccurate during surgery, which is a frequent problem during surgical navigation, quick and fast re-registration should be easily accessible to maintain the availability of an accurate navigational tool throughout the procedure.

Intraoperative tracked ultrasound (iUS) combines image acquisition with real-time positional information. This can be used to find rigid physical anatomical features on iUS that can be used during patient registration. The bone surface on US has an unique appearance due to a large impedance difference between soft tissue and the hard bone surface [67]. Therefore, automatic segmentation of the bone surface on iUS and 3D volume reconstruction may serve as a novel registration feature. The technical feasibility of this iUS-based registration methodology, using the bone surface as registration feature, was proven in previous studies [49,76–78]. Ciganovic et al. developed a registration workflow that manually extracts the bone surface on freehand US frames to obtain a 3D bone model that was used for patient registration [78]. In volunteers, the authors observed a highly accurate point-to-point distance error of 0.57 (± 0.08) mm.

During iUS-based registration, the time for image acquisition is potentially quicker compared to the CBCT-based registration. The workflow for either CBCT-based and iUS-based registration is listed in Table 8. Especially, the time of workflow interruption might be neglectable as US acquisitions are common during surgery and mostly completed within a few minutes. Moreover, as the iUS sweep must be performed on the healthy section of the bone, the surgeon may be able to continue while an assistant performs the relatively short iUS sweep. This manner of image acquisition may result in an acquisition time of <7.5 minutes, allowing for potential fast re-registrations in case of inaccuracies occurs during

the procedure. Therefore, replacing the CBCT with iUS may potentially results in a more robust and more straightforward surgical navigation system. Therefore the calibration of the US probe is required.

Table 8: Surgical phases required for either CBCT- and iUS-based navigation.

Surgical Phase:	With CBCT-Based navigation:	With iUS-Based navigation:
Preoperative Planning	Preoperative CT or MRI	Preoperative CT or MRI
	Surgical Planning	Surgical Planning
	Defining site of incision	Defining site of incision
Intraoperative Preparation	Sterile draping	Sterile draping
	Fixation Kirschner wires	Fixation Kirschner wires
	CBCT patient registration	iUS patient registration
Intraoperative Guidance	Primary incision	Primary incision
	Actual surgery	Actual surgery
	CBCT re-registration	iUS re-registration

Tracked Ultrasound Calibration

Accurate calibration of the iUS is inevitable related to the accuracy of an iUS-based surgical system [79]. Probe calibration defines the static relation between the real-time image acquisition and the position and orientation of the US probe, consisting of a temporal and a spatial calibration procedure. The used registration method is a non-rigid transformation including translation, rotation, and scaling. Temporal calibration corrects for the time offset between image and tracking acquisitions to derive an accurately synchronized data stream. Spatial calibration is considered as the main cause of inaccuracies [79] and this calibration defines the match between the image pixel coordinates with the optical reference body attached to the US probe.

Temporal calibration corrects for the potential time lag between imaging and tracking data, fundamental for iUS-based procedures. Therefore, the iUS probe is moved up and down in a tank filled with water, while imaging the bottom of the tank. Resultingly, two sines-shaped curves defining the bottom of the tank and the vertically tracking information. Calibration defines the match of these two shapes, computing the time lag correction to obtain an accurate match [79].

Although different spatial calibration approaches has been reported in literature, an optimal standardized method has currently not been provided [42]. These approaches are performed by either matching detected features on US of a tracked phantom or localize the tip of a tracked pointer on US. The match between localized features on imaging and tracking, relates the desired static calibration. However, accurate localization of the target point on imaging (e.g., tool tip) may be potential for misinterpretation and thus error. Therefore, automatic segmentation algorithms in N-wire phantom calibration procedures could be more accurate. Although, this potential advantage, the calibration of these N-wire phantoms are highly related to the accuracy of the phantom itself (e.g., 3D printing accuracy) [42,80].

Tracked phantom based spatial calibration requires an accurately developed phantom. Moreover, the N-wire phantom is the most used open-source calibration phantom and shown in Figure 15a [42]. Within this phantom, several N-shaped wires can be spanned following fixed configuration resulting in a specifically US pattern as shown in Figure 15b. Automatic segmentation of the cross-section of these wires improves the spatial calibration. [42,81].

(a)	(b)
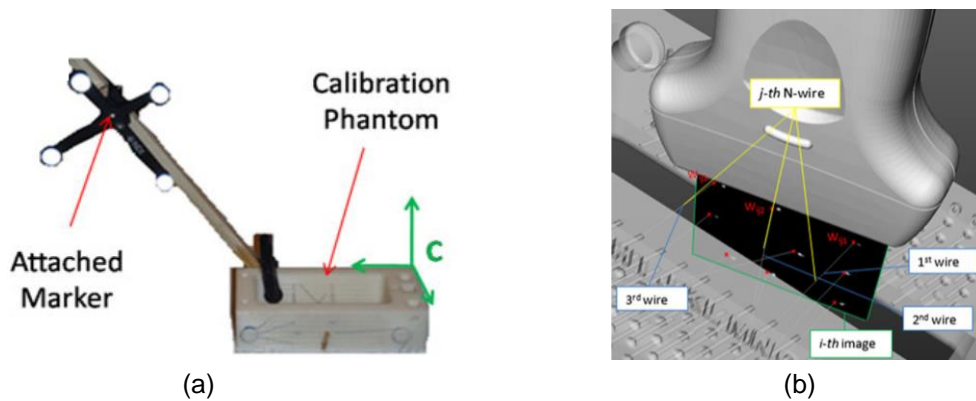
Figure 15: (a) Tracked N-wire phantom. (b) Image acquisition of the N-wire phantom, resulting in a specific US pattern of the spanned N-wires. (Retrieved from Carbajal et al. [82])

Tracked pointer based spatial calibrations are considered as the most straightforward iUS calibration method and requires the tracked tool calibration as prerequisite. During the procedure, the iUS is placed in a tank filled with water, imaging the tracked tooltip. The position of the tracked tooltip is saved and correlated to the manually located tip on US imaging. The spatial transformation is computed by applying an ICP registration, linking at least three points together. The causalities for errors are the tracked tool calibration and precise localization of the tool tip in the US plane [80,83]. The tracked tool calibration was reported to have similar accuracies compared to the N-wire phantom calibration [84].

iUS-Based Patient Registration

Patient registration is performed by matching the digital model to accessible anatomical features present in the physical world. Before this fundamental step can be performed, several steps are required to derive a 3D bone model linked to the physical location of the patient, as shown in Figure 16.

During the intraoperative preparation phase, the physical location of the patient is being tracked. Second, an iUS sweep is performed either over the skin of the patient or in the surgical wound bed. This iUS acquisition results into 2D US frames that are coupled to the physical location. Third, anatomical landmarks (e.g., the bone surface) are automatically segmented on this iUS acquisition. Fourth, these segmented 2D frames are reconstructed to a 3D volume. Finally, this 3D volume (i.e., point-cloud) is available for ultimate registration. Therefore, the preoperative patient-specific 3D model of the landmarks is matched with the iUS derived point-cloud. Patient registration is completed, and the navigated surgery system is now available upon the indication of the surgeon.
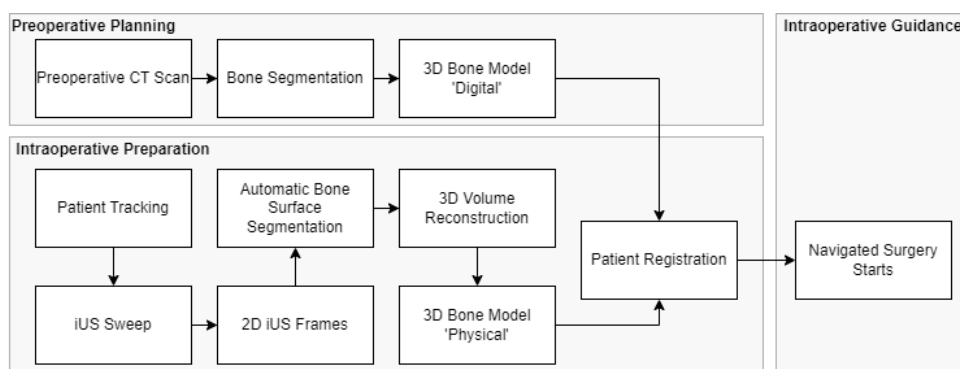
Figure 16: Schematic diagram of an iUS-based surgical navigation workflow.

In this study, an iUS-based navigated surgery system will be developed using the previously developed automatic US-based segmentation workflow (Part 1). The main aim of this part is to determine the surgical accuracy of the developed system. The developed system requires an accuracy better than 5 mm for clinical applications.

4.2 Method

This section describes the development steps required for the iUS-based surgical system. This system involves the derived segmentation algorithm of Part I as prerequisite. Moreover, surgical accuracy of the derived system is computed with a gold standard registration. Therefore, two registrations were required for the evaluation of the surgical accuracy with porcine cadavers.

4.2.1 Hardware

The surgical navigation system consists of several hardware components. Firstly, a Philips CX50 US (Philips, Best, The Netherlands) machine together with a linear probe (Philips L12-3) was used for US acquisition. Streaming of these US images (100 fps) to a computer workstation (NVIDEA T600 4GB graphical card, 32GB Ram) was performed with a frame grabber (Epiphan System Inc, Ottowa, Canada). Secondly, positional data of the US probe, surgical instruments and cadaver were captured by an optical tracking system (Northern Digital Inc., Polaris Vega ST, Waterloo, Ontario, Canada).

The trackable objects required an attachable optical reference body (ORB) to capture the position and pose of these objects by the optical tracking system. Therefore, the ORBs provided by the commercial NDI system were used. However, one ORB was missing for cadaver tracking in the setup and therefore an ORB designed by Brown et al. adjusted and 3D printed [85]. The authors designed several printable ORBs that were compatible with the NDI tracking system with comparable accuracies. During this experiment, three pivot points were placed onto this ORB, used for gold standard point registration. Tracking occurred by the optical tracking system and four rigidly attached passive reflective markers on each ORB. An overview of the whole setup is shown in Figure 17.

Figure 17: Schematic overview of the experimental setup.

Within the PLUS Open-Source Toolkit for Ultrasound-Guided Intervention Systems several 3D models were provided that were made for specific transducers [86]. This library consisted of a clip specifically made for a linear transducer compatible with a Telemed Ultrasound system, The clip was then adjusted according to the Philips L12-3 probe by increasing the height, width, and length with a factor 1.13, 1.27 and 1.10, respectively. Secondly, the attachment frame for the ORB was tilted with 15 degrees to obtain a better line-of-sight between the probe and the optical tracker for different US scanning procedures. Consequently, the derived 3D model was printed using an Ultimaker S5 and a PLA filament as shown in Figure 18-a. The probe together with the 3D printed clip and the ORB is shown in Figure 18-b.

<div style="text-align:center">(a)   (b)</div>
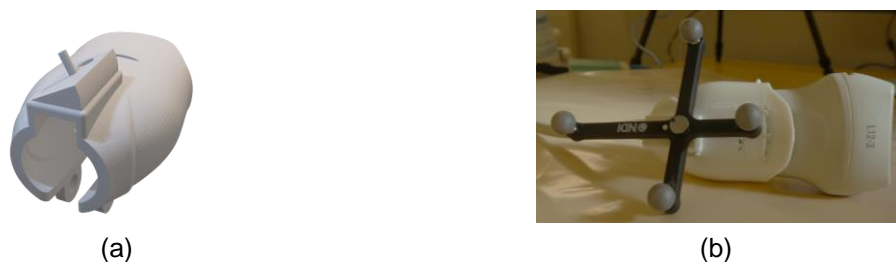
Figure 18: (a) The 3D-model of clip for the US probe. (b) The Philips L12-3 iUS-probe with the attached 3D-printed clip and the optical reference.

4.2.2 Software

The software packages used for the surgical navigation setup can be subdivided for different components. Tracking occurred using the NDI software, derived from the manufactory. Imaging data was acquired and streamed via the Epiphan software. Altogether, the tracking and imaging data acquired were streamed to a computer workstation trough a TCP/IP and USB 3.0 connection respectively. Within the workstation, a configuration file (shown in Appendix C) that was derived and adjusted from the Plus Server that was made available by the open-source PLUS Toolkit [86]. This configuration file combines the input tracking and imaging data to a server that can be read out by the SlicerIGT extension toolkit. The open-source computer vision software 3D Slicer was used to obtain the 3D models and to perform the actual surgical navigation procedure. Within the 3D Slicer software, the SlicerIGT extension was used to obtain the tracking and image data acquired by the Plus Server. Automatic bone segmentation occurred in Spyder (Anaconda 3, Python 3.9). The complete workflow for the data streaming is shown in Figure 19.
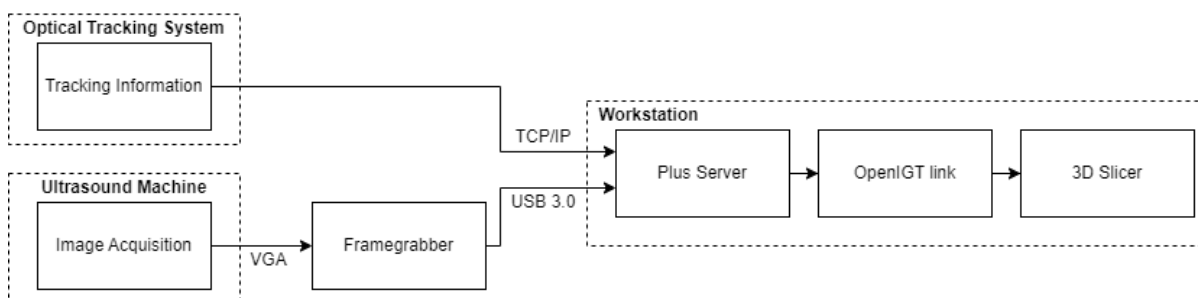
Figure 19: Data streaming workflow

4.2.3 Porcine Cadavers

The registration accuracy was validated using eight lower legs, both left and right, derived from porcine cadavers obtained via a local butcher. For conservation, all cadavers were stored in the fridge and defrosted one day before the experiment. Before the cadavers were scanned, an ORB was placed in the distal tibia and two Kirschner wires were placed in the proximal tibia. The ORB in the distal tibia was fixated with two, conventional (∅=6mm), screws together with a 3D printed clamp and served as ORB for the gold standard. Fixation of the ORB and the 3D printed clamp occurred with a 3D printed bolt and nut to avoid metal artefacts. Finally, the, frozen, cadavers were CT scanned (Siemens Somatom Spiral CT scanner, Erlangen, Germany) with the used scan parameters for a single cadaver shown in Table 9, representative for all cadavers. Metal artefacts were minimized using the in-built Iterative Metal Artifact Reduction (IMAR) option. Consent was obtained from the Head Technician Diagnostic Imaging of the Faculty for Veterinary Medicine (University of Utrecht, the Netherlands) to conduct image acquisitions and experiments in their institute.

(a)   (b)
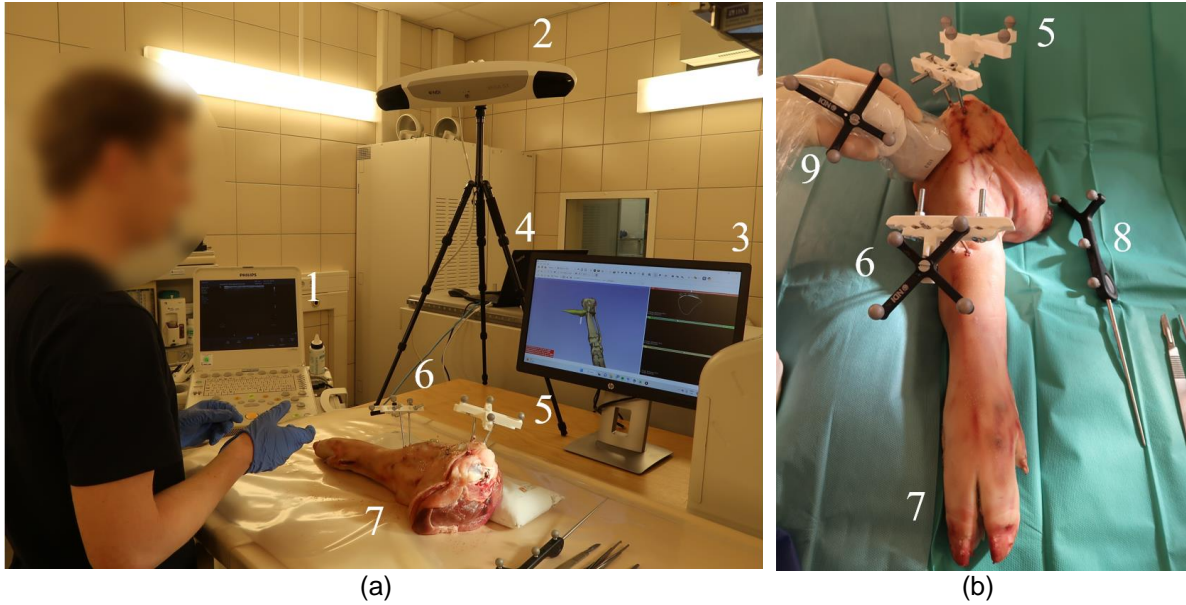
Figure 20: (A) The experimental setup and the (B) intraoperative situation. (1) Ultrasound machine and frame-grabber, (2) optical tracker, (3) 2D interactive screen, (4) computer workstation, (5) ground truth optical reference body, (6) cadaver optical reference body, (7) lower leg of a porcine cadaver, (8) tracked surgical pointer and (9) tracked ultrasound probe.

Table 9: Scan parameters for cadaver 8.

Parameter	Value
Tube voltage (kV)	140
Beam collimation (mm)	32 * 0.60
Detector rows	32
Voxel spacing (mm)	0.46 *0.46*1
Type scan	Spiral
Rotational time (sec)	0.5
Tube current – time product (mAs)	82 - 160
Tube current (mA)	51-102

Segmentation

The scan was exported and imported to the workstation as DICOM files. With these DICOM files, segmentation was performed in 3D Slicer to derive the cadaver specific 3D model using the 'Segment Editor'. In this editor, a 'Grow-From-Seeds procedure was performed in 3D Slicer. Areas in the bone and background, were manually labelled and used as input for the segmentation procedure. Although the IMAR option reduced metal artifacts, special care for segmentation was required near the metal components. Segmentation of the bone resulted in a 3D model of all bones below the knee joint. Finally, ten artificial surgical targets were placed on the bone surface for the evaluation of the surgical accuracy as shown in Figure 32. The followed protocol is shown in Appendix D.

4.2.4 Calibration of Surgical Tools
Stylus Calibration

A rigid static transformation between the tooltip and ORB of the surgical pointer is required. Therefore, a pivot calibration method was performed as provided by the 3D Slicer Software. During this procedure, the tooltip of the surgical pointer was positioned on a rigid point and a circular motion around this point was performed as shown in Figure 21. Consequently, the 3D Slicer software calculates the static transformation ($^{Stylus}T_{StylusTip}$) matrix to express the tooltip coordinates in the ORB frame of the surgical pointer.

(a)   (b)
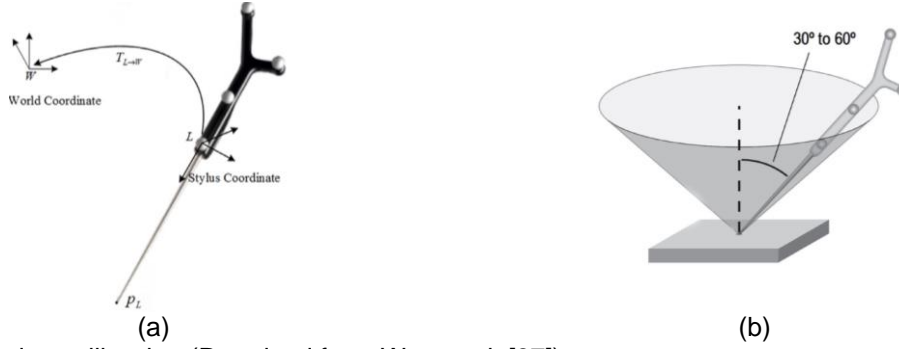
Figure 21: Stylus calibration (Retreived from Wen et al. [87])

Calibration of Tracked Ultrasound

The calibration transformation was derived with a linear transducer, Philips L12-3, and the surgical navigation setup. The main goal of the calibration procedure is calculating the static transformation between the ORB placed on the pixel coordinates. Therefore, two calibration methods were performed of whom one succeeded. Within the PLUS software package, a N-wired phantom calibration method was described. Unfortunately, due to time limitation and calibration issues observed during the N-wired methodology the tracked pointer calibration method was chosen to be preferable. Before the calibration measurement took place, a 3D printed clip had to be derived.

Probe calibration was performed using the provided tracked pointer and the needle calibration method as provided by the PLUS and 3D Slicer Software packages. The conditions of this medium, in which calibration was performed, should match the speed of sound of 1540 m/s set by the US machine. The calibration procedure was performed using a water tank with the water at 18 degrees Celsius. According to Martin et al. a mixture of water and ethanol around 1:0.08 should provide a speed of sound comparable to the emitted US waves emitted by the transducer [88]. The water tank was filled with 7.5l of water and 0.6l of ethanol to provide the desired speed of sound. The calibration method was subdivided into a temporal and spatial calibration part.

Temporal Calibration

Temporal calibration was performed using the fCal software provided by the PLUS toolkit. Therewith, the US probe was moved up and down in the water tank in vertical manner at a constant speed of approximately 1cm/s that is comparable to an US sweep. The bottom of the tank was consistently detected by the algorithm. The temporal offset provided during the calibration method resulted in a sub-millisecond range and was therefore neglected. To conclude, the fusion between imaging and tracking data was assumed to be accurate.

Spatial Calibration

Spatial calibration was performed using the 'Fiducial Registration Wizzard' extension in 3D Slicer. This transformation includes translation, rotation and scaling and is defined as a non-rigid transformation. First the tracked tool tip was transformed to the probe coordination frame to correct for probe movements following equation 7.

$$p^{Probe}_{StylusTip} = p_{StylusTip} \, {}^{Stylus}T_{StylusTip} \, {}^{Tracker}T_{Stylus} \, {}^{Probe}T_{Tracker} \tag{7}$$

Second, the tool tip moves accordingly to the probe. The tracked tool is then manually aligned in the along the US frame, imaging the tool tip as shown in Figure 22c, and the US frame and tool tip location are saved. The p^{Probe}_{Image}, the position of the tool tip in the US frame is manually selected and saved accordingly. This procedure is repeated for all corners twice. Finally, the static transformation, ${}^{Probe}T_{Image}$, is calculated with an ICP registration linking the corresponding reference points tracked and found on US imaging together following equation 8.

$$p^{Probe}_{StylusTip} = p^{Probe}_{Image} \, ^{Probe}T_{Image}$$ (8)

The resulted static transformation is related to the depth used during calibration. For this latter, a 4-cm depth was found to be practical for the imaging acquisition of the tibia during this study no zoom correction was provided.

(a)   (b)   (c)
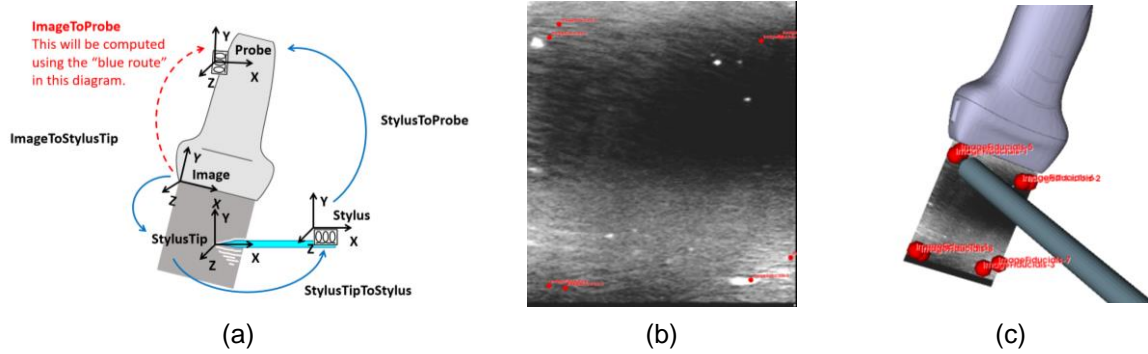
Figure 22: (a) Overview of transformation matrices. Retrieved and adjusted from Ungi et al. [86]. (b) US frame with the eight, in red, selected points corresponding to the tooltip. (c) 3D overview with the iUS frame, US probe and surgical pointer.

4.2.5 Registration

Surgical accuracy of the proposed system is computed, comparing the proposed registration with the gold standard. Both registrations are limited to a translational and rotational transformation only as the digitally 3D model should be in accordance with the physical dimensions. The complete workflow is shown in Figure 23.
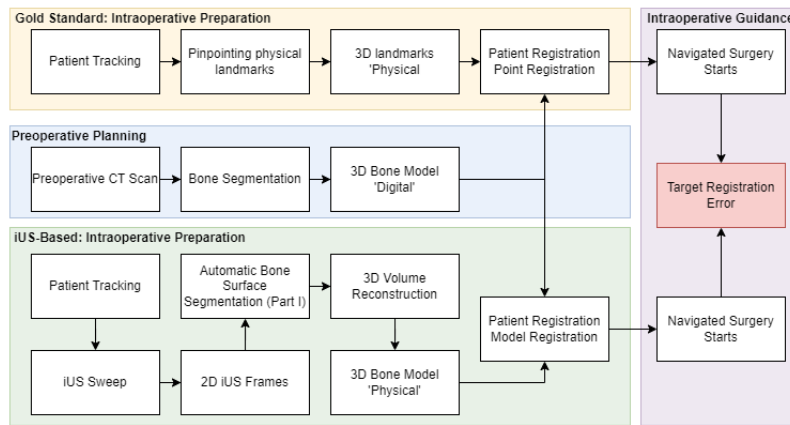
Figure 23: Schematic workflow for the experimental validation study. This study validates an iUS-based registration methodology (in green) with a Gold Standard registration (in yellow) to compute the target registration error (in red).

Gold Standard Registration

The gold standard registration requires the presence of the ORB in the 3D model. Therefore, the 3D model of the ORB was imported in the scene and placed at the correct position using the 'Fiducial Registration Wizzard' in 3D Slicer. The pivot points on the ORB 3D model were matched with the corresponding pivot points on the preoperative CT scan, as shown in Figure 24a-b.

The gold standard registration was done following an ICP registration. This registration can be performed within the standard extensions in the 3D Slicer software, the 'Fiducial Wizzard' Therefore, registration points were located at the distal end of the Kirschner wires (Figure 20-5) and three pivot points on the 3D-printed frame (Figure 20-6). The corresponding registration points in the 3D model are shown in Figure 24b. These points were registered in two steps with the corresponding physical points assigned with the surgical pointer. The required steps are listed below:
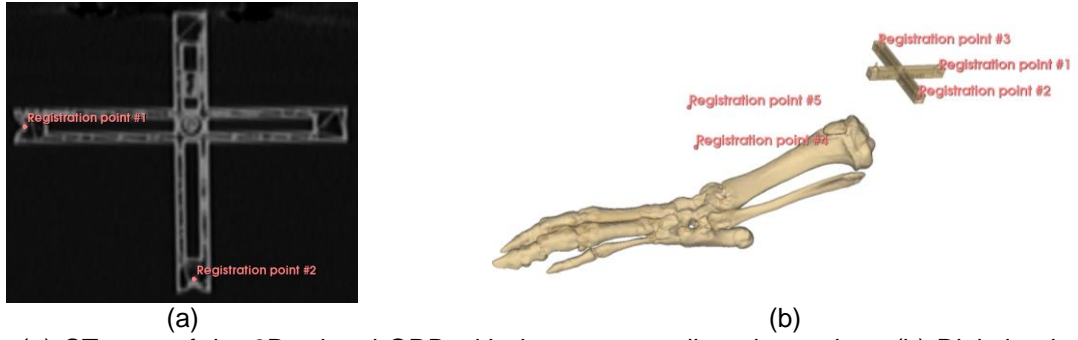
Figure 24: (a) CT-scan of the 3D printed ORB with the corresponding pivot points. (b) Digital points available for point registration to compute the gold standard registration.

Step 1: Find the registration points with the tracked tool and correct for movements of the cadaver. Therefore, the found points are tracked in consecutive order from StylusTip to Stylus to Tracker to the cadaver reference, indicated with the solid blue line in Figure 25. This consecutive transformation results in the following transformation operations:

$$p_{RegPoints,Physically}^{CadaverRef} = p_{RegPoints,Physically} \, ^{Stylus}T_{StylusTip} \, ^{Tracker}T_{Stylus} \, ^{CadaverRef}T_{Tracker} \tag{9}$$

Secondly, the detected registration points expressed in the coordination frame of the tracker, indicated with the blue dashed line in Figure 25 and the following transformation:

$$p_{RegPoints,Physically}^{Tracker} = p_{RegPoints,Physically}^{CadaverRef} \, ^{Tracker}T_{CadaverRef} \tag{10}$$

Step 2: Find the total transformation between the preoperative planning and the physically found registration points. First, the planning is linked to movements tracked by the cadaver reference, indicated with the orange solid line in Figure 25. Second, registration is performed to align the planning, preoperative imaging and 3D models, to the physically found registration points. Finally, this registration transforms the planning to the physical cadaver with movement correction by constant tracking of the cadaver reference frame.

$$p_{RegPoints,Digitially}^{Tracker} = p_{RegPoints,Digitially} \, ^{CadaverRef}T_{Cadaver} \, ^{Tracker}T_{CadaverRef} \tag{11}$$

$$^{CadaverRef}T_{Cadaver} = T_{Point\ registration} \tag{12}$$
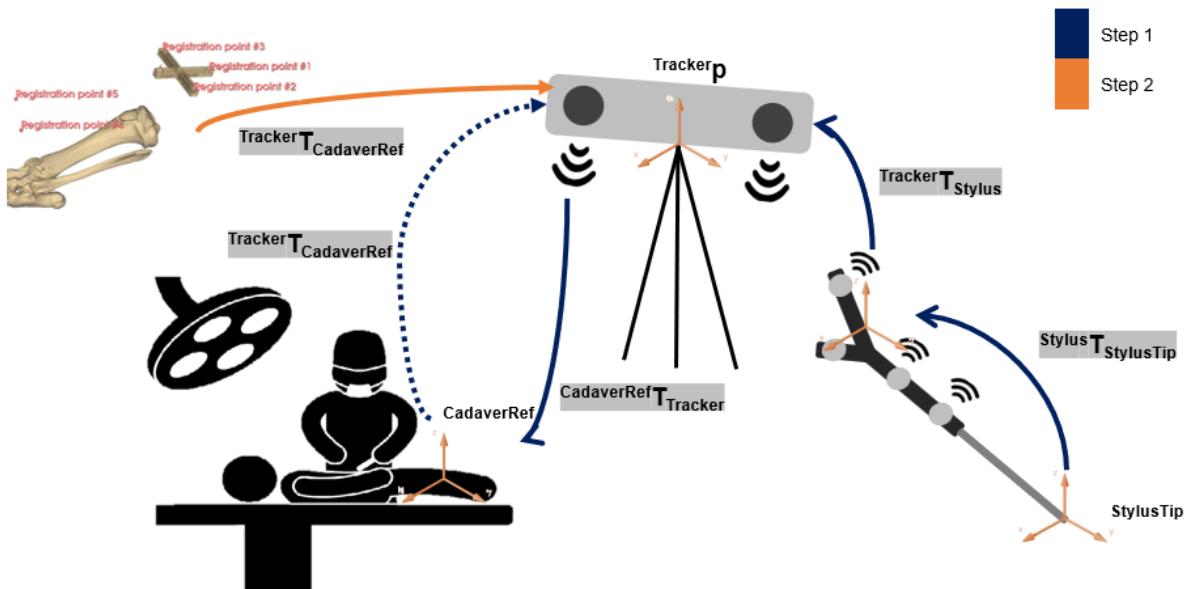
Figure 25: Schematic overview of all involved transformation required for the gold standard registration.

iUS-Based Cadaver Registration

The iUS-based registration consisted of several steps as shown in Figure 27. First, a second ORB was fixated in the proximal tibia with two Kirschner wires. This ORB used as cadaver reference should not be placed near the tumor, to avoid tumor contamination [31]. Image acquisition was performed with an iUS sweep on the skin of the cadaver. Secondly, the automatic segmentation algorithm detected the bone surface on every slice. Thirdly, the 3D bone surface was derived after 3D volume reconstruction. Finally, the preoperative 3D model based on the CT was registered to this intraoperatively determined 3D bone surface via a model-to-model registration in 3D Slicer. This model-to-model registration is based on an ICP registration to match to two-point cloud together (iterations = 200). Intraoperative navigation was achieved which gave positional feedback of the surgical pointer in correlation with the preoperative 3D model. Moreover, localization can be performed with the iUS superimposed with other available imaging modalities. Eventually, all components are expressed in the same coordination frame to link the preoperative planning, digitally, to the physical cadaver, captured with iUS, as shown in Figure 26. With the two bone surfaces in the same coordination frame, the final transformation can be computed $^{US}T_{CT}$ in the coordination frame of the tracker. Therefore, the following transformation steps are required:

Step 1: Find the accessible healthy bone surface with iUS and correct for movements. Therefore, the US pixels are tracked in consecutive order from probe to tracker to the cadaver reference, indicated with the solid blue line in Figure 26. This consecutive transformation results in the following transformation operations:

$$p^{CadaverRef}_{US\_Pixels} = p_{US\_Pixels} \, {}^{Probe}T_{Image} \, {}^{Tracker}T_{Probe} \, {}^{CadaverRef}T_{Tracker} \tag{13}$$

Secondly, the detected bone surface is expressed in the coordination frame of the tracker, indicated with the dashed blue line in Figure 26 and the following transformation:

$$p^{Tracker}_{US_{Pixels}} = p^{CadaverRef}_{US\_Pixels} \, {}^{Tracker}T_{CadaverRef} \tag{14}$$

Step 2: Find the total transformation between the preoperative planning and the detected bone surface. First, the planning is linked to movements tracked by the cadaver reference, indicated with the orange solid line in Figure 26. Second, a coarse initial point registration transforms the planning to the detected bone surface. Third, registration is performed to align the planning, preoperative imaging and 3D models, to the detected bone surface. Finally, this registration transforms the planning to the physical cadaver with movement correction by constant tracking of the cadaver reference frame.

$$p^{Tracker}_{Planning} = p_{Planning} \, {}^{CadaverRef}T_{Cadaver} \, {}^{Tracker}T_{CadaverRef} \tag{15}$$

$$^{CadaverRef}T_{Cadaver} = T_{Coarse\ point\ registration} T_{Model\ Registration} \tag{16}$$

Step 3: Tracked surgical tools such as pointers, oscillating saws and drills can be added to the total set-up following the green route shown in Figure 26. First, a static transformation is required between the tooltip and the tool reference computed with a calibration procedure. Second, the optical tracking system tracks the tool in the tracker coordination frame. Following this route, the iUS can be visualized in the navigation system also. Therefore, the following transformations are required:

$$p^{Tracker}_{Tooltip} = p_{Tooltip} \, {}^{ToolRef}T_{ToolTip} \, {}^{Tracker}T_{ToolRef} \tag{17}$$
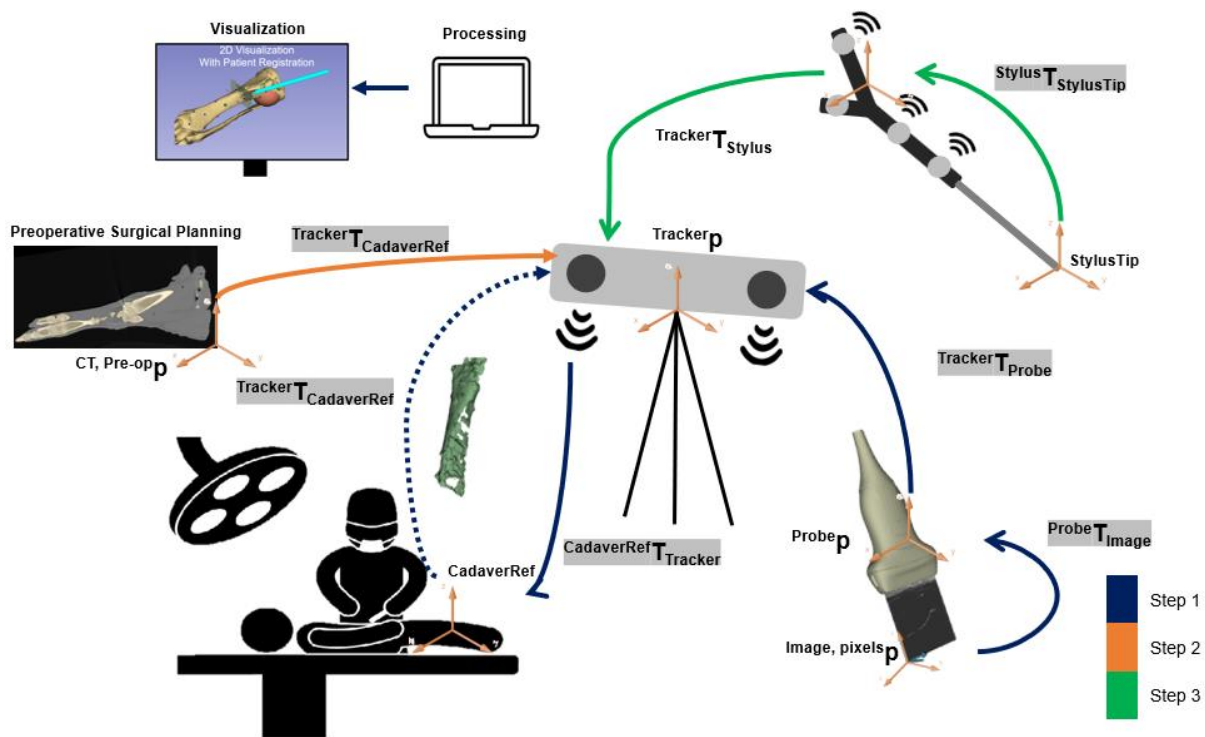
Figure 26: Schematic overview of all involved transformation required for the iUS-based registration.
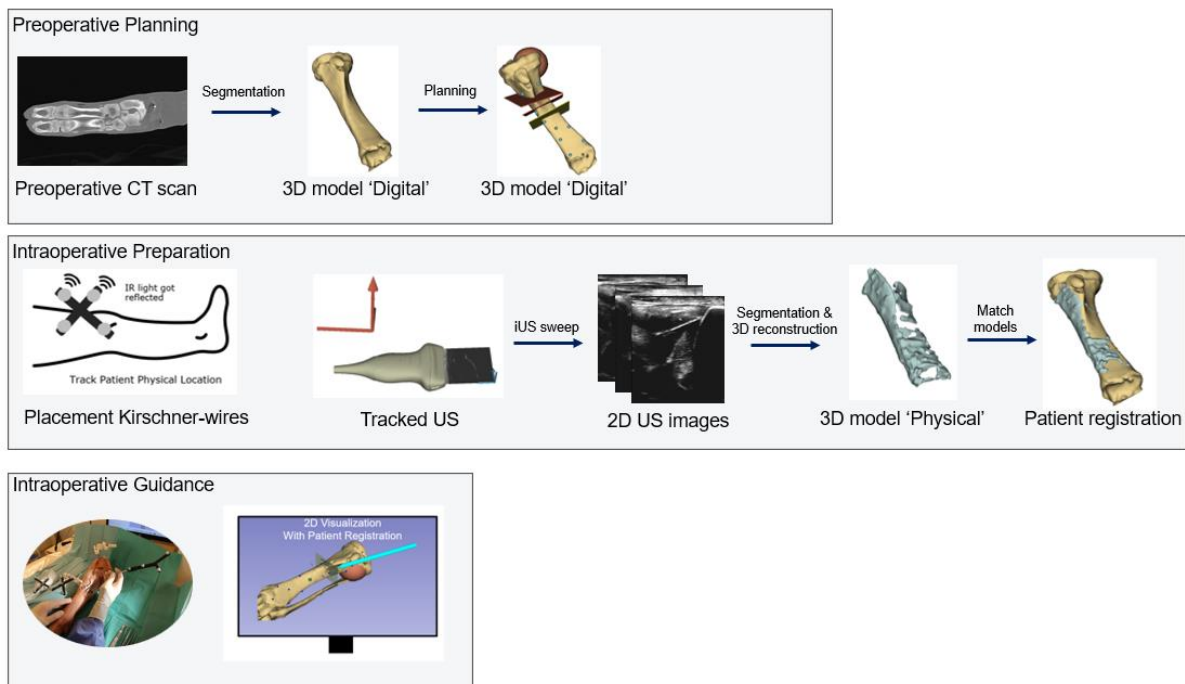
Figure 27: Workflow for the iUS-based cadaver registration.

The iUS acquisition must be performed on the non-affected bone surface as cadaver registration was performed using non-affected bone surface derived from the preoperative CT. Therefore, the lateral proximal part of the porcine tibia was considered as inaccessible due to the mimicked OS tumor during the experiments. The sweep was performed on all accessible bone surface available while maintaining accurate tracking. Therefore, the dorsal parts were not available for image acquisition as a matter the ORBs were located on the ventral side. Moreover, the speed of the image acquisition was approximately 1 cm/sec. The scan parameters are shown in Table 10.

Table 10: Ultrasound parameters with the L12-3 linear (Philips) probe

Parameter:	Value:
Frequency	12 MHz
Depth	4 cm
Gain	30

4.2.6 Accuracy Evaluation

The accuracies of the US probe, the surgical pointer, and the gold standard were defined as root-mean-square (RMS) errors. The artificial surgical targets located at the bone surface were used to compute the registration accuracy. The surgical accuracy was derived by computing the Target Registration Error (TRE). The TRE defines the Euclidean distance between each surgical targets located by the GS and the iUS-based registration [89]. This resulted in ten TREs per cadaver, resulting in a total of 90 TREs.

Registration accuracy better than 5 mm was considered as clinical acceptable, and the registration was classified as successful. The derived data was tested for normality using a Saphiro-Wilk test in SPSS Statistics version 28 (IBM SPSS Statistics, New York, United States of America) [74]. The null hypothesis for normal distribution gets rejected if the p-value<0.05 and the median values were computed.

$$RMSE = \sqrt{\sum_{i=1}^{n} \frac{(\hat{y} - y_i)^2}{n}} \tag{18}$$

$$TRE = \|P_{iUS} - P_{CT}\| = \sqrt{(x_{iUS} - x_{CT})^2 + (y_{iUS} - y_{CT})^2 + (z_{iUS} - z_{CT})^2} \tag{19}$$
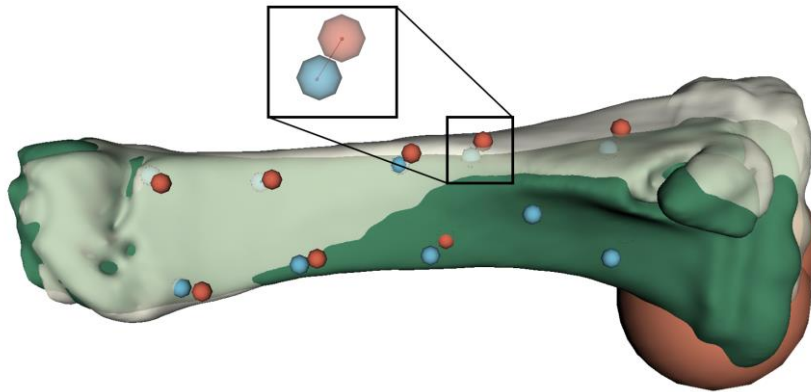
Figure 28: Target registration error calculation between gold standard registration, 3D model shown in green and corresponding blue surgical targets, and the iUS-based registration (CT), 3D model shown in white and corresponding red surgical targets.

4.3 Results

The Tracked US probe and surgical pointer were calibrated with an RMS error of 1.0 mm and 0.17 mm respectively. The golden reference registration, via ICP-point registration, was successful in all cadavers with a mean RMS of 1.70 mm (std = 0.17 mm).

The detected bone surfaces with iUS are shown in Figure 29. The amount of detected bone surface varies for the different acquisitions. The acquisition was limited to a lateral or medial bone plane only in four cases. The other cases involved more anatomical planes of the tibia. Ineffective tracking between both the US probe and the cadaver ORB was observed in 6/9. In one cadaver, tracking issues caused a mean TRE > 15 mm and this cadaver was therefore discarded for further analysis. Successful iUS-based registration (TRE < 5 mm) was found in 3/8 cadavers, as shown in Figure 30. The null hypothesis was accepted and therefore it was assumed that the data was normally distributed. The mean TREs were 7.83 mm (STD = 0.79 mm) and 6.78 mm (STD = 0.70 mm) for all cases and discarding cadaver 6, respectively. The maximum and minimum observed TRE were 0.50 and 16.80, respectively. All TREs are shown in Appendix I.

The mean times for the US acquisition, automatic bone segmentation and model-to-model registration were 136 sec (std = 40 sec), 225 sec (std = 63 sec) and 919 sec (std = 418 sec), respectively.

Mean (STD)	*Mean (STD)*	*Mean (STD)*	*Mean (STD)*
1.73 mm (STD = 0.76 mm)	13.27 mm (STD = 2.64 mm)	7.36 mm (STD = 0.6 mm)	4.29 mm (STD = 1.6 mm)
(a)	(b)	(c)	(d)

Mean (STD)	*Mean (STD)*	*Mean (STD)*	*Mean (STD)*
9.05 mm (STD = 0.62 mm)	7.08 mm (STD = 1.44 mm)	9.07 mm (STD = 1.04 mm)	2.42 mm (STD = 0.37 mm)
(e)	(f)	(g)	(h)
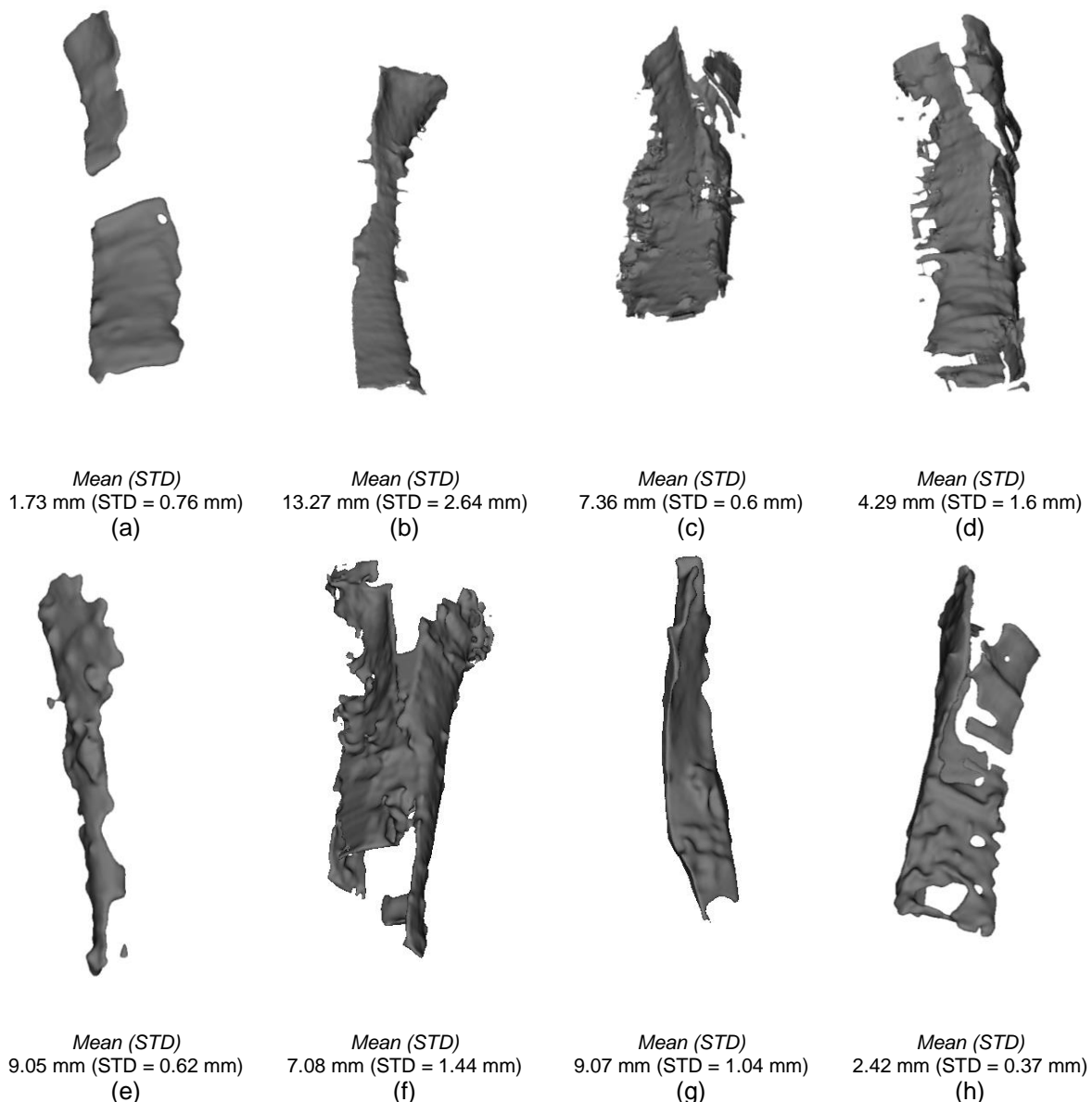
Figure 29: iUS detected bone surfaces with the corresponding median target registration error.
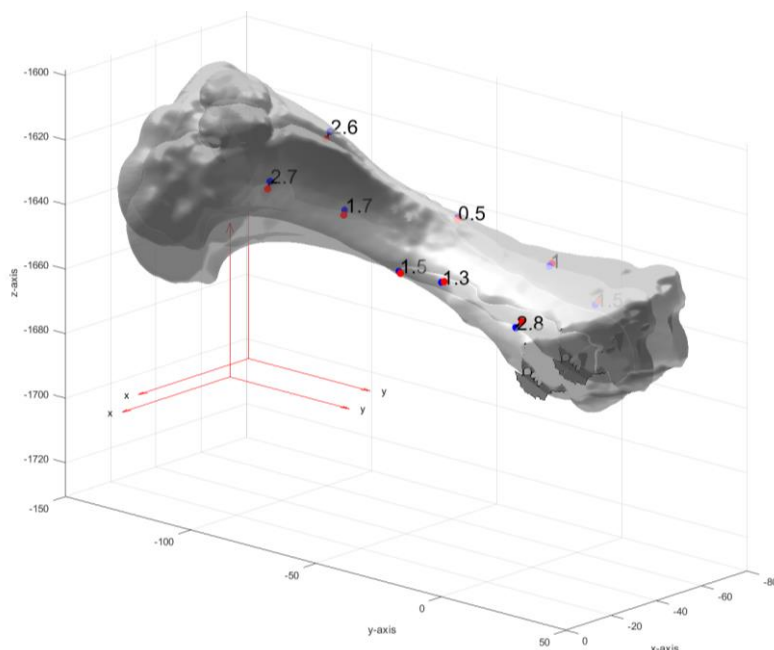
Figure 30: iUS-based registration with corresponding TREs for cadaver 9.

4.4 Discussion

During this study, an iUS-bone-based IGS system was validated with a median surgical accuracy of 7.18 mm (2.74 – 9.04 mm), with two best registrations of 1.50 mm (1.15 – 2.45 mm) and 2.35 mm (2.23 – 2.43 mm). The developed iUS-based cadaver registration could potentially substitutes the CBCT-based registration methods in future. Nevertheless, current system involves inacceptable accurcies and the system must be improved before clinical implementation.

The spatial iUS probe calibration was computed with the surgical tool, resulting in relatively accurate RMS-errors compared to literature. Comparable calibration errors were reported by Zhang et al. and Welch et al., with observed errors of 1.2 mm and 1.3 mm, respectively [84,90]. Although these authors reported comparable calibration errors, other studies observed errors of 2.4 mm up to 3.2 mm that might be caused by an increased imaging depth [80,91]. This implies that the observed RMS error (1.0 mm) of the US probe is in line with literature. Nevertheless, the iUS calibration might be affected since the procedure was performed once, at the start of the experiments only, resulting in inaccuracies over time. The experiments evolved over three weeks that may cause inaccuracies in the iUS calibration matrix due to the displacement of the 3D-printed reference clip attached to the probe. Unfortunately, the influence on the calibration accuracy has not been quantified nor corrected.

Relatively large TREs were observed during this study compared to the TREs smaller than 1 mm up to 4 mm found in comparable studies [49,76–78,92–95]. Fanti et al. showed in a phantom study a mean accurate registration error of 0.62 mm [76]. In this study, the authors included the joint plane of the tibia, resulting in more unique match between US-CT and thus improved accuracy. However, joint planes are clinically not feasible and this might decrease accuracy as confirmed in a human cadaver study performed by Wein et al. [94].

The observed TRE must be considered as an error propagation caused by probe calibration, tooltip calibration, GT calibration, iUS sweep tracking, automatic segmentation, 3D volume reconstruction, cadaver registration and the ultimate constant tracking of all objects. Therefore, minor random and systematic errors could significantly influence the final TRE. Several steps in the developed pipeline could cause this increase of observed TRE.

First, this study involved two optical references instead of one reference for both the gold standard and the iUS-based registration as used in a comparable porcine study [92]. Second, the mean RMS-error of the gold standard was 1.70 mm introducing a systematic error in the whole experimental setup. The found error of the gold standard was relatively large compared to Gueziri et al. who observed an error <1 mm [92]. The error could be caused as the CT scan and the experiment were not scheduled on the same day and the cadaver reference may have been shifted during transportation and storage.

Therefore, future research should implement one reference for both registration comparable to the experimental setup of Gueziri et al. [92].

Second, tracking issues were observed as the optical tracker had problems distinguishing between the three ORBs if the iUS probe was moved closely to another. In the beginning of the experiments, the ORB for the gold standard was placed at the midshaft of the tibia causing an inaccessible area for the iUS sweep. Therefore, the location of the ORB should be chosen carefully.

Third, the spherical markers were damaged after cleaning that was not noticed during the experiments. This damage was caused by removing of the reflecting layer by the cleaning products and the optical tracking system was not able to find the markers accurately. Consequently, these tracking issues affected the 3D reconstruction as the movements of the probe and the cadavers were not captured correctly.

Finally, the amount of detected bone surface available for iUS-based registration was various during this study. Ideally, more morphological bone features should be scanned that will result in a more accurately match with the CT derived surface. However, the amount of detected bone surface was not linked with better TRE as shown in Figure 29. This study observed a mismatch of ~1-2 mm between the bone surface segmented on CT and the surface segmented on the US frames causing these relatively large TREs. Therefore, post-procedural corrections were performed that resulted in an improved TRE of 1.5 mm and 2.35 mm for two cases.

Improved registration time could be a potential benefit of the proposed iUS-based registration. However, the developed workflow required relatively long registration times and must therefore be improved. Surgical workflow interruption can be divided into the placement of the cadaver reference plus the iUS sweep and the registration itself. Image acquisition was considered to be clinically reasonable (i.e., a mean sweep time of 136 seconds). Especially automatic segmentation and 3D volume reconstruction were time-consuming, and improvements are required for clinical implementation. Therefore, improvement can be done by efficient coding, implementation of the segmentation pipeline in 3D Slicer and improved 3D volume reconstruction. Ideally, registration may take less than 5 minutes in total with a patient interaction of less than 2.5 minutes for the iUS sweep. This might be feasible as Fanti et al. developed a comparable system that required eight minutes in total for registration [76]. Moreover, the system would be robust with minor operator interaction.

Non-invasive optical markers are more friendly to the patient with similar accuracies compared to Kirschner-wires [52,96]. Therefore, trackable markers can be attached to the patient's skin and used as patient references. Moreover, the use of non-invasive markers could result in less interruption of the surgical workflow. Nevertheless, Groen et al. observed inaccuracies in these markers as the skin shifts related to the bones after repositioning, especially in obese patients with a significant amount of subcutaneous fat [97,98]. However, as pediatric patients have mostly a thin layer of subcutaneous fat, skin markers could be beneficial for this patient group. Consequently, the advantages of these non-invasive skin markers should outweigh the potential cause of error due to non-rigid fixation compared to conventional Kirschner-wires. Further research should evaluate the advantages of non-invasive optical markers above the conventional invasive patient references.

This study has some limitations that need to be acknowledged. First, the SOS could have been influenced due to postmortem effects and the freezing and thawing of the cadaver, resulting in different physical acoustic behavior of US in the cadaver. Moreover, image acquisition occurred just after thawing of the cadaver instead of body temperature. To the knowledge of the author, an accurate correction of the SOS for the physical behavior of US in ex vivo porcine tissue compared to the SOS based on in vivo human tissue was not available for application during this study. Therefore, no correction for the cadaver specific SOS was performed during this study and depth perception of the bone surface may have been influenced that resulted in relatively large TRE. Future study should address the postmortem effects on the physical acoustic behavior of US in porcine tissue in relating to in vivo human tissue. Therefore, a SOS correction method should be provided by correlating the location of bone surface on US with the location on CT [99]. Second, present study involved a merely perfect automatic segmentation algorithm that resulted in raveled 3D volume reconstructions. Third, the CT acquisition and the iUS sweeps were not performed on the same day that could influenced the results. Fourth, the performance of the proposed method was limited to the tibia only. Further research should evaluate the performance on different bone structures. Furthermore, the addressed technical shortcomings should be improved in further research to improve the navigational accuracy that is required for clinical implementation.

4.5 Conclusion

In this porcine cadaver study, an iUS-based surgical navigation system was developed. The derived system reported a mean TRE of 6.78 mm (STD = 0.70 mm) and the registration error did not exceed the 5 mm in 3/9 registrations. The mean time required for the cadaver registration times was 21 minutes, that exceed the maximum time for registration of 7.5 minutes. Nevertheless, the developed technique demonstrated a maximum patient interaction of 2.5 minutes during image acquisition that was as prerequisite for the registration. Further research should improve the technical performance and improve the time required for patient registration. Furthermore, the surgical feasibility of the developed system should be evaluated in a hands-on experimental setting.

Part III:

User-Experience

"Evaluation of Surgical Feasibility in a Porcine Cadaver Study"

5

Porcine Cadaver Study

Tracked Ultrasound Bone Surface Registration for Intraoperative Navigation during Pediatric Bone Tumor Resections with Soft tissue Components

J.M. van der Zee[1,2], M. Fitski[1,], M.A.J. van de Sande[1,3], M.A.D. Buser[1], M.A.J. Hiep[4], C.E.J. Terwisscha van Scheltinga[1], C.C.C. Hulsker[1], C.H. van den Bosch[1], C.P. van de Ven[1], L. van der Heijden[1], G.M.J. Bökkerink[1], M.H.W.A. Wijnen[1], F.J. Siepel[5] and A.F.W. van der Steeg[1]

[1] *Princess Máxima Center for Pediatric Oncologic, Utrecht, the Netherlands.*
[2] *Technical Medicine, TechMed Centre, University of Twente, Enschede, the Netherlands.*
[3] *Department of Orthopaedics, Leiden University Medical Center, Leiden, the Netherlands.*
[4] *Department of Surgical Oncologic, Netherlands Cancer Institute, Amsterdam, the Netherlands.*
[5] *Robotics and Mechatronics, TechMed Centre, University of Twente, Enschede, the Netherland.*

5.1 Introduction

Osteosarcoma (OS) is a rare primary malignant bone tumor that originates from mesenchymal cells and accounts for 15% of all cancers in pediatric patients [100]. The incidence of high-grade OS is 0.15 per 100.000 persons at 10-19 years of age, with an overall five-years survival rate between 50-66% [6,100–103] in The Netherlands. This pediatric cancer is commonly found in the extremities with a predisposed localization in the proximal tibia, distal femur and proximal humerus. Treatment involves multiple cycles of neoadjuvant chemotherapy followed by surgical removal of the tumor and subsequent adjuvant chemotherapy. The best surgical approach is determined based on local tumor extend and involvement of neurovascular structures, and whenever possible through a shared decision-making process together with the patients and their caregivers. Nowadays, limb salvage surgery is possible in ~90% of patients with OS in the extremities, but sometimes amputation is indicated. Also, in some localizations such as distal tibia, a below knee amputation may be preferred for better functional outcome compared to technically reconstructions and arthrodesis which are technically demanding. Although limb salvage surgery improves the patient's quality of life by maintaining the functionality of the limb, it can also pose surgical challenges due to the need for narrow resection margins which may increase the risk of local recurrence [16]. Furthermore, as soft tissue components of the tumor are present, they are often difficult to visualize or palpate, which requires extensive preoperative radiological planning.

To overcome these surgical challenges, image guided surgery (IGS) is often used in orthopedic surgery to help the surgeon navigate intraoperatively and it may improve surgical and oncological outcomes and eventually may reduce operating time. [104]. IGS based on imaging may be a valuable tool to assist the surgeon by translating the intraoperative situation with the preoperative planning. Importantly, it may aid in safe oncological margins while maintaining as much healthy tissue as possible, minimizing morbidity. Commercialized IGS systems often use pre-incisional registration to register the virtual model with the physical patient. This registration methodology requires insertion of Kirschner wires into the bone followed by an additional three-dimensional (3D) fluoroscopy scan. The surgical workflow gets interrupted, and the patient is exposed to additional radiation with this conventional registration method. Alternative registration methods could result in faster registration resulting in less interruption of the surgical workflow and lower radiation exposure for the patient. Also, if registration gets lost during

surgery, which is a common problem with the current registration methods, quick and fast re-registration should be easily accessible.

Tracked ultrasound combines positional information together with 2D ultrasound (US) image acquisition to derive a 3D volume reconstruction. This intraoperative US (iUS) can be used to find rigid physical anatomical registration features such as bone surface. The appearance of the bone surface on US is unique due to a large impedance difference between soft tissue and the relatively hard bone surface. This creates a specific acoustic shadow behind the bone surface which can be used for automatic bone surface detection [58,67,105]. Automatic segmentation of the bone surface together with 3D volume reconstruction serve as a new registration feature. Previous research has shown the potential of an iUS-based registration methodology with registration errors less than 5 mm between the virtual model and physical patient [49,76–78,92–94].

After registration, the surgeon will get navigational feedback on a conventional 2D screen that is comparable to a laparoscopic procedure. Especially, it was proven in terms of clinical value that the combination of a tracked surgical tool together with the 3D model aids in tumor localization assessed by surgeons [97,98,106]. Moreover, within the iUS-based IGS system the surgeon gets the ability to orientate the iUS together with the 3D model. Therewith, an iUS-based IGS system could result in more accurate localization of the soft tissue components during the surgical removal of OS by superimposing the iUS with preoperative imaging. In this study, an iUS-based IGS system as described in Chapter 4 was validated based on the localization performance and user-experience.

5.2 Method

This section describes the experimental validation of the previous derived iUS-based surgical system done by surgeons and orthopedists. This system involves the derived segmentation algorithm of Part I and iUS-based navigation system as prerequisites.

5.2.1 Hardware and Software

The ultrasound surgical navigation system as described in Chapter 4 was used during the porcine cadaver study. Therefore, the same hardware and software components were used during these experiments. A schematic overview of the whole experimental setup is shown in Figure 23.

5.2.2 Porcine Cadavers and iUS-based registration

The porcine cadavers together with the iUS-based registration as described in Chapter 3 were used in this study. Therefore, the mean TRE of the iUS-based registration was 6.78 mm (STD = 0.70). A schematic overview of the whole registration methodology is shown in Figure 31.
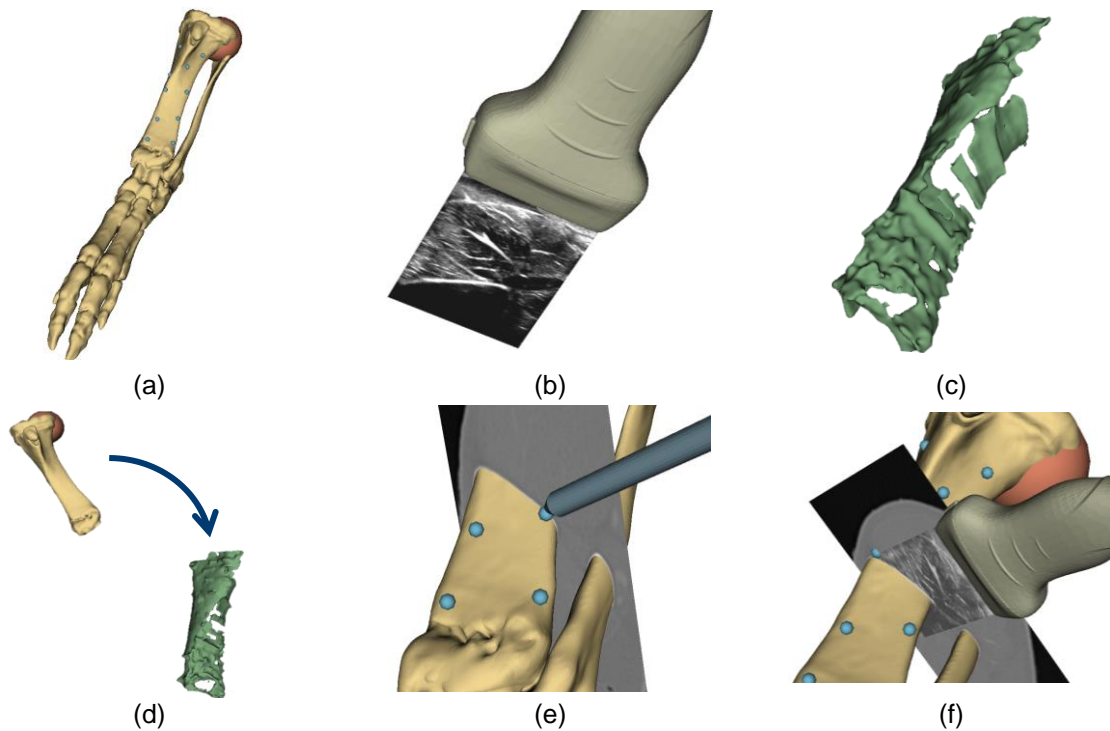
Figure 31: Overview of the registration method used by the iUS-based IGS system. (a) The preoperative derived 3D model with the artificial eccentric sphere-shaped tumor in the proximal tibia and the artificial surgical targets on the bone surface (blue dots) of the tibia. (b) iUS acquisition either over the skin or in the surgical wound bed. (c) The iUS derived bone surface after automatic segmentation and 3D volume reconstruction. (d) The model-to-model registration between the virtual planning (CT) with the physical cadaver (US). Intraoperative navigation with respect to the 3D model together with the surgical pointer (e) and with the iUS (f) superimposed with CT.

5.2.3 Participants and Experiment

Intraoperative validation was performed by six pediatric surgeons and two pediatric oncologic orthopedists, each operating a different cadaver. The participated pediatric oncologic orthopedists were familiar with optical based intraoperative navigation in their current clinical practice.

The previously derived 3D models were used as shown in Figure 32. An artificial eccentric circular-shaped tumor, mimicking an OS tumor in proximal tibia. Secondly, eleven artificial surgical targets were placed on the ventral side of the porcine bone surface. The experiment consisted of two phases:
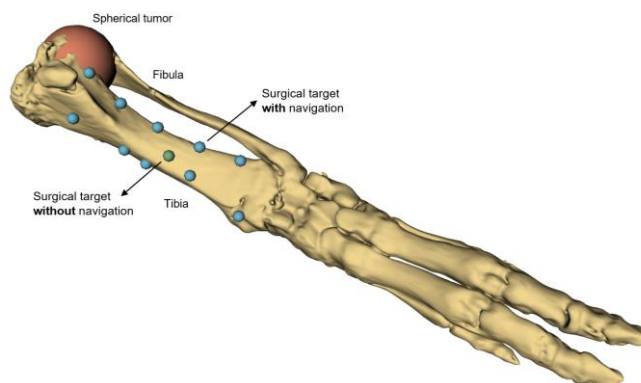
Figure 32: Surgical Planning

First, the surgeons were asked to localize a surgical target on the ventral side of the tibia. They were allowed to use every conventional localization method such as preoperative 2D- and 3D-imaging, palpation, visual inspection, conventional US and artificial fluoroscopy. The fluoroscopy was mimicked by placing the tracked surgical tool on the cadaver and visualizing the pointer as and 3D model. If the surgeons localized the surgical target, the found location was saved for further analysis.

Second, the surgeons were asked to localize ten surgical targets located on the bone surface of the tibia with the aid of iUS. Surgical incision was performed, and the surgical target were localized on the bone. The surgeons were allowed to use the IGS system with an interactive CT overlay regarding the tip of the surgical pointer during the experiment.

4.2.4 Accuracy Evaluation

Localization Accuracy

The accuracies of the US probe, the surgical pointer, and the golden standard were defined as RMS errors. The artificial surgical targets as located on the bone surface were used to compute the registration accuracy. Registration was classified as successful if the TRE was lower than 5 mm. These RMS errors and TREs were observed concluding the experiment as described in Chapter 4.

Secondly, the experimental Point Localization Error (PLE) was computed that defines the Euclidean distance between the located point by the surgeon and the location defined by either the golden registration or iUS-based registration. Resultingly, three experimental PLEs were computed for three situations:

$$PLE^1 = \left\| P_{iUS}^{Surgeon} - P_{CT}^{Planned} \right\| \tag{20}$$

The error defines the PLE between the point localized by the surgeon defined in the iUS-based registration compared to the location defined by the golden standard registration.

$$PLE^2 = \left\| P_{iUS}^{Surgeon} - P_{iUS}^{Planned} \right\| \tag{21}$$

The error defines the PLE between the point localized by the surgeon defined in the iUS-based registration compared to the location defined by the iUS-based registration.

$$PLE^3 = \left\| P_{CT}^{Surgeon} - P_{CT}^{Planned} \right\| \tag{22}$$

The error defines the PLE between the point localized by the surgeon defined in the golden standard registration compared to the location defined by the golden standard registration.

(a) (b)
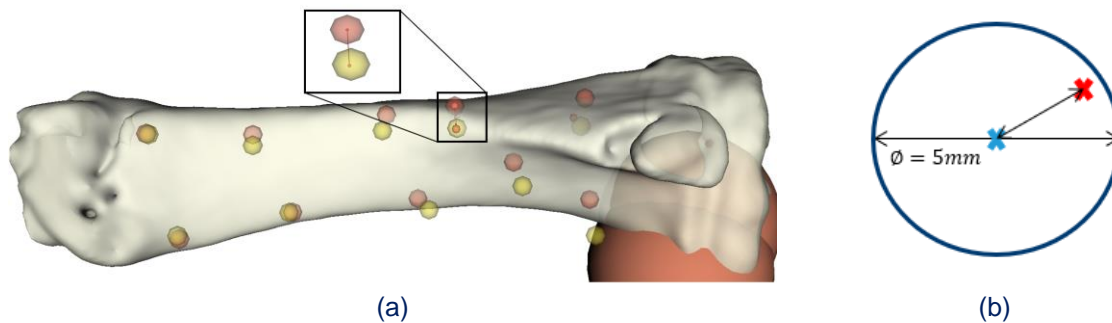
Figure 33: (a) Point localization error (PLE^2) calculation between point localized by the surgeon within the iUS-based registration, yellow surgical target, and the iUS-based registration, 3D model shown in white and corresponding red surgical targets. (b) Localized point within a surgical target.

Statistics

The derived data was tested for normality using a Saphiro-Wilk test in SPSS Statistics version 28 (IBM SPSS Statistics, New York, United States of America) [74]. The null hypothesis for normal distribution gets rejected if the p-value<0.05 and the median values were computed.

User-Experience

The participating surgeons were asked to score several statements on a 5-point Likert-scale ranging from '*Total disagree*' (1/5) up to '*Total agree*' (5/5) to evaluate the ease of the proposed IGS system. The statements involved in the post-procedural questionnaire are shown in Table 12.

5.3 Results

This section describes both the qualitative and the quantitative results of the conducted validation study.

Localization Accuracy

Localization without the aid of the surgical system occurred with conventional US (3/9), artificial fluoroscopy (3/9), palpation (9/9), visual inspection (9/9), 2D CT imaging (2/9), 3D model (9/9) and measurements (2/9). Subsequently, the surgeons localized one surgical target without the aid of the IGS system with a mean PLE of 11.8 mm (STD = 4.6 mm). According to the TREs found in Chapter 3, the results for one cadaver were discarded for further analysis.

The surgeons localized ten surgical targets that resulted in total of 90 attempts. The null hypothesis for normal distribution was rejected ($p<0.05$) in some cases. Therefore, the null hypothesis for the whole data set could not be approved and the data set was considered as a non-normal distribution. Resultingly, all attempts had a median of 9.25 mm (IQR = 4.91 – 13.81 mm), 5.90 mm (IQR = 2.25 – 6.93 mm) and 2.90 mm (2.80 – 5.05) for the PLE^1, PLE^2 and PLE^3, respectively. Moreover, post-procedural improvements of the iUS-based registration were performed that improved the PLE^1. The found PLEs with the aid of IGS are shown in Table 11. The results for each PLE per surgical target per cadaver are shown in Appendix J-M.

Table 11: Median Target Registration Errors and Point Localization Errors of proposed IGS system.

	PLE^1: iUS-CT (mm)	PLE^2: iUS-iUS (mm)	PLE^3: CT-CT (mm)
Cumulative (n = 8)	9.25 (4.91 – 13.81)	5.90 (2.25 – 6.93)	2.90 (2.80 – 5.05)
Cumulative (n = 8) Including post-procedure improvements	8.00 (3.86 – 8.96)	Not defined	Not defined

User-Experience

The surgeons agreed about the willingness for clinical implementation in their current clinical practice (5/5, IQR = 0). Moreover, they mentioned the additional clinical value of iUS in combination with the 3D model for the localization of involved soft tissue components by the tumor. Moreover, localization of the surgical targets felt to be faster (5/5, IQR = 1) and easier (5/5, IQR = 0) with the addition of this IGS system and the surgeons were even more confident (4/5, IQR = 2) about their actions. Finally, they agreed (5/5, IQR = 1) about the advantage of the minimal workflow interruption of this registration technique which allows for fast intraoperative re-registration. The results of the post-procedural questionnaire are shown in Table 12.

Table 12: Results of the post-procedural questionnaire

Statement	Median	IQR
1. I was confident about my localization of the surgical target	4	2
2. Localization with the aid of IGS was fast	5	1
3. Localization with the aid of IGS was easy	5	0
4. The proposed IGS is worth the additional time for registration	5	1
5. I would like to use the proposed IGS in my current practice	5	0

5.4 Discussion

During this study, an iUS-based surgical navigation system was validated within an experimental surgical setting using porcine cadavers performed by six pediatric surgeons and two pediatric orthopedic surgeons. The participating surgeons underlined the clinical added value of iUS as a registration feature and as intraoperative guidance in terms of registration time and intraoperative anatomical awareness, respectively.

The clinical relevance of tumor localization was evaluated during this study. Especially, the potential localization of soft tissue components, also during tumor resections of Ewing Sarcoma (ES), could be more accurate than with conventional IGS systems as they lack the localization of soft tissue components [21,107]. Moreover, the addition of iUS could serve as a more intuitive manner of US acquisition due to the direct interaction with the 3D model and the position of the US probe.

The participated surgeons agreed unanimously (IQR≤1) upon the statements that IGS resulted in a faster and easier surgical approach, worthwhile additional time required for the registration. Nevertheless, the surgeons showed no obvious agreement if localization was possible without the help of IGS. These observations of the user-experience for IGS were confirmed with a clinical study by Groen et al. [98]. In this study, surgeons were helped with an IGS during the resection of LRRC. Resulting from the post-procedural evaluation, the surgeons agreed that the surgery would have been possible without IGS, the procedure was faster, easier, and potentially increased the risk for radical resections. Although the use of IGS is not assumed to be essential for complex oncological surgery, these interventions would become faster and easier with the help of IGS techniques. Moreover, the help of IGS improves surgical decisiveness caused by an increase of anatomical awareness.

During this study relatively large PLEs were observed. Note, as a matter of fact that the PLE is directly coupled to the TRE, the surgeons could not perform better than this already stated TRE. Within this note, the surgeons performed within expectation as indicated with an ideal situation, the PLE^3. Moreover, the surgeons were asked to locate surgical targets at the porcine tibia, several causes can introduce increased PLE. First, in some cases, the surgical targets were physically unreachable. For instance, if the navigation has a dorsal-ventral shift of a few millimeters, the surgical targets appear to be located inside the bone instead of at the bone surface based on the navigation feedback. The other way around is possible as well. Second, the size of the spherical surgical targets introduces an error. The maximum error caused is equal to the radius of the sphere of the surgical target, as shown in Figure 33b. During the experiment, surgeons were satisfied if the pointer has reached a part of these spheres instead of reaching the ultimate center. The distraction of the radius of the surgical targets of the found PLEs could correct for this inevitable systematic error resulting in corrected errors of 5.65 mm, 2.40 mm and 0.40 mm for the PLE^1, PLE^2 and PLE^3, respectively.

The PLE^3 illustrates the surgical accuracy of the gold standard registration, and this concludes clinical performance with a corrected median PLE^3 of 0.40 mm. Concluding, small TREs will result in comparable PLEs and thus in an accurate and reliable system. Nevertheless, surgeons should be aware of the followed registration workflow and the corresponding cause of error [107]. Misinterpreting the navigational feedback could result in inaccurate resections instead of increased accuracy with subsequent adverse clinical outcomes. Moreover, the spatial 3D feedback given by the 2D display was sensitive for misinterpretation by the user.

The registration accuracy of an image guided surgery remains critical for accurate guidance during surgical challenging procedures. Inaccuracies could jeopardize surgical outcome creating adverse events. Although, an inevitable clinical accepted level of registration error deemed debatable, registration errors of <1 to 2 mm are currently reported for orthopedic oncology applications [52,108]. The clinical resection margins for the resection of soft tissue components is preferred to be 1-2c wherever possible [12]. Wide resection is not always possible due to close relation or involvement into surrounding structures such as neurovascular bundles, requiring a R1 resection. Nevertheless, the preferable resection margin of 1-2 cm results in a minimal clinical feasible registration accuracy and PLE of <5 mm and <10mm, respectively [12,109,110]. Therewith, the developed resulted in a clinical feasible system for three cadavers concluding the results of Chapter 4 which reported TRE < 5 mm. Consequently, the required PLE<10 mm was reported in five experiments for cadaver 4, 5, 7, 8 and 9. Nevertheless, the maximum PLE exceeded 1mm in three experiments. Therefore, the experiments resulted in a clinical feasible system in two experiments only, for cadaver 7 and 9.

Although the porcine tibia is obviously shorter than an adult human tibia, it could be of comparable length in pediatric patients [111]. Nevertheless, some anatomical differences between the human and porcine tibia are present. First, the lateral and medial condyles of the tibia are more distinctive in humans than found in porcine tibias. Moreover, this is also the case for the medial malleolus as this is more sharpened and relatively larger than in human tibias. The tibial tuberosity is comparable for both the human and porcine tibia. Final, the ventral side of the tibia is more flattened, resulting in a more cubic bone structure midshaft, in porcine than in human tibias. Although, these morphological differences, the performance of iUS-based registration could be relatively large influenced by a shorter tibia length than based on these morphological differences. Namely, short bone length with relatively closed placed ORBs resulted in tracking inaccuracies that influenced the registration performance present in current study.

Surgeons were able to familiarize themselves with the system shortly. However, the observer concluded that surgeons who use optical tracking-based navigation in their current practice had a significantly better understanding of the tracking system. This resulted in less optical obstruction of the optical references and better handling of the surgical tool during the experiment. Moreover, all surgeons agreed to get better handling and understanding throughout the experiments. Therefore, practice could make the difference in terms of handling and possibly in accuracy. Subsequently, potential learning effects during the experiment were observed as the accuracy improved during the experiments as shown with Figure 44 in the Appendix L. Although the decrease of PLE during the experiment could be caused by better handling during the experiments, some surgical targets were reported as more challenging than others by some of the participated surgeons. Especially, targets located at the distal part of the tibia or at bone edges resulted in relatively large PLEs.

This study has some limitations that need to be acknowledged. Although a surgical situation was simulated, this study was purely experimental as it lacked in the presence of an actual tumor, combined with tumor extent, due the inclusion of a porcine cadaver instead of an actual pediatric patient. Second, the surgical task performed by surgeons did not involve localization of soft tissue and/or moving targets. Therefore, the additional clinical value for localization of tumor extent in soft tissue components remains debatable. Further improvement of the technical setup and the surgical experiment are required to validate and strengthen the clinical relevance of this potential new surgical tool for the local treatment of OS.

5.5 Conclusion

This study evaluated the surgical feasibility of an iUS-based registration methodology for an IGS system in an experimental porcine cadaver study. The mean error of the localization of the artificial surgical targets without navigation was 11.8 mm (STD = 4.6 mm) and localization with the developed surgical system resulted in a median error of 8.00 mm (3.86 – 8.96 mm). The participated surgeons were unanimously satisfied about the interaction between the iUS and the 3D model and the relatively fast registration method compared to commercial IGS systems. The use of iUS during the localization of OS tumor extent in soft tissue components could be valuable. Further research is needed to improve the technical performance and address the limitations of this study before the proposed system can be embedded into the clinical practice.

6

General Discussion and Implementation

This chapter highlights several aspects before the proposed surgical navigation technique can be clinically implemented in the Princess Máxima Center within the surgical department. Therefore, the technical improvements required for an accurate and straightforward surgical navigation system are discussed. Second, the position of the proposed system in the surgical department will be highlighted. In this section, the application of the developed surgical system during the resection of other non-palpable, non-visible and/or complex-located extra-cranial solid tumors for all pediatric malignancies is evaluated.

6.1 Development

This chapter primarily evaluates the technical limitations of the current workflow that must be improved in further research and the limitations underlined in Chapters 4 and 5 must be considered in future work. Most importantly, the proposed setup should be improved to obtain a surgical tool that is straightforward and highly accessible before clinical implementation in the Princess Máxima Center. To conclude, these four improvements are assumed to be the most important:

First, the same optical reference should track both the iUS-based and gold standard ORBs. In the current setup, two optical references were involved that resulted in a potential random error. Moreover, using one ORB is in accordance with a comparable porcine study done by Guezeri et al. [77]

Second, automatic segmentation should be more precise to detect the bone surface at the same physical position compared to CT. In this study, the location of the US and CT based segmentation were different, and a systematic offset might be required. This observation could either be caused by misalignment of the bone surface by the segmentation algorithm or due to physical changes of US in cadavers. The current algorithm was trained with in vivo image data, acquired from humans, and during the validation experiment ex vivo image data, acquired from porcine cadavers, were used. Therefore, a potential 'systematic' offset implies a simple correction of a few pixels in either the US or CT segmentation. Nevertheless, the required correction was not quantified in this study. Moreover, quantification of this off-set was ineffective, caused by the observed tracking issues, that were not solved during experiments. Future work should evaluate the physical location of the bone surface on US image acquired with in vivo human tissue and ex vivo porcine tissue. Consequently, a direct link to the surface found by CT should be acquired. Possibly, the US probe could be scanned together with the cadaver in the CT scanner. This results in two scans that relates the bone surface after aligning these two scans, as shown in Figure 34 [99,112]. Moreover, the optical reflecting spheres must be replaced in case they are damaged.
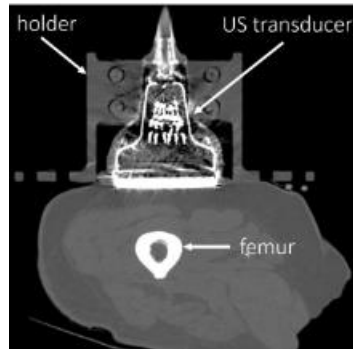
Figure 34: CT image of a cadaver together with an US transducer. (Retrieved from Rook [112])

Third, the iUS 3D volume reconstruction should be improved, resulting in a smoother bone surface. The obtained 3D reconstructed bone surface raveled, possibly caused by ineffective tracking or the segmentation. Improved volume reconstruction results in a better similarity of the bone surface with the CT-based segmentation, resulting in an increased registration accuracy. Moreover, the implementation of other registration techniques instead of the built-in rigid transformation of 3D Slicer could be evaluated in future work.

Fourth, surgical performance was evaluated with the PLE. Unfortunately, this poses inaccuracies as surgical satisfaction was achieved by locating the spherical target with the surgical pointer although the spherical center may not be reached yet. Therefore, the radius of these spheres introduces an error and could therefore be extracted. Moreover, experience of handling with an optical based surgical system by the operator may influences the observed PLE. The evaluation of the surgical performance should be reconsidered in future work.

6.2 Implementation

This chapter will evaluate the current proposed and developed navigation tool's potential clinical benefits and innovations.

The embedment of AR in orthopedic IGS is currently on the rise [113,114]. The use of AR could improve the spatial awareness of the surgeon as the surgeon perceives patient specific 3D models while looking at the patient, as shown in Figure 35a. Spijkerboer et al. developed an AR workflow that allows the pediatric surgeon to receive a holographic projection of the tumor at the child during the intraoperative preparation phase [115]. This workflow is currently embedded into the surgical management for Ewing Sarcoma in thoracic wall in the Princess Máxima Center, as these non-palpable tumors poses challenges defining the surgical incision in these patients. The early experiences in five patients can be found in Appendix B. However, this application lacks for stable visualization as the AR device appears to be sensitive to the angle of sight remaining accurate holographic projections, causing drift. This drift is assumed to be impractical for accurate intraoperative guidance. Nevertheless, AR improves the spatial awareness compared to 2D displays in the operating theatre as proposed in current study.

Receiving an accurate holographic projection is inevitable incorporated with accurate patient registration and accurate tracking. Conventional tracking strategies for AR devices incorporates quick-response (QR) codes, Aruco markers, Vuforia markers and outside-in-tracking as most often used tracking methods in IGS application. Currently, inside-out-tracking is upcoming that uses the infrared detectors of the AR device [116,117]. This upcoming tracking strategy results in a better accuracy and more robust holographic projections compared to the conventional tracking strategies. Although the implementation of AR has not been proposed in this study, integration of AR strategies as replacement for 2D display could be beneficial as shown in Figure 35b. Moreover, the visualization of the iUS could be integrated in the AR headset to provide a holographic imaging stream as shown in Figure 35c [118,119]. The surgeon will always remain a direct line of sight with the iUS probe. This may increase the anatomical awareness of the iUS acquisition intraoperatively. Future research should therefore implement AR visualization together with inside-out tracking to receive an accurate and robust holographic projection of the 3D models that is comparable to accuracies received with optical tracking systems used in this study.
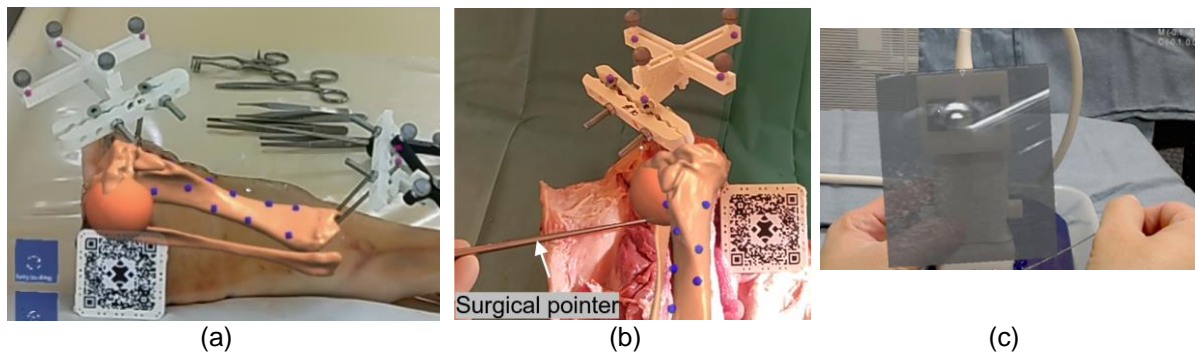
Figure 35: Preoperative (a) and intraoperative (b) holographic projection of the patient specific 3D model. (c) Holographic projection of an US stream onto the US probe to maintain a direct line of sight.

Current system requires a preoperative CT scan that can be superimposed with the iUS as shown in Figure 36a-b. Accurate fusion of preoperative derived imaging and real-time imaging could be beneficial for soft tissue localization as real-time feedback can be provided. However, the available imaging modality for superimposing is limited to the one used during patient registration (i.e., the preoperative CT scan). Therefore, the fusion of different preoperative image acquisitions could result in the addition of more anatomical and pathological information than provided solely by CT. For instance, visualization of the tumor extent in soft tissue is optimal on MRI and might be accessible if the MRI is registered to the CT [31]. Therefore, image registration should be implemented in the current preoperative phase for the optimal localization during the surgical management of OS. Within this registration, localization of the soft tissue components may be improved intraoperatively with the MRI. Moreover, the fusion with nuclear image could result in intraoperative localization for metabolic active sites of the tumor [120].
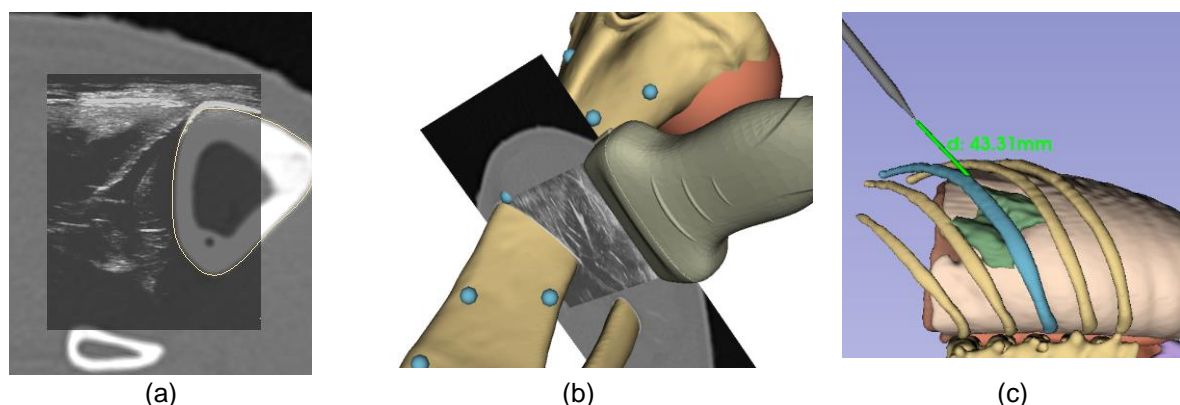
Figure 36: (a) Image fusion between iUS and preoperative derived CT. (b) Intraoperative navigational feedback of patient specific 3D model, surgical planning and the iUS with the superimposed preoperative CT scan. (c) Direct link between surgical pointer and surgical target during the resection of an Ewing Sarcoma in the thoracic wall.

Real-time 3D volume reconstruction of the tumor during surgery on iUS could enhance surgical decisiveness and localization capabilities even more. Therefore, real-time automatic tumor segmentation tools should be developed specific for the tumor type. For instance, in the surgical management of soft tissue sarcoma's the tumor extent is merely fixated to the bone and the proposed system currently does not correct for this soft tissue movements. In combination with accurate localization of these soft tissue components together with the proposed system, localization will be improved. Moreover, the addition of fluoresces image guided surgery could result in a final check-up of the presence of tumor cells in these soft tissues [121].

The surgical resection of metastatic lymph nodes, Wilms tumors, neuroblastomas, and germ-cell tumors, could be surgically challenging as these tumors are sometimes non-palpable, very small, non-visible and/or difficult located. In adults, comparable surgical challenges are present during the resection and localization of mama-carcinomas, liver tumors, and rectal cancer related metastatic lymph nodes. Nijkamp et al. first published the results of a prospective patient study that proofed the feasibility of an EM-based surgical system that helps the surgeon to find complex located metastatic lymph nodes in the pelvic region [122]. Although this study evaluated the surgical feasibility of navigation in tumors

that are not fixated to bone, this setup lacked in the ability for the correction of tumor movements. Smit et al. developed an workflow that allows for active tracking and localization of liver tumors [123]. Although relatively large TRE were reported, the application of iUS-based navigation could lead to the application in deformable, non-rigid, tumor resections. Moreover, automatic segmentation of the surface of an organ could be helpful for organ registration instead of bone-based registration approaches.

The workflow developed by Smit et al. could be helpful in pediatric renal surgery (i.e., Wilms tumor resection or nephron-sparing surgery) [123]. Intraoperative navigation increases the intraoperative awareness of vital structures or the depth of the resection during nephron-sparing surgery. Therefore, automatic kidney surface segmentation algorithms could be required to match the kidney surface visualized with iUS with the preoperative derived 3D model [124]. Further research should address alternative methods for the placement of patient references on non-rigid structures such as organs, for the embedment of intraoperative navigation techniques in non-rigid and deformable applications.

Tissue biopsy for efficient tumor classification is crucial in the diagnostic workflow for pediatric malignancies. Therefore, most of the pediatric patients are scheduled for either an open approach or a closed approach, such as core-needle biopsy (CNB). In the Princess Máxima Center, accurate diagnosis were found with CNBs in all included patients according to a retrospective mono-center study of Bruinsma et al. [125]. Nevertheless, the proposed navigation technique could, combined with non-invasive reference markers, potentially be useful as an additional tool during complex CNBs. Guidance could decrease the number of attempts, increase the anatomical awareness of the radiologist, and reduce interventional time.

Present study did not involve a direct link between the surgical pointer and the desired surgical target due to limited computational power. Resultingly, the surgeons reported difficulties translating the image guidance to their actions. Therefore, the operator was asked to alter the camera angle in the navigation system to receive more 3D information and thus increase their spatial awareness. To overcome this observed limitation, a continue direct link between the surgical pointer and the desired surgical target should be provided in future work, as shown in Figure 36c.

The proposed IGS system might be of beneficial value to low-income countries, as the system requires a relatively low investment (between €5000 – €22000). This investment includes a frame grabber and an optical tracking system only, as any US device is assumed to be applicable in current workflow. Therefore, the developed system creates an opportunity for the implementation of intraoperative navigation to surgical departments in low-income countries for whom commercial IGS systems are inaccessible, due to the large investments and running costs.

Conclusion

This graduation project may be considered as a proof-of-concept study and a first experimental contact with an iUS-based IGS system for the pediatric surgeons in the Princess Máxima Center. Consequently, the clinical potential of IGS, combined with the evidence found in literature, resulted in unanimous satisfaction in the surgical team about the potential aid in tumor localization for non-palpable, very small, non-visible and difficult located tumors in pediatric patients. Therefore, the surgical team would like to continue with the exploration of the aided clinical value of surgical navigation techniques for pediatric patients. Consequently, the results of this graduation project have resulted in the potential collaboration with the Antoni van Leeuwenhoek Hospital and a grant proposal that will be submitted to the Foundation Children Cancer-free, KiKa, in June 2023. This grant proposal evaluates all future perspectives stated by the surgical department of the Princess Máxima Center resulting in the ORCAS study (**O**ncologic **R**esection of **C**omplex Pediatric Tumors using **A**ccurate Navigation Guided **S**urgery).

Implementing of surgical navigation techniques may result in more radical resections during surgical management of pediatric extra-cranial solid tumors in the Princess Máxima Center. Hopefully, the improvement of registration techniques results in the registration of deformable non-rigid structures. In the future, this research may result in intraoperative navigation on moving targets during the complex tumor resections.

7

General Conclusion

The main objective of this thesis was to improve the intraoperative translation of the preoperative surgical planning during the surgical treatment of pediatric OS with soft tissue components. Therefore, an iUS-based IGS system was developed, and the surgical feasibility was evaluated. In the first part, an automatic bone segmentation algorithm was developed that automatically finds the bone surface on US frames. The derived algorithm was assumed to be practical for sequential computation of 3D reconstructions of the bone surface and therefore implemented in the second part, the development of an iUS-based surgical navigation system. This system was validated on the tibia of nine porcine cadavers and resulted in a mean TRE of 6.78 mm (STD = 0.70 mm). Furthermore, in three registrations the reported error was less 5 mm.

Straightforward initial patient registration within 7.5 minutes was not achieved in present study. Although the image acquisition required less than 2.5 minutes, the total time for the initialization of the system exceeded the stated requirement. Therefore, the potential for accessible re-registration was deemed limited based on the extensive duration for patient registration.

The clinical relevance of the proposed system and the clinical relevance was unanimously underlined by the participated surgeons and orthopedists. The participated clinicians were convinced about faster and easier localization of the surgical targets during the experiments. Furthermore, the clinicians were satisfied with the intraoperative coupling of the iUS together with the 3D models. This coupling could help the localization of soft tissue components during pediatric bone sarcoma-related tumor resections.

In conclusion, the proposed iUS-based IGS system has the potential for intraoperative guidance during the surgical management of OS with soft tissue tumor extent. Moreover, the proposed system could overcome the current limitations of CBCT-based registration approaches. Therefore, further research is required to improve the current system to acquire a surgical system that meets the clinical requirements. Furthermore, the proposed system has the potential to provide intraoperative guidance during the resection of other pediatric malignancies than OS alone.

8

Bibliography

1. Choi, J.H.; Ro, J.Y. The 2020 WHO Classification of Tumors of Bone: An Updated Review. *Advances in Anatomic Pathology* **2021**, *28*, 119–138, doi:10.1097/PAP.0000000000000293.
2. Ritter, J.; Bielack, S.S. Osteosarcoma. *Annals of Oncology* **2010**, *21*, vii320–vii325, doi:10.1093/annonc/mdq276.
3. Anninga, J.K.; Gelderblom, H.; Fiocco, M.; Kroep, J.R.; Taminiau, A.H.M.; Hogendoorn, P.C.W.; Egeler, R.M. Chemotherapeutic Adjuvant Treatment for Osteosarcoma: Where Do We Stand? *European Journal of Cancer* **2011**, *47*, 2431–2445, doi:10.1016/j.ejca.2011.05.030.
4. Longhi, A.; Errani, C.; De Paolis, M.; Mercuri, M.; Bacci, G. Primary Bone Osteosarcoma in the Pediatric Age: State of the Art. *Cancer Treatment Reviews* **2006**, *32*, 423–436, doi:10.1016/j.ctrv.2006.05.005.
5. Mirabello, L.; Troisi, R.J.; Savage, S.A. Osteosarcoma Incidence and Survival Rates from 1973 to 2004: Data from the Surveillance, Epidemiology, and End Results Program. *Cancer* **2009**, *115*, 1531–1543, doi:10.1002/cncr.24121.
6. Strauss, S.J.; Frezza, A.M.; Abecassis, N.; Bajpai, J.; Bauer, S.; Biagini, R.; Bielack, S.; Blay, J.Y.; Bolle, S.; Bonvalot, S.; et al. Bone Sarcomas: ESMO–EURACAN–GENTURIS–ERN PaedCan Clinical Practice Guideline for Diagnosis, Treatment and Follow-Up. *Annals of Oncology* **2021**, *32*, 1520–1536, doi:10.1016/j.annonc.2021.08.1995.
7. Sobin, L.; Wittekind, C. *UICC-TNM Classificaton of Malignant Tumors.*; Wiley: New York, 2002;
8. Grimer, R.J. Surgical Options for Children with Osteosarcoma. *The Lancet Oncology* **2005**, *6*, 85–92, doi:10.1016/S1470-2045(05)01734-1.
9. Abrams, A.K.; Avedian, R.S.; Marina, N. Treating Pediatric Osteosarcoma: Recent Clinical Trial Evidence. *Clinical Investigation* **2013**, *3*, 967–978, doi:10.4155/cli.13.89.
10. Whelan, J. EURAMOS-1 Treatment Protocol 2009.
11. Whelan, J.S.; Bielack, S.S.; Marina, N.; Smeland, S.; Jovic, G.; Hook, J.M.; Krailo, M.; Anninga, J.; Butterfass-Bahloul, T.; Böhling, T.; et al. EURAMOS-1, an International Randomised Study for Osteosarcoma: Results from Pre-Randomisation Treatment. *Annals of Oncology* **2015**, *26*, 407–414, doi:10.1093/annonc/mdu526.
12. Agarwal, M.; G., M.; Nayak, P. Limb Salvage for Osteosarcoma: Current Status with a Review of Literature. In *Osteosarcoma*; InTech, 2012 ISBN 978-953-51-0506-0.
13. HILLMANN, A.; HOFFMANN, C.; GOSHEGER, G.; KRAKAU, H.; WINKELMANN, W. Malignant Tumor of the Distal Part of the Femur or the Proximal Part of the Tibia: Endoprosthetic Replacement or Rotationplasty. Functional Outcome and Quality-of-Life Measurements*. *JBJS* **1999**, *81*.
14. Kotz, R.; Salzer, M. Rotation-Plasty for Childhood Osteosarcoma of the Distal Part of the Femur. *JBJS* **1982**, *64*.
15. Sommerauer, L.; Phyo, A.; Pion, E.; Zucal, I.; Klingelhoefer, E.; Thu, S.; Win, T.; Khin, S.; Kyaw, T.; Zaw, H.H.; et al. Modified Borggreve–Van Nes-Winkelmann Rotationplasty for Surgery in Developing Countries. *BMC Surg* **2022**, *22*, 333, doi:10.1186/s12893-022-01780-z.
16. He, F.; Zhang, W.; Shen, Y.; Yu, P.; Bao, Q.; Wen, J.; Hu, C.; Qiu, S. Effects of Resection Margins on Local Recurrence of Osteosarcoma in Extremity and Pelvis: Systematic Review and Meta-Analysis. *International Journal of Surgery* **2016**, *36*, 283–292, doi:10.1016/j.ijsu.2016.11.016.
17. Rickles, A.S.; Dietz, D.W.; Chang, G.J.; Wexner, S.D.; Berho, M.E.; Remzi, F.H.; Greene, F.L.; Fleshman, J.W.; Abbas, M.A.; Peters, W.; et al. High Rate of Positive Circumferential Resection Margins Following Rectal Cancer Surgery: A Call to Action. *Annals of Surgery* **2015**, *262*, 891–898, doi:10.1097/SLA.0000000000001391.

18. Heriot, A.G.; Tekkis, P.P.; Darzi, A.; Mackay, J. Surgery for Local Recurrence of Rectal Cancer. *Colorect Dis* **2006**, *8*, 733–747, doi:10.1111/j.1463-1318.2006.01018.x.

19. Reijers, S.J.M.; Heerink, W.J.; Van Veen, R.; Nijkamp, J.; Hoetjes, N.J.; Schrage, Y.; Van Akkooi, A.; Beets, G.L.; Van Coevorden, F.; Ruers, T.J.M.; et al. Surgical Navigation for Challenging Recurrent or Pretreated Intra-abdominal and Pelvic Soft Tissue Sarcomas. *J Surg Oncol* **2021**, *124*, 1173–1181, doi:10.1002/jso.26624.

20. Bosma, S.E.; Cleven, A.H.G.; Dijkstra, P.D.S. Can Navigation Improve the Ability to Achieve Tumor-Free Margins in Pelvic and Sacral Primary Bone Sarcoma Resections? A Historically Controlled Study. *Clin Orthop Relat Res* **2019**, *477*, 1548–1559, doi:10.1097/CORR.0000000000000766.

21. Nandra, R.; Matharu, G.; Stevenson, J.; Parry, M.; Grimmer, R.; Jeys, L. Long-Term Outcomes after an Initial Experience of Computernavigated Resection of Primary Pelvic and Sacral Bone Tumours: Softtissue Margins Must Be Adequate to Reduce Local Recurrences. *The Bone & Joint Journal* **2019**, *101*, 484-490., doi:https://doi.org/10.1302/0301-620X.101B4.BJJ-2018-0981.R1.

22. Jeys, L.; Grimer, R.; Carter, S.; Tillman, R. Outcomes of Primary Bone Tumours of The Pelvis - The ROH Experience. *Orthopaedic Proceedings* **2012**, *94-B*, 39–39.

23. Fujiwara, T.; Kaneuchi, Y.; Stevenson, J.; Parry, M.; Kurisunkal, V.; Clark, R.; Tsuda, Y.; Laitinen, M.; Grimer, R.; Jeys, L. Navigation-Assisted Pelvic Resections and Reconstructions for Periacetabular Chondrosarcomas. *European Journal of Surgical Oncology* **2021**, *47*, 416–423, doi:10.1016/j.ejso.2020.05.025.

24. Laitinen, M.K.; Parry, M.C.; Albergo, J.I.; Grimer, R.J.; Jeys, L.M. Is Computer Navigation When Used in the Surgery of Iliosacral Pelvic Bone Tumours Safer for the Patient? *The Bone & Joint Journal* **2017**, *99-B*, 261–266, doi:10.1302/0301-620X.99B2.BJJ-2016-0149.R2.

25. Kok, E.N.D.; van Veen, R.; Groen, H.C.; Heerink, W.J.; Hoetjes, N.J.; van Werkhoven, E.; Beets, G.L.; Aalbers, A.G.J.; Kuhlmann, K.F.D.; Nijkamp, J.; et al. Association of Image-Guided Navigation With Complete Resection Rate in Patients With Locally Advanced Primary and Recurrent Rectal Cancer: A Nonrandomized Controlled Trial. *JAMA Netw Open* **2020**, *3*, doi:10.1001/jamanetworkopen.2020.8522.

26. Picci, P.; Sangiorgi, L.; Bahamonde, L.; Aluigi, P.; Bibiloni, J.; Zavatta, M.; Mercuri, M.; Briccoli, A.; Campanacci, M. Risk Factors for Local Recurrences after Limb-Salvage Surgery for High-Grade Osteosarcoma of the Extremities. *Annals of Oncology* **1997**, *8*, 899–903, doi:10.1023/A:1008230801849.

27. Farfalli, G.L.; Albergo, J.I.; Ritacco, L.E.; Ayerza, M.A.; Milano, F.E.; Aponte-Tinao, L.A. What Is the Expected Learning Curve in Computer-Assisted Navigation for Bone Tumor Resection? *Clinical Orthopaedics & Related Research* **2017**, *475*, 668–675, doi:10.1007/s11999-016-4761-z.

28. Jeys, L.; Matharu, G.S.; Nandra, R.S.; Grimer, R.J. Can Computer Navigation-Assisted Surgery Reduce the Risk of an Intralesional Margin and Reduce the Rate of Local Recurrence in Patients with a Tumour of the Pelvis or Sacrum? *The Bone & Joint Journal* **2013**, *95-B*, 1417–1424, doi:10.1302/0301-620X.95B10.31734.

29. Aponte-Tinao, L.; Ritacco, L.E.; Ayerza, M.A.; Muscolo, L.D.; Albergo, J.I.; Farfall, G.L. Does Intraoperative Navigation Assistance Improve Bone Tumor Resection and Allograft Reconstruction Results? *Clinical Orthopaedics & Related Research* **2015**, *473*, 796–804, doi:10.1007/s11999-014-3604-z.

30. Wong, K.C.; Kumta, S.M. Joint-Preserving Tumor Resection and Reconstruction Using Image-Guided Computer Navigation. *Clinical Orthopaedics & Related Research* **2013**, *471*, 762–773, doi:10.1007/s11999-012-2536-8.

31. Cho, H.S.; Oh, J.H.; Han, I.; Kim, H.-S. The Outcomes of Navigation-Assisted Bone Tumour Surgery. *THE JOURNAL OF BONE AND JOINT SURGERY* **2012**, *94*.

32. Li, J.; Shi, L.; Chen, G. Image Navigation Assisted Joint-Saving Surgery for Treatment of Bone Sarcoma around Knee in Skeletally Immature Patients. *Surgical Oncology* **2014**, *23*, 132–139, doi:10.1016/j.suronc.2014.04.004.

33. Franz, A.M.; Haidegger, T.; Birkfellner, W.; Cleary, K.; Peters, T.M.; Maier-Hein, L. Electromagnetic Tracking in Medicine—A Review of Technology, Validation, and Applications. *IEEE Trans. Med. Imaging* **2014**, *33*, 1702–1725, doi:10.1109/TMI.2014.2321777.

34. Sorriento, A.; Porfido, M.B.; Mazzoleni, S.; Calvosa, G.; Tenucci, M.; Ciuti, G.; Dario, P. Optical and Electromagnetic Tracking Systems for Biomedical Applications: A Critical Review on Potentialities and Limitations. *IEEE Rev. Biomed. Eng.* **2020**, *13*, 212–232, doi:10.1109/RBME.2019.2939091.

35. Fattori, G.; Lomax, A.J.; Weber, D.C.; Safai, S. Technical Assessment of the NDI Polaris Vega Optical Tracking System. *Radiat Oncol* **2021**, *16*, 87, doi:10.1186/s13014-021-01804-7.

36. Yaniv, Z.; Wilson, E.; Lindisch, D.; Cleary, K. Electromagnetic Tracking in the Clinical Environment: Electromagnetic Tracking in the Clinical Environment. *Med. Phys.* **2009**, *36*, 876–892, doi:10.1118/1.3075829.

37. Koivukangas, T.; Katisko, J.P.; Koivukangas, J.P. Technical Accuracy of Optical and the Electromagnetic Tracking Systems. *SpringerPlus* **2013**, *2*, 90, doi:10.1186/2193-1801-2-90.

38. Noltes, L. A Study into Laparoscopic Surgical Navigation for Colorectal Cancer Patients without a Hybrid Operating Room. M3 Technical Medicine Thesis, University of Twente, 2019.

39. Hiep, M.A.J. Tracked Ultrasound for Patient Registration in Surgical Navigation during Abdominal Cancer Surgery. M3 Technical Medicine Thesis, University of Twente, 2021.

40. Laugier, P.; Haïat, G. Bone Quantitative Ultrasound. In *Introduction to the Physics of Ultrasound*; Springer, 2010; pp. 29–45.

41. Prince, J.L.; Links, J.M. The Physics of Ultrasound. In *Medical Imaging Signals and Systems*; Pearson, 2015; pp. 335–366.

42. Mercier, L.; Lango, T.; Lindseth, F.; Louis Collins, D. A Review of Calibration Techniques for Freehand 3-D Ultrasound Systems. *Ultrasound in Medicine & Biology* **2005**, *31*, 587, doi:10.1016/j.ultrasmedbio.2005.03.001.

43. Amin, D.V.; Kanade, T.; Digioia, A.M.; Jaramaz, B. Ultrasound Registration of the Bone Surface for Surgical Navigation. *Computer Aided Surgery* **2003**, *8*, 1–16, doi:10.3109/10929080309146097.

44. van der Heijden, F. Surgical Navigation Techniques [Syllabus] 2022.

45. Besl, P.J. A Method for Registration of 3-D Shapes. *IEEE Transactions on Pattern Analysis and Machine Intelligence* **1992**, *14*, 239–256.

46. Rusinkiewicz, S.; Levoy, M. Efficient Variants of the ICP Algorithm [Conference Paper]. In Proceedings of the Proceedings Third International Conference on 3-D Digital Imaging and Modeling; IEEE Comput. Soc: Quebec City, Que., Canada, 2001; pp. 145–152.

47. Li, P.; Wang, R.; Wang, Y.; Tao, W. Evaluation of the ICP Algorithm in 3D Point Cloud Registration. *IEEE Access* **2020**, *8*, 68030–68048, doi:10.1109/ACCESS.2020.2986470.

48. Özbay, E.; Çınar, A. A Comparative Study of Object Classification Methods Using 3D Zernike Moment on 3D Point Clouds. *TS* **2019**, *36*, 549–555, doi:10.18280/ts.360610.

49. Brößner, P.; Hohlmann, B.; Welle, K.; Radermacher, K. Validation of Automated Ultrasound-Based Registration for Navigated Scaphoid Fixation. *Current Directions in Biomedical Engineering* **2021**, *7*, 5.

50. Zaman, A.; Park, S.H.; Bang, H.; Park, C.; Park, I.; Joung, S. Generative Approach for Data Augmentation for Deep Learning-Based Bone Surface Segmentation from Ultrasound Images. *Int J CARS* **2020**, *15*, 931–941, doi:10.1007/s11548-020-02192-1.

51. Fitski, M.; Meulstee, J.W.; Littooij, A.S.; van de Ven, C.P.; van der Steeg, A.F.W.; Wijnen, M.H.W.A. MRI-Based 3-Dimensional Visualization Workflow for the Preoperative Planning of Nephron-Sparing Surgery in Wilms' Tumor Surgery: A Pilot Study. *Journal of Healthcare Engineering* **2020**, *2020*, 8899049, doi:10.1155/2020/8899049.

52. Sahovaler, A.; Daly, M.J.; Chan, H.H.L.; Nayak, P.; Tzelnick, S.; Arkhangorodsky, M.; Qiu, J.; Weersink, R.; Irish, J.C.; Ferguson, P.; et al. Automatic Registration and Error Color Maps to Improve Accuracy for Navigated Bone Tumor Surgery Using Intraoperative Cone-Beam CT. *JBJS Open Access* **2022**, *7*, doi:10.2106/JBJS.OA.21.00140.

53. Szabo, TL. *Diagnostic Ultrasound Imaging Inside Out.*; 2th ed.; Elsevier, 2014;

54. Noble, J.A.; Boukerroui, D. Ultrasound Image Segmentation: A Survey. *IEEE Trans. Med. Imaging* **2006**, *25*, 987–1010, doi:10.1109/TMI.2006.877092.

55. Hacihaliloglu, I. Ultrasound Imaging and Segmentation of Bone Surfaces: A Review. *Technology* **2017**, *05*, 74–80, doi:10.1142/S2339547817300049.

56. Niu, K.; Homminga, J.; Sluiter, V.; Sprengers, A.; Verdonschot, N. Measuring Relative Positions and Orientations of the Tibia with Respect to the Femur Using One-Channel 3D-Tracked A-Mode Ultrasound Tracking System: A Cadaveric Study. *Medical Engineering & Physics* **2018**, *57*, 61–68, doi:10.1016/j.medengphy.2018.04.015.

57. Tümer, N.; Kok, A.C.; Vos, F.M.; Streekstra, G.J.; Askeland, C.; Tuijthof, G.J.M.; Zadpoor, A.A. Three-Dimensional Registration of Freehand-Tracked Ultrasound to CT Images of the Talocrural Joint. **2018**, 16.

58. Jia, R.; Mellon, S.; Hansjee, S.; Monk, A.P.; Murray, D.; Noble, J.A. Automatic Bone Segmentation in Ultrasound Images Using Local Phase Features and Dynamic Programming. **2016**, 1005–1008.

59. Anas, E.M.A.; Seitel, A.; Rasoulian, A.; John, P.St.; Ungi, T.; Lasso, A.; Darras, K.; Wilson, D.; Lessoway, V.A.; Fichtinger, G.; et al. Registration of a Statistical Model to Intraoperative Ultrasound for Scaphoid Screw Fixation. *Int J CARS* **2016**, *11*, 957–965, doi:10.1007/s11548-016-1370-y.

60. Foroughi, P.; Boctor, E.; Swartz, M.J.; Taylor, R.H.; Fichtinger, G. P6D-2 Ultrasound Bone Segmentation Using Dynamic Programming. *IEEE Ultrasonics Symposium* **2007**, 4.

61. Tran, D.; Rohling, R.N. Automatic Detection of Lumbar Anatomy in Ultrasound Images of Human Subjects. *IEEE Trans. Biomed. Eng.* **2010**, *57*, 2248–2256, doi:10.1109/TBME.2010.2048709.

62. Quader, N.; Hodgson, A.J.; Mulpuri, K.; Schaeffer, E.; Abugharbieh, R. Automatic Evaluation of Scan Adequacy and Dysplasia Metrics in 2-D Ultrasound Images of the Neonatal Hip. *Ultrasound in Medicine & Biology* **2017**, *43*, 1252–1262, doi:10.1016/j.ultrasmedbio.2017.01.012.

63. van Sloun, R.J.; Cohen, R.; Eldar, Y.C. Deep Learning in Ultrasound Imaging. *Proceedings of Electrical and Electronics Engineering* **2019**, *108*.

64. Alsinan, A.; Vives, M.; Patel, V.; Hacihaliloglu, I. Spine Surface Segmentation from Ultrasound Using Multi-Feature Guided CNN [Conference Paper].; 2019; pp. 6–0.

65. Hohlmann, B.; Glanz, J.; Radermacher, K. Segmentation of the Distal Femur in Ultrasound Images. *Current Directions in Biomedical Engineering* **2020**, *6*, 20200034, doi:10.1515/cdbme-2020-0034.

66. Luan, K.; Li, Z.; Li, J. An Efficient End-to-End CNN for Segmentation of Bone Surfaces from Ultrasound. *Computerized Medical Imaging and Graphics* **2020**, *84*, 101766, doi:10.1016/j.compmedimag.2020.101766.

67. Patel, H. Improved Automatic Bone Segmentation Using Large-Scale Simulated Ultrasound Data to Segment Real Ultrasound Bone Surface Data [Conference Paper].; Cincinnati, 2020.

68. Wang, P.; Vives, M.; Patel, V.M.; Hacihaliloglu, I. Robust Real-Time Bone Surfaces Segmentation from Ultrasound Using a Local Phase Tensor-Guided CNN. *Int J CARS* **2020**, *15*, 1127–1135, doi:10.1007/s11548-020-02184-1.

69. Pandey, P.U.; Quader, N.; Guy, P.; Garbi, R.; Hodgson, A.J. Ultrasound Bone Segmentation: A Scoping Review of Techniques and Validation Practices. *Ultrasound in Medicine & Biology* **2020**, *46*, 921–935, doi:10.1016/j.ultrasmedbio.2019.12.014.

70. Ronneberger, O.; Fischer, P.; Brox, T. U-Net: Convolutional Networks for Biomedical Image Segmentation [Conference Paper].; Springer: Munich, 2015; Vol. 9351, pp. 234–241.

71. Tirindelli, M.; Eilers, C.; Simson, W.; Paschali, M.; Azampour, M.F.; Navab, N. Rethinking Ultrasound Augmentation: A Physics-Inspired Approach [Conference Paper]. In Proceedings of the Medical Image Computing and Computer Assisted Intervention – MICCAI 2021; de Bruijne, M., Cattin, P.C., Cotin, S., Padoy, N., Speidel, S., Zheng, Y., Essert, C., Eds.; Springer International Publishing: Virtual, 2021; Vol. 12908, pp. 690–700.

72. Sørensen, T.J. *A Method of Establishing Groups of Equal Amplitude in Plant Sociology Based on Similarity of Species Content and Its Application to Analyses of the Vegetation on Danish Commons*; 5; Kongelige Danske Videnskabernes Selskab: Kobenhaven, 1948;

73. Guo, Z.; Bai, J.; Lu, Y.; Wang, X.; Cao, K.; Song, Q.; Sonka, M.; Yin, Y. DeepCenterline: A Multi-Task Fully Convolutional Network for Centerline Extraction [Conference Paper].; arXiv: Hong Kong, March 25 2019.

74. Shapiro, S.S.; Wilk, M.B. An Analysis of Variance Test for Normality (Complete Samples). *Biometrika* **1965**, *52*, 591, doi:10.2307/2333709.

75. Goodfellow, I.J.; Pouget-Abadie, J.; Mirza, M.; Xu, B.; Warde-Farley, D.; Ozair, S.; Courville, A.; Bengio, Y. Generative Adversarial Networks. *Advances in Neural Information Processing Systems* **2014**, 2672–2680.

76. Fanti, Z.; Torres, F.; Hazan-Lasri, E.; Gastelum-Strozzi, A.; Ruiz-Huerta, L.; Caballero-Ruiz, A.; Cosıo, F.A. Improved Surface-Based Registration of CT and Intraoperative 3D Ultrasound of Bones. *Journal of Healthcare Engineering* **2018**, 12.

77. Gueziri, H.-E.; Georgiopoulos, M.; Santaguida, C.; Collins, D.L. Ultrasound-Based Navigated Pedicle Screw Insertion without Intraoperative Radiation: Feasibility Study on Porcine Cadavers. *The Spine Journal* **2022**, *22*, 1408–1417, doi:10.1016/j.spinee.2022.04.014.

78. Ciganovic, M.; Ozdemir, F.; Pean, F.; Fuernstahl, P.; Tanner, C.; Goksel, O. Registration of 3D Freehand Ultrasound to a Bone Model for Orthopedic Procedures of the Forearm. *Int J CARS* **2018**, *13*, 827–836, doi:10.1007/s11548-018-1756-0.

79. Lindseth, F.; Langø, T.; Selbek, T.; Hansen, R.; Reinertsen, I.; Askeland, C.; Solheim, O.; Unsgard, G.; Marvik, R.; Nagelhus Hernes, A. Ultrasound-Based Guidance and Therapy. *Advancements and Breakthroughs in Ultrasound Imaging* **2013**, 27–82, doi:10.5772/55884.

80. Hsu, P.; Gee, A.H.; Treece, G.M. *Freehand 3D Ultrasound Calibration: A Review*; Springer, Berlin Heidelberg, 2009; ISBN https://doi.org/10.1007/978-3-540-68993-5_3.

81. Prager, R.W.; Rohling, R.N.; Gee, A.H.; Berman, L. Rapid Calibration for 3-D Freehand Ultrasound. *Ultrasound in Medicine & Biology* **1998**, *24*, 855–869, doi:10.1016/S0301-5629(98)00044-1.

82. Carbajal, G.; Lasso, A.; Gómez, Á.; Fichtinger, G. Improving N-Wire Phantom-Based Freehand Ultrasound Calibration. *Int J CARS* **2013**, *8*, 1063–1072, doi:10.1007/s11548-013-0904-9.

83. Zhang, Z. Iterative Point Matching for Registration of Free-Form Curves. *International Journal of Computer Vision* **1994**, *13*, 119–152.

84. Welch, M.; Andrea, J.; Ungi, T.; Fichtinger, G. Freehand Ultrasound Calibration: Phantom versus Tracked Pointer [Conference Paper].; Holmes, D.R., Yaniv, Z.R., Eds.; Orlando, March 14 2013; p. 86711C.

85. Brown, A.; Uneri, A.; Silva, T.D. Design and Validation of an Open-Source Library of Dynamic Reference Frames for Research and Education in Optical Tracking. *J. Med. Imag.* **2018**, *5*, 1, doi:10.1117/1.JMI.5.2.021215.

86. Ungi, T.; Lasso, A.; Fichtinger, G. Open-Source Platforms for Navigated Image-Guided Interventions. *Medical Image Analysis* **2016**, *33*, 181–186, doi:10.1016/j.media.2016.06.011.

87. Wen, T.; Wang, C.; Zhang, Y.; Zhou, S. A Novel Ultrasound Probe Spatial Calibration Method Using a Combined Phantom and Stylus. *Ultrasound in Medicine & Biology* **2020**, *46*, 2079–2089, doi:10.1016/j.ultrasmedbio.2020.03.018.

88. Martin, K.; Spinks, D. Measurement of the Speed of Sound in Ethanol/Water Mixtures. *Ultrasound in Medicine & Biology* **2001**, *27*, 289–291, doi:10.1016/S0301-5629(00)00331-8.

89. Hill, D.L.G.; Batchelor, P.G.; Holden, M.; Hawkes, D.J. Medical Image Registration. *Institute of Physics and Engineering in Medicine* **2001**, *46*.

90. Zhang, H.; Banovac, F.; White, A.; Cleary, K. Freehand 3D Ultrasound Calibration Using an Electromagnetically Tracked Needle [Conference Paper].; Cleary, K.R., Galloway, Jr., R.L., Eds.; San Diego, CA, March 2 2006; p. 61412M.

91. Vasconcelos, F.; Peebles, D.; Ourselin, S.; Stoyanov, D. Spatial Calibration of a 2D/3D Ultrasound Using a Tracked Needle. *Int J CARS* **2016**, *11*, 1091–1099, doi:10.1007/s11548-016-1392-5.

92. Gueziri, H.-E. Evaluation of an Ultrasound-Based Navigation System for Spine Neurosurgery: A Porcine Cadaver Study. *Frontiers in Oncology* **2021**, *11*, 10.

93. Gueziri, H.-E. Toward Real-Time Rigid Registration of Intra-Operative Ultrasound with Preoperative CT Images for Lumbar Spinal Fusion Surgery. *International Journal of Computer Assisted Radiology and Surgery* **2019**, 11.

94. Wein, W.; Karamalis, A.; Baumgartner, A.; Navab, N. Automatic Bone Detection and Soft Tissue Aware Ultrasound–CT Registration for Computer-Aided Orthopedic Surgery. **2015**, 9.

95. Penney, G.P.; Barratt, D.C.; Chan, C.S.K.; Slomczykowski, M.; Carter, T.J.; Edwards, P.J.; Hawkes, D.J. Cadaver Validation of Intensity-Based Ultrasound to CT Registration. *Medical Image Analysis* **2006**, *10*, 385–395, doi:10.1016/j.media.2006.01.003.

96. Zamora, R.; Punt, S.E.; Christman-Skieller, C.; Yildirim, C.; Shapton, J.C.; Conrad, E.U. Are Skin Fiducials Comparable to Bone Fiducials for Registration When Planning Navigation-Assisted Musculoskeletal Tumor Resections in a Cadaveric Simulated Tumor Model? *Clin Orthop Relat Res* **2019**, *477*, 2692–2701, doi:10.1097/CORR.0000000000000924.

97. NijkamP, J.; Kuhlmann, K.; Sonke, J.-J.; Ruers, T. Image-Guided Navigation Surgery for Pelvic Malignancies Using Electromagnetic Tracking [Conference Paper].; San Diego, California, United States, 2016; Vol. 2016.

98. Groen, H.C. Use of Image-Guided Surgical Navigation during Resection of Locally Recurrent Rectal Cancer. **2022**, 13.

99. Fontanarosa, D.; van der Meer, S.; Harris, E.; Verhaegen, F. A CT Based Correction Method for Speed of Sound Aberration for Ultrasound Based Image Guided Radiotherapy: Speed of Sound Aberration Correction in IGRT. *Med. Phys.* **2011**, *38*, 2665–2673, doi:10.1118/1.3583475.

100. Stiller, C.A.; Bielack, S.S.; Steliarova-Foucher, E. Bone Tumours in European Children and Adolescents, 1978-1997. Report from the Automated Childhood Cancer Information System Project. *European Journal of Cancer* **2006**, *Volume 42*, 2124–2135, doi:10.1016/j.ejca.2006.05.015.

101. Goedhart, L.M.; Ho, V.K.Y.; Ploegmakers, J.J.W.; van der Geest, I.C.M.; van de Sande, M.A.J.; Bramer, J.A.; Stevens, M.; Jutte, P.C. Bone Sarcoma Follow-up; a Nationwide Analysis of Oncological Events after Initial Treatment. *Journal of Bone Oncology* **2023**, *38*, 100466, doi:10.1016/j.jbo.2022.100466.

102. Goedhart, L.M.; Ho, V.K.Y.; Dijkstra, P.D.S.; Schreuder, H.W.B.; Schaap, G.R.; Ploegmakers, J.J.W.; van der Geest, I.C.M.; van de Sande, M.A.J.; Bramer, J.A.; Suurmeijer, A.J.H.; et al. Bone Sarcoma Incidence in the Netherlands. *Cancer Epidemiology* **2019**, *60*, 31–38, doi:10.1016/j.canep.2019.03.002.
103. Choi, Y. Patient-Specific Quality Assurance Using a 3D-Printed Chest Phantom for Intraoperative Radiotherapy in Breast Cancer. *Frontiers in Oncology* **2021**, *11*, 11.
104. Morris, G.V.; Stevenson, J.D.; Evans, S.; Parry, M.C.; Jeys, L. Navigation in Musculoskeletal Oncology: An Overview. *IJOO* **2018**, *52*, 22–30, doi:10.4103/ortho.IJOrtho_205_17.
105. Pandey, P. Fast and Automatic Bone Segmentation and Registration of 3D Ultrasound to CT for the Full Pelvic Anatomy: A Comparative Study. *International Journal of Computer Assisted Radiology and Surgery* **2018**, 11.
106. Kok, E.N.D. Accurate Surgical Navigation with Real-Time Tumor Tracking in Cancer Surgery. *npj Precision Oncology* **2020**, 7.
107. Wong, K.C. CAOS in Bone Tumor Surgery. In *Computer Assisted Orthopaedic Surgery for Hip and Knee*; Sugano, N., Ed.; Springer Singapore: Singapore, 2018; pp. 157–169 ISBN 978-981-10-5244-6.
108. Wong, K.-C.; Kumta, S.-M. Use of Computer Navigation in Orthopedic Oncology. *Curr Surg Rep* **2014**, *2*, 47, doi:10.1007/s40137-014-0047-0.
109. Sambri, A.; Caldari, E.; Fiore, M.; Zucchini, R.; Giannini, C.; Pirini, M.G.; Spinnato, P.; Cappelli, A.; Donati, D.M.; De Paolis, M. Margin Assessment in Soft Tissue Sarcomas: Review of the Literature. *Cancers* **2021**, *13*, 1687, doi:10.3390/cancers13071687.
110. Kandel, R.; Coakley, N.; Werier, J.; Engel, J.; Ghert, M.; Verma, S. Surgical Margins and Handling of Soft-Tissue Sarcoma in Extremities: A Clinical Practice Guideline. *Current Oncology* **2013**, *20*, 247–254, doi:10.3747/co.20.1308.
111. Adams, B.; Crabtree, P. Comparative Osteology. In; Academic Press, 2011 ISBN 978-0-12-388437-4.
112. Rook, A. Evaluation of Options to Improve Accurate Execution of Osteotomies of the Lower Limb. Graduation Thesis, University of Twente: Enschede, The Netherlands, 2022.
113. Zhao, Z.; Poyhonen, J.; Chen Cai, X.; Sophie Woodley Hooper, F.; Ma, Y.; Hu, Y.; Ren, H.; Song, W.; Tsz Ho Tse, Z. Augmented Reality Technology in Image-Guided Therapy: State-of-the-Art Review. *Proc Inst Mech Eng H* **2021**, *235*, 1386–1398, doi:10.1177/09544119211034357.
114. Casari, F.A.; Navab, N.; Hruby, L.A.; Kriechling, P.; Nakamura, R.; Tori, R.; de Lourdes dos Santos Nunes, F.; Queiroz, M.C.; Fürnstahl, P.; Farshad, M. Augmented Reality in Orthopedic Surgery Is Emerging from Proof of Concept Towards Clinical Studies: A Literature Review Explaining the Technology and Current State of the Art. *Curr Rev Musculoskelet Med* **2021**, *14*, 192–203, doi:10.1007/s12178-021-09699-3.
115. Spijkerboer, K.G.P.; Fitski, M.; Siepel, F.J.; Ven, C.P. van de; Steeg, A.F.W. van der Augmented Reality-Guided Localization of a Chest Wall Tumor in a Pediatric Patient. *European Journal of Cancer* **2022**, *170*, 103–105, doi:10.1016/j.ejca.2022.04.023.
116. Gsaxner, C.; Pepe, A.; Schmalstieg, D.; Li, J.; Egger, J. Inside-Out Instrument Tracking for Surgical Navigation in Augmented Reality. **2021**, 11.
117. Kunz, C.; Maurer, P.; Kees, F.; Henrich, P.; Marzi, C.; Hlaváč, M.; Schneider, M.; Mathis-Ullrich, F. Infrared Marker Tracking with the HoloLens for Neurosurgical Interventions. *Current Directions in Biomedical Engineering* **2020**, *6*, 20200027, doi:10.1515/cdbme-2020-0027.
118. Nguyen, T.; Plishker, W.; Matisoff, A.; Sharma, K.; Shekhar, R. HoloUS: Augmented Reality Visualization of Live Ultrasound Images Using HoloLens for Ultrasound-Guided Procedures. *Int J CARS* **2022**, *17*, 385–391, doi:10.1007/s11548-021-02526-7.
119. von Haxthausen, F.; Moreta-Martinez, R.; Pose Díez de la Lastra, A.; Pascau, J.; Ernst, F. UltrARsound: In Situ Visualization of Live Ultrasound Images Using HoloLens 2. *Int J CARS* **2022**, *17*, 2081–2091, doi:10.1007/s11548-022-02695-z.
120. Wong, K.C. Image Fusion for Computer-Assisted Bone Tumor Surgery. In *Computational Radiology for Orthopaedic Interventions*; Zheng, G., Li, S., Eds.; Lecture Notes in Computational Vision and Biomechanics; Springer International Publishing: Cham, 2016; Vol. 23, pp. 217–230 ISBN 978-3-319-23481-6.
121. Rijs, Z.; Jeremiasse, B.; Shifai, N.; Gelderblom, H.; Sier, C.F.M.; Vahrmeijer, A.L.; van Leeuwen, F.W.B.; van der Steeg, A.F.W.; van de Sande, M.A.J. Introducing Fluorescence-Guided Surgery for Pediatric Ewing, Osteo-, and Rhabdomyosarcomas: A Literature Review. *Biomedicines* **2021**, *9*, 1388, doi:10.3390/biomedicines9101388.

122. Nijkamp, J.; Kuhlmann, K.F.D.; Ivashchenko, O.; Pouw, B.; Hoetjes, N.; Lindenberg, M.A.; Aalbers, A.G.J.; Beets, G.L.; van Coevorden, F.; KoK, N.; et al. Prospective Study on Image-guided Navigation Surgery for Pelvic Malignancies. *J Surg Oncol* **2019**, *119*, 510–517, doi:10.1002/jso.25351.

123. Smit, J.N.; Kuhlmann, K.F.D.; Ivashchenko, O.V.; Thomson, B.R.; Langø, T.; Kok, N.F.M.; Fusaglia, M.; Ruers, T.J.M. Ultrasound-Based Navigation for Open Liver Surgery Using Active Liver Tracking. *Int J CARS* **2022**, *17*, 1765–1773, doi:10.1007/s11548-022-02659-3.

124. Leroy, A.; Mozer, P.; Payan, Y.; Troccaz, J. Intensity-Based Registration of Freehand 3D Ultrasound and CT-Scan Images of the Kidney. *Int J CARS* **2007**, *2*, 31–41, doi:10.1007/s11548-007-0077-5.

125. Bruinsma, R.S.; Nievelstein, R.A.J.; Littooij, A.S.; Vermeulen, M.A.; van de Ven, C.P.; van Noesel, M.M.; Wijnen, M.H.W.A.; van der Steeg, A.F.W.; de Krijger, R.R. Diagnostic Accuracy of Image-Guided Core Needle Biopsy of Non-Central Nervous System Tumors in Children. *Pediatric Blood Cancer* **2021**, *68*, doi:https://doi.org/10.1002/pbc.29179.

Appendices

Appendix A: CARS 2023 Submission 1

Has been **accepted** as poster presentation at the CARS 2023 congres in Munchen at 20-23 June 2023. Moreover, the manuscript is currently being peer-reviewed for publication in the corresponding International Journal of CARS.

Tracked Ultrasound Bone Surface Registration for Intraoperative Navigation during Pediatric Bone Tumor Resections with Soft tissue Components

J.M. van der Zee[1,2], M. Fitski[1,], M.A.J. van de Sande[1,3], M.A.D. Buser[1], M.A.J. Hiep[4], C.E.J. Terwisscha van Scheltinga[1], C.C.C. Hulsker[1], C.H. van den Bosch[1], C.P. van de Ven[1], L. van der Heijden[1], G.M.J. Bökkerink[1], M.H.W.A. Wijnen[1], F.J. Siepel[5] and A.F.W. van der Steeg[1]

[1] Princess Máxima Center for Pediatric Oncologic, Utrecht, the Netherlands.
[2] Technical Medicine, TechMed Centre, University of Twente, Enschede, the Netherlands.
[3] Department of Orthopaedics, Leiden University Medical Center, Leiden, the Netherlands.
[4] Department of Surgical Oncologic, Netherlands Cancer Institute, Amsterdam, the Netherlands.
[5] Robotics and Mechatronics, TechMed Centre, University of Twente, Enschede, the Netherland.

Keywords: Osteosarcoma, Ewing Sarcoma, Pediatric Oncologic, Image Guided Surgery, Tracked Ultrasound, Intraoperative Navigation

Abstract

Purpose: Resection of pediatric osteosarcoma in the extremities with soft tissue involvement presents surgical challenges due to difficult visualization and palpation of the tumor. Therefore, an adequate image-guided surgery (IGS) system is required for more accurate tumor resection. The use of a 3D model in combination with intraoperative tracked ultrasound (iUS) may enhance surgical decision-making. This study evaluates the clinical feasibility of iUS as a novel surgical tool using a porcine cadaver model.
Methods: First a 3D model of the porcine lower limb was created based on preoperative scans. Second, the bone surface of the tibia was automatically detected with an iUS by a sweep on the skin. The bone surface of the preoperative 3D model was then matched with the bone surface detected by the iUS. Ten artificial surgical targets were used to calculate the target registration error (TRE) to evaluate the registration accuracy. Intraoperative performance of this surgical tool was evaluated by six pediatric surgeons and two pediatric oncologic orthopedists. Finally, user-experience was assessed with a post-procedural questionnaire.
Results: Eight registration procedures were performed that showed median target registration error of 7.18 mm (IQR = 6.30 mm). The surgeons were more confident with this novel surgical tool about their actions, and they experienced tumor localization as fast and easy.
Conclusion: This study shows the feasibility of the use of iUS as an IGS method for the resection of osteosarcoma in the extremities with soft tissue components.

Introduction

Osteosarcoma (OS) is a rare primary malignant bone tumor in children and young adults that originates from mesenchymal cells [1]. The annual incidence of OS is 8-11 cases per million at 10-19 years of age [2]. The overall five-years survival rate between 50-66% in the Netherlands [3]. OS is commonly found in the extremities with a preference for the proximal tibia, distal femur and proximal humerus. Treatment

involves neoadjuvant chemotherapy regimen followed by surgical resection of the tumor and subsequent adjuvant chemotherapy. The best surgical approach is determined based on local tumor extension and involvement of neurovascular structures, and whenever possible through a shared decision-making process together with the patients and their caregivers. Nowadays, limb salvage surgery is possible in ~90% of patients with OS in the extremities, but sometimes amputation is indicated. Although limb salvage surgery improves the patient's quality of life by maintaining the functionality of the limb, it can pose surgical challenges due to the need for negative resection margins. When these margins are not achieved, the risk of local recurrence increases significantly [16]. Furthermore, when soft tissue components of the tumor are present, they are often difficult to visualize or palpate, which requires extensive preoperative surgical planning based on radiological imaging.

To overcome these surgical challenges, image guided surgery (IGS) is often used in orthopedic surgery to help the surgeon navigate intraoperatively [4]. This may improve surgical and oncological outcomes and eventually may reduce operating time. Importantly, it may aid in safe oncological margins while maintaining as much healthy tissue as possible, minimizing morbidity [5]. Commercialized IGS systems often use pre-incisional registration to match the virtual model with the physical patient. This registration methodology requires insertion of Kirschner wires into the bone followed by an additional three-dimensional (3D) fluoroscopy scan. The surgical workflow gets interrupted for ~20-30 minutes, and the patient is exposed to additional radiation. Alternative registration methods could result in faster registration resulting in less interruption of the surgical workflow and lower radiation exposure for the patient. Also, if registration becomes inaccurate during surgery, which is a frequent problem with the current registration methods, quick and fast re-registration should be easily accessible.

Intraoperative tracked ultrasound (iUS) combines image acquisition with real-time positional information. The iUS can be used to find rigid physical anatomical structures which are required for registration. Bone surface on US gives an unique appearance due to a large impedance difference between soft tissue and the hard bone surface. Therefore, automatic segmentation of the bone surface on iUS followed by 3D volume reconstruction, may serve as a novel registration feature. The technical feasibility of such iUS-based registration methodology, using the bone surface as registration feature, was proven in previous studies [49,76–78]. However, the clinical value of the proposed IGS system during OS resection, especially with involved soft tissue components, has not been proven yet. In this study, an iUS-based IGS system was developed and subsequently evaluated in a porcine cadaver study.

Method

Experimental Setup: The iUS imaging was performed with a Philips CX50 US (Philips, Best, the Netherlands) machine combined with a linear probe (Fig. 1a). The US images were streamed with a frame grabber (Epiphan System Inc, Ottowa, Canada) to a computer workstation (NVIDIA T600 4GB graphical card, 32GB Ram), as shown in Fig. 1c. Positional data of the US probe, surgical instruments and patient were captured by an optical tracking system (Northern Digital Inc., Waterloo, Ontario, Canada), as shown in Fig. 1b. An optical reference body was attached to the US probe with a 3D printed clip (Fig. 1g). The open-source PLUS Toolkit was used to stream both the tracking and imaging data to the open-source surgical navigation software program 3D Slicer. A calibration procedure between the pixel coordinates and the optical reference body was performed with a tracked needle calibration method prior to utilizing the IGS system. The surgical pointer), as shown in Fig. 1f, was calibrated through a pivot calibration procedure in the 3D Slicer software.
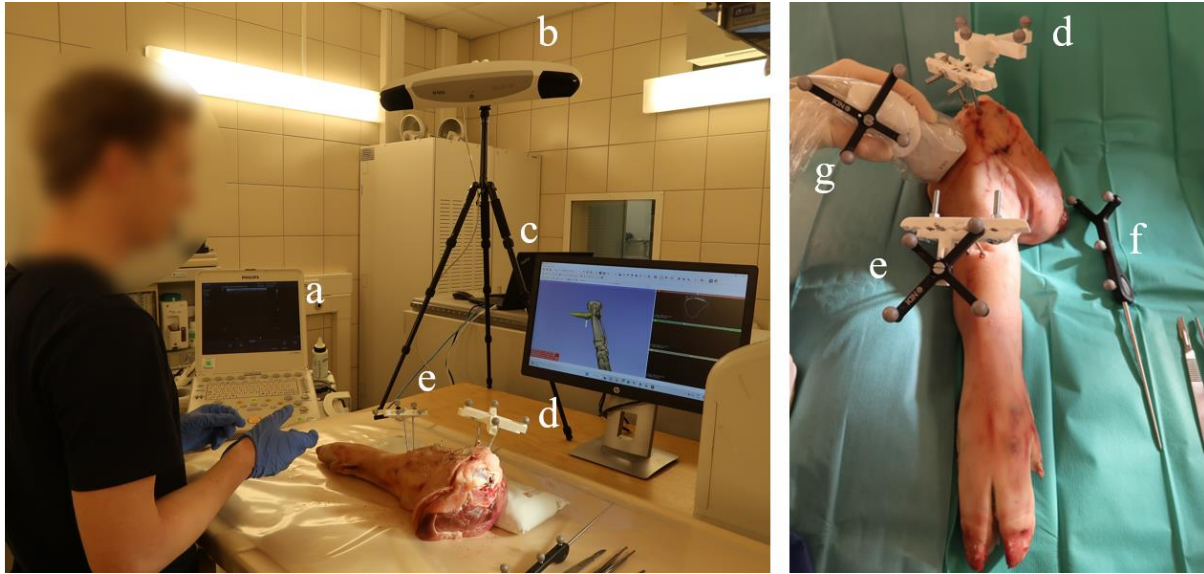
Figure 1: Overview of experimental setup

Automatic Segmentation: A fully automatic bone surface segmentation algorithm was developed using a 2D U-Net machine learning network. This network was trained and tested with 1085 B-mode US images with an 80:20 train:test split. Hyper-parameter optimization was performed. A batch size of 4, and an Adam optimizer with a learning rate of 1e-04 were optimal and thus chosen for this application. The included US images (Fig. 2a.) were acquired from the tibia, femur and humerus of four volunteers. Data augmentation of the trainings set was applied by adding randomly a Gaussian blur (sigma = 1.1) and a left-right flip for a quarter of the total set. Labeling of the dataset was done manually by an experienced Technical Physician (Fig. 2b). In addition to standard validation, the network was also tested on an independent dataset that included 942 images acquired from the tibia, femur, ribs, sternum and humerus of two volunteers. Finally, the network was evaluated based on the coverage percentage which calculates the percentage of the label that is detected by the network and the distance between the prediction and annotated bone surface (Fig. 2c).

| (a) | (b) | (c) |
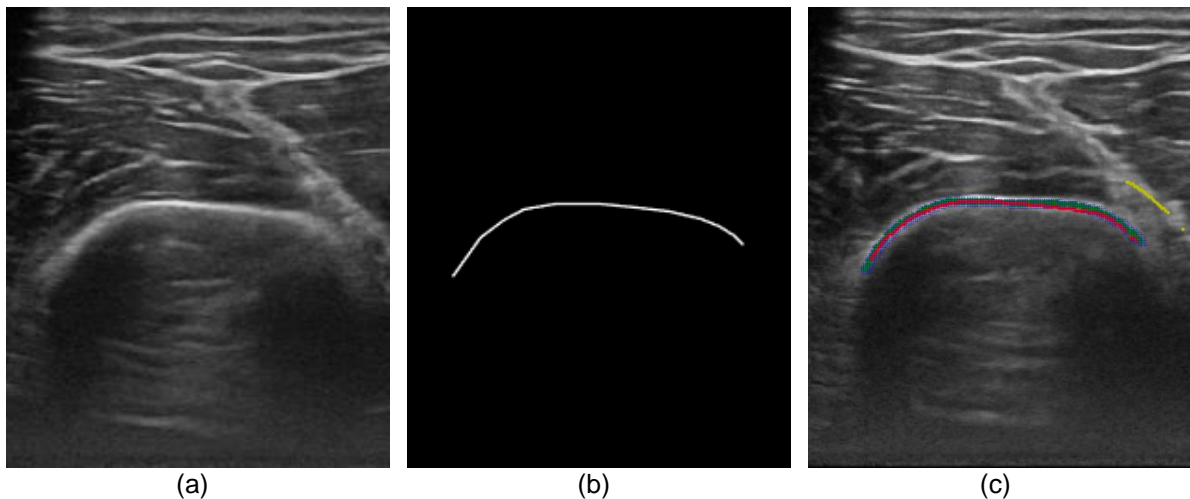
Figure 2: Automatic bone surface segmentation overview

Cadaver Experiment: The IGS method was validated using eight lower limbs derived from porcine cadavers. These cadavers were CT scanned (Siemens, Erlangen, Germany) with a fixated optical reference body (ORB) that served as the reference for the gold standard as shown in Fig. 1d. A preoperative 3D model of the bones was derived after segmentation by a threshold procedure using the preoperative derived CT in 3D Slicer. Ten artificial surgical targets were digitally defined on the bone

surface and one artificial eccentric circular-shaped tumor was placed in the distal tibia within this 3D model.

Registration: A gold standard and an iUS-based registration procedure had to be performed. The gold standard registration was done using an iterative closest point (ICP) registration. Digital and physical points were found on the preoperative imaging and assigned on the physical model with the surgical pointer. These points were located at the screw heads, Kirschner wires and three pivot points on the 3D printed frame. The iUS-based registration consisted of several steps as shown in Figure 3. First, a second ORB, (Fig. 1e), was fixated in the proximal tibia with two Kirschner wires. Within this reference frame, a pre-incisional iUS sweep was performed on the skin of the patient (Fig. 3b). Secondly, the bone surface on every slice was detected by the automatic segmentation algorithm. Thirdly, the 3D bone surface was derived after 3D volume reconstruction (Fig. 3c). Finally, the preoperative 3D model based on the CT was registered to this intraoperatively determined 3D bone surface via a model-to-model registration in 3D Slicer (Fig. 3c). Intraoperative navigation was achieved which gave positional feedback of the surgical pointer in correlation with the preoperative 3D model (Fig. 3e). Moreover, localization can be performed with the iUS superimposed with other available imaging modalities (Fig. 3f).
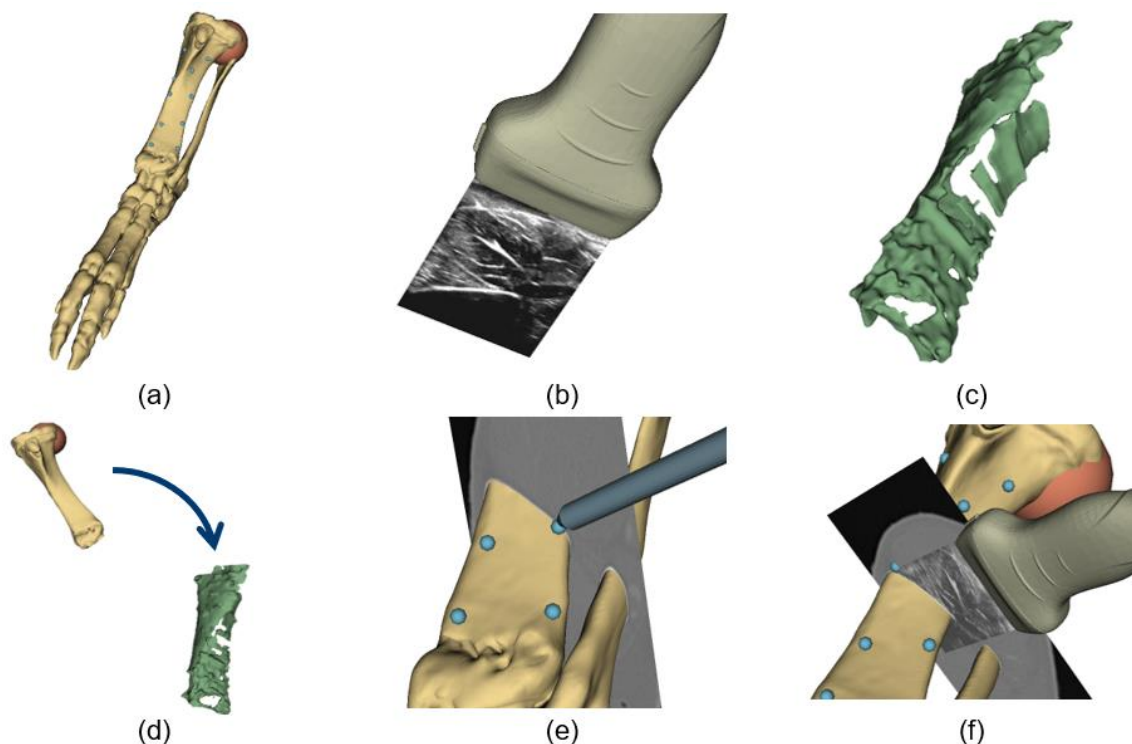
Figure 3: Overview of the registration method used by the iUS-based IGS system

User-Experience: Intraoperative evaluation was performed by six oncologic pediatric surgeons and two pediatric oncologic orthopedists, each operating a different cadaver. The surgeons were asked to localize one surgical target without the proposed IGS system and ten targets with the help of the IGS system. After determining the point of entry with all available imaging, they made an incision and localized the surgical target on the bone. Finally, to determine the ease of use and experience of the proposed IGS system, the participating surgeons were asked to score several statements on a 5-point Likert-scale ranging from '*Totally disagree'* (1/5) up to '*Totally agree'* (5/5). The median scores and their associated inter-quartile range (IQR) were reported per question.

Accuracy: The accuracies of the US probe, the surgical pointer, and the gold standard were defined as root-mean-square (RMS) errors. During the experiment, a Target Registration Error (TRE) was computed that defines the Euclidean distance between each surgical target located by the gold standard and the iUS-based registration. Registration was classified as successful if the TRE was lower than 5 mm.

Results

Automatic segmentation: The network predictions resulted in a median coverage percentage of 100% (100% - 100%) and a median distance between the annotated and detected bone surface of 1.18 mm (0.98 mm – 1.23 mm). The results for the independent dataset, specified per bone structure, can be found in Table 1. The results for these bone structures showed a cumulative median coverage percentage of 96% (92% - 98%) and a distance of 1.57 mm (1.39 mm – 1.83 mm).

Table 1: The results for the segmentation U-Net predictions in terms of the coverage perctentage and the distance between the labelled and the predicted bone surface

Data set	Coverage Percentage (%)			Distance (mm)		
	Median	25th percentile	75th percentile	Median	25th percentile	75th percentile
Test set	100.00	100.00	100.00	1.18	0.98	1.23
Sternum	97.82	95.01	100.00	1.44	1.07	1.73
Rib	92.62	96.07	97.62	1.45	1.15	1.84
Distal humerus	97.65	90.24	100.00	1.69	1.32	1.97
Distal femur	90.96	83.59	97.52	2.26	1.82	2.69
Proximal femur	95.00	87.50	100.00	1.68	1.40	1.95
Distal tibia	96.55	93.31	100.00	1.21	1.00	1.43

IGS System: The tracked US probe and surgical pointer were calibrated resulting in an RMS error of 1.0 mm and 0.17 mm, respectively. The gold standard registration had a mean RMS error of 1.70 mm (std = 0.17 mm). The eight registration procedures resulted in a median cumulative TRE of 7.18 mm (2.74 mm – 9.04 mm). Successful iUS-based registration (TRE < 5 mm) was found in 3/8 cadavers and a median TRE of 2.35 mm (1.50 mm – 3.90 mm) was reported for these cases. Ineffective tracking between both the US probe and the patient ORB was observed in 5/8 and this resulted in relatively large TREs. The mean times for the US acquisition, automatic bone segmentation and the 3D volume reconstruction followed by the model-to-model registration were 136 sec (std = 40 sec), 225 sec (std = 63 sec) and 919 sec (std = 418 sec), respectively.

User-Experience: The result from the post-procedural questionnaire can be found in Table 2. The surgeons agreed about their willingness for clinical implementation in the current clinical practice. Moreover, they mentioned the additional clinical value of iUS in combination with the 3D model for the localization soft tissue component as shown in Figure 3f. Localization of the surgical targets was felt to be fast and easy. Moreover, the surgeons even more confident with the addition of this IGS system about their actions. Finally, they agreed about the advantage of the minimal workflow interruption of this registration technique which allows for fast intraoperative re-registration in the surgical wound bed.

Table 2: Results of the post-procedural questionnaire

Statement	Median	IQR
1. I was confident about my localization of the surgical target	4	2
2. Localization with the aid of IGS was fast	5	1
3. Localization with the aid of IGS was easy	5	0
4. The proposed IGS is worth the additional time for registration	5	1
5. I would like to use the proposed IGS in my current practice	5	0

Discussion

During this study, an iUS-bone-based IGS system was developed and evaluated within a surgical setting in eight porcine cadavers by six pediatric surgeons and two pediatric orthopedic surgeons. Furthermore, the clinical additional value of iUS as a registration feature and as intraoperative guidance was underlined in terms of registration time and intraoperative anatomical awareness respectively. Especially, the possibility of localizing of the soft tissue components with the aid of iUS in combination with the preoperative 3D model (Fig. 3f) was accentuated by the surgeons. Moreover, they mentioned that this could also be helpful during the surgical treatment of other sarcomas such as Ewing Sarcoma or chondrosarcoma. Registration included the fixation of two Kirschner-wires in the healthy part of the affected bone and a pre-incisional iUS sweep. This resulted in short pre-incisional interruption of the surgical workflow. Moreover, because of this relatively fast and accessible registration, straightforward intraoperative re-registration is possible which can be performed even inside the surgical wound.

In this study several technical limitations were observed and these may have led to a relatively large TRE compared the accuracies reported in comparable literature [49,76–78]. Firstly, inaccurate tracking was observed as the optical tracker had problems to distinguish between the three ORBs (one for the US probe, the patient and the gold standard) which were placed in close proximity to each other.

Secondly, the amount of detected bone surface was limited during this study. The inclusion of more bone surface with more morphological features, if clinically feasible due to physical restrictions, could result in better TREs. Also, registration accuracy depends on the 3D volume acquired by automatic bone segmentation and the volume reconstruction. Mismatch between the bone surface based on the CT and the delineated iUS image of ~1-2 mm was detected. Network improvement in combination with registration and tracking improvement may result in a TREs less than 5 mm in future work that is a prerequisite for the clinical implementation of this proposed IGS system.

Conclusion

The current study showed the potential and feasibility of iUS-based registration methodology for an image-guided surgery (IGS) system using a porcine cadaver model. The surgeons who participated in this study were unanimously enthusiastic about the registration methodology. Moreover, the interaction between the iUS and the 3D model could be useful in the localization of the tumor and soft tissue components during the surgical treatment of OS.

References:

1. Choi JH, Ro JY (2021) The 2020 WHO Classification of Tumors of Bone: An Updated Review. Advances in Anatomic Pathology 28:119–138. https://doi.org/10.1097/pap.0000000000000293
2. Ritter J, Bielack SS (2010). Osteosarcoma. Annals of Oncologic 21(7):320-325 https://doi.org/10.1093/annonc/mdq276
3. Goedhart LM, Ho VKY, Dijkstra PDS, Schreuder HWB, Schaap GR, Pleogmakers JJW, van der Geest ICM, van de Sande MAJ, Bramer JA, Suurmeijer AJH, Jutte PC. (2019) Bone sarcoma incidence in the Netherlands. Cancer Epidemiology 60:31–38. https://doi.org/10.1016/j.canep.2019.03.002
4. McCulloch RA, Frisoni T, Kurunskal V, Donati DM, Jeys L (2021). Computer Navigation and 3D Printing in the Surgical Management of Bone Sarcoma. Cells 10(2):195. https://doi.org/10.3390/cells10020195
5. He F, Zhang W, Shen Y, Yu P, Bao Q, Wen J, Hu C, Qiu S (2016) Effects of resection margins on local recurrence of osteosarcoma in extremity and pelvis: Systematic review and meta-analysis. International Journal of Surgery 36:283–292. http://dx.doi.org/10.1016/j.ijsu.2016.11.016
6. Fanti Z, Torres F, Hazan-Lasri E, Gastelum-Strozzi A, Ruiz-Huerta L, Caballero-Ruiz A, Cosıo FA (2018) Improved Surface-Based Registration of CT and Intraoperative 3D Ultrasound of Bones. Journal of Healthcare Engineering. https://doi.org/10.1155/2018/2365178.
7. Gueziri H-E, Georgiopoulos M, Santaguida C, Collins DL (2022) Ultrasound-based navigated pedicle screw insertion without intraoperative radiation: feasibility study on porcine cadavers. The Spine Journal 22:1408–1417. https://doi.org/10.1016/j.spinee.2022.04.014
8. Brößner P, Hohlmann B, Welle K, Radermacher K. (2021). Validation of Automated Ultrasound-based Registration for Navigated Scaphoid Fixation. Current Directions in Biomedical Engineering 7(1):116-120. https://doi.org/10.1515/cdbme-2021-1025
9. Ciganovic M, Ozdemir F, Pean F, Fuernstahl P, Tanner C, Goksel O (2018) Registration of 3D freehand ultrasound to a bone model for orthopedic procedures of the forearm. Int J CARS 13:827–836. https://doi.org/10.1007/s11548-018-1756-0

Has been **accepted** as an oral presentation at the CARS 2023 congres in Munchen at 20-23 June 2023.

Augmented Reality guidance for the surgical localization of pediatric chest wall tumors

Rémi van der Woude[1,2], Jasper M. van der Zee[1,2], Matthijs Fitski[1], Cornelis P. van de Ven[1], Marc H. W. A. Wijnen[1], Françoise J. Siepel[3], Alida F. W. van der Steeg[1]

[1] Department for Pediatric Surgery, Princess Máxima Center for Pediatric Oncologic, Utrecht, The Netherlands.
[2] Technical Medicine, TechMed Centre, University of Twente, Enschede, The Netherlands.
[3] Robotics and Mechatronics, TechMed Centre, University of Twente, Enschede, The Netherland.

PURPOSE

Surgical treatment of pediatric chest wall tumors is complex. Due to the highly malignant nature of these tumors, complete tumor resection with a wide tumor margin is the main goal of surgery. However, the inevitable removal of multiple ribs can lead to significant chest wall deformities that negatively affect respiration, mobilization and aesthetics. Consequently, to achieve radical resection while still sparing as much healthy tissue as possible, pediatric chest wall resections require meticulous surgical planning and accurate tumor localization. However, tumor localization can be difficult as these tumors have often become invisible and non-palpable due to neoadjuvant chemotherapy. Surgical decision making is currently based on multiple two-dimensional (2D) imaging modalities, palpation and thoracoscopy prior to resection. Subsequently, by using solely 2D imaging, the three-dimensional (3D) perception and anatomical relation of the tumor greatly depend on the surgeon's spatial interpretation.

The use of intraoperative 3D guidance, e.g. Augmented Reality (AR), could overcome these challenges and significantly improve surgical planning and anatomical understanding, thereby facilitating surgical decision making. After a first introduction of an AR system by Spijkerboer et al. [1], we have used the HoloLens 2 (Microsoft Corporation, Redmond, WA, USA) to intraoperatively localize chest wall tumors of five patients treated in our center. We present our early experience with this system and discuss the feasibility of AR guidance for the surgical localization of pediatric chest wall tumors.

METHODS

From the first of January 2021 to the end of 2022, a total of five pediatric patients underwent surgical resection of a chest wall tumor in the Princess Máxima Center (Utrecht, The Netherlands) (Table 1). For all patients, a patient-specific 3D model was created by segmenting the tumor and relevant anatomy from preoperative computed tomography (CT) images. Segmentation was done by technical physicians specifically trained in Ewing sarcoma delineation together with the performing surgeon (CvdV). Finally, the model was projected onto the patient in the operating room (OR) by a five-point registration method based on anatomical landmarks.

The preoperative CT scan was performed with the patients lying in the surgical lateral decubitus position. During this scan, five 1.5 mm radiopaque skin markers (Suremark®, Mesa, AZ, USA) were attached to recognizable landmarks such as scars, birthmarks, or the nipple. The tumor, adjacent ribs, five landmarks and involved anatomical structures were segmented from the CT images and the 3D model was integrated into the HoloLens 2 application in Unity (Unity Technologies, San Francisco, CA, USA).

Registration was performed pre-incisional by using a 3D printed pointer with a quick response (QR) code recognized by the HoloLens 2. A reference QR code was attached onto the patient to enable a stable visualization and adjust for respiratory movement. During registration, the surgeon pinpointed

the anatomical landmarks and voice commands were used to save the real 3D position of each point. Subsequently, a Procrustes algorithm computed the most accurate transformation of the virtual 3D model onto the patient and the holographic overlay was realized. A more extensive explanation of the used method is described by Spijkerboer et al. [1]

Patient	Sex	Age (y) Median = 7	Tumor	Resected ribs	Neoadjuvant chemotherapy	Diagnostic tumor measurements (AP x RL x CC) (cm)	Preoperative tumor measurements (AP x RL x CC) (cm)
1	F	6	Ewing sarcoma	1 (7th)	Yes	11.2 x 14.9 x 19.9	4.6 x 2.5 x 5.9
2	M	12	Ewing sarcoma	3 (8th - 10th)	Yes	5.9 x 5.4 x 7.4	5.8 x 1.3 x 4.5
3	M	7	Ewing sarcoma	3 (8th - 10th)	Yes	4.6 x 6.4 x 5.6	4.4 x 3.3 x 1.6
4	M	2	Ewing sarcoma	1 (7th)	Yes	5.0 x 3.0 x 5.0	2.6 x 1,8 x 1.1
5	M	13	Mesenchymal chondrosarcoma	3 (5th – 7th)	No	9.1 x 7.1 x 7.6	9.1 x 7.1 x 7.4

Table 1: Patient characteristics

RESULTS

Registration and holographic overlay was achieved in all five patients. Figure 1 shows the results of the AR-guided tumor localization in one case. The pre-incisional holographic overlay appeared to be accurate for most patients, though it is difficult to quantify misalignments of the holographic overlay since it is unclear which localization is to be kept as ground truth. In some cases, minor disagreements between the overlay and expected tumor location based on the conventional localization methods were found. Moreover, the system was unable to maintain a correct projection of the 3D model once the skin had been opened. Lastly, as the chest wall generally lacks the presence of distinguishable and rigid landmarks, the five-point registration method proved to be prone to inaccuracies and user-dependent errors. The holographic overlay seemed most accurate when the five-landmarks were positioned in a non-symmetric configuration in proximity to the tumor.

Figure 1: Holographic overlay of the 3D model including the tumor, ribs, lung and anatomical landmarks (purple spheres). The reference QR code is fixated on the patient's hip. Note that there

can be an apparent misalignment between patient and hologram due to the displacement between the camera and surgeon's line of sight.

CONCLUSION

Our results prove the further applicability of AR guidance for the pre-incisional localization of pediatric chest wall tumors during surgery. The system has the potential to enable intraoperative 3D visualization, hereby facilitating surgical planning and management of chest wall resections. Misalignments of the holographic overlay may be due to insufficient tracking of the reference QR code or inaccurate landmark selection during registration. Therefore, we are currently exploring the feasibility of different registration methods, such as surface matching. Moreover, as it remains difficult to quantify misalignments of the hologram within our current workflow, we are working on methods to measure our system's accuracy and to validate its performance.

REFERENCES

[1] Spijkerboer, Fitski, Siepel, van de Ven, van der Steeg (2022) Augmented reality-guided localization of a chest wall tumor in a pediatric patient. European Journal of Cancer 170: 103-105

Appendix C: PLUS Server Configuration File

```xml
<PlusConfiguration version="2.1">
  <DataCollection StartupDelaySec="1.0" >
    <DeviceSet
      Name="PlusServer: NDI Vega tracker with passive markers - by IP - Adjusted - M3 Thesis"
      Description="Broadcasting tool tracking data through OpenIGTLink
For NDI Vega: Tool (8700339), Stylus (8700340), Reference (8700449)" />
    <Device
      Id="TrackerDevice"
      Type="PolarisTracker"
      SerialPort = "3"
      NetworkHostname="P9-03812"
      AcquisitionRate = "120"
      NetworkPort="8765"
      ToolReferenceFrame="Tracker" >
      <DataSources>
        <DataSource Type="Tool" Id="Probe" RomFile="NdiToolDefinitions/8700449- Polaris
Passive 4-Marker Rigid Body 3.rom"  />
        <DataSource Type="Tool" Id="Stylus" RomFile="NdiToolDefinitions/8700340- Polaris
Passive 4-Marker Probe.rom"  />
        <DataSource Type="Tool" Id="RefPatient" RomFile="NdiToolDefinitions/8700339- Polaris
Passive 4-Marker Rigid Body 2.rom"  />
        <DataSource Type="Tool" Id="RefModel" RomFile="NdiToolDefinitions/APPLE01.rom"  />

      </DataSources>
      <OutputChannels>
        <OutputChannel Id="TrackerStream" >
          <DataSource Id="Probe"/>
          <DataSource Id="Stylus"/>
          <DataSource Id="RefPatient"/>
          <DataSource Id="RefModel"/>
        </OutputChannel>
      </OutputChannels>
    </Device>


    <Device
      Id="VideoDevice"
      Type="MmfVideo"
      FrameSize="640 480"
      VideoFormat="YUY2"
      AcquisitionRate = "100"
      CaptureDeviceId = "1" >
      <DataSources>
        <DataSource Type="Video" Id="Video" PortUsImageOrientation="MN"
        ClipRectangleOrigin="175 40"
      ClipRectangleSize="250 300"/>
      </DataSources>
      <OutputChannels>
        <OutputChannel Id="VideoStream" VideoDataSourceId="Video" />
      </OutputChannels>
    </Device>

    <Device
      Id="CaptureDevice"
      Type="VirtualCapture"
      BaseFilename="RecordingTest.igs.nrrd"
      EnableFileCompression="TRUE"
      EnableCapturingOnStart="TRUE" >
      <InputChannels>
        <InputChannel Id="TrackerStream" />
      </InputChannels>
    </Device>

<!--      <Device
      Id="CaptureDevice"
      Type="VirtualCapture"
      BaseFilename="RecordingTest.igs.mha"
      EnableCapturingOnStart="FALSE" >
      <InputChannels>
        <InputChannel Id="VideoStream" />
          <InputChannel Id="TrackerStream" />
```

```xml
          </InputChannels>
        </Device>
        -->
   </DataCollection>
   <CoordinateDefinitions>
     <Transform From="Image" To="Reference"
      Matrix="
        1 0 0 0
        0 1 0 0
        0 0 1 0
        0 0 0 1"
       Error="0.554951" Date="012617_105449" />
     <Transform From="StylusTip" To="Stylus"
      Matrix="
        1 0 0.000203823 0.0180449
        3.31529e-09 -1  -1.62655e-05  -0.00144002
        0.000203823 1.62655e-05 -1  -88.5321
        0 0 0 1"
       Error="0.554951" Date="012617_105449" />

     <CoordinateDefinitions>
     <Transform From="Image" To="Reference"
      Matrix="
        1 0.0 0.0 0.0
        0.0 1 0.0 0.0
        0.0 0.0 1 0.0
        0 0 0 1" />
   </CoordinateDefinitions>

   </CoordinateDefinitions>
   <PlusOpenIGTLinkServer
     MaxNumberOfIgtlMessagesToSend="1"
     MaxTimeSpentWithProcessingMs="50"
     ListeningPort="18944"
     SendValidTransformsOnly="true"
     OutputChannelId="TrackerStream" >
     <DefaultClientInfo>
       <MessageTypes>
         <Message Type="TRANSFORM" />
       </MessageTypes>
       <TransformNames>
         <!-- <Transform Name="StylusTipToReference" /> -->
         <Transform Name="ProbeToTracker" />
         <!-- <Transform Name="ProbeToReference" /> -->
         <Transform Name="StylusToTracker" />
         <Transform Name="RefPatientToTracker" />
         <Transform Name="RefModelToTracker" />
       </TransformNames>
     </DefaultClientInfo>
   </PlusOpenIGTLinkServer>

   <PlusOpenIGTLinkServer
     MaxNumberOfIgtlMessagesToSend="1"
     MaxTimeSpentWithProcessingMs="50"
     ListeningPort="18945"
     SendValidTransformsOnly="true"
     OutputChannelId="VideoStream" >
     <DefaultClientInfo>
       <MessageTypes>
         <Message Type="IMAGE" />
       </MessageTypes>
       <ImageNames>
         <Image Name="Image" EmbeddedTransformToFrame="Reference" />
       </ImageNames>
     </DefaultClientInfo>
   </PlusOpenIGTLinkServer>

</PlusConfiguration>
```

Appendix D: 3D Slicer Protocol Experiment

Probe kalibratie:

1. Voor een pivot calibratie uit voor de volgende kalibratie: StylusTip→StylusTipToStylus. Dit brengt de tip van de stylus naar het stylus coordinatensysteem.
2. Nu hang je de referentie van het model aan de stylus. In dit geval wordt de stylus uitgedrukt in het coordinatensysteem van het model. Daarvoor voer je twee stappen uit:
    a. Bereken via TransformProcessor de actuele inverse van de ProbeToTracker uit. Hiermee berekent hij continu de TrackerToProbe uit.
    b. TrackerToProbe →StylusTip→StylusTipToStylus
    Aan ImageReference hang je nog niks te hangen.
3. Nu wil je de fiducial registratie uitvoeren om de registratie te doen van het model coordinaten naar de tracking coordinaten:
    a. From: ImageFiducials
    b. To: TrackingFiducials
    c. Transform: ImageToProbe
4. Nu haal je de TrackerToProbe van de stylus af. Dit zorgt ervoor dat de stylus weer in het tracking systeem komt te staan.
5. Nu moet je zorgen dat het model zijn transformatie krijgt naar het tracking systeem. Hiervoor moet je twee transformatie eraanhangen, namelijk vanuit het model naar lokaal tracking naar tracking systeem.

Creeëren Scene tbv navigatie experiment

1. Importeer de CT & NDI Reference Frame
2. Kleur in een aantal slices gebieden met bot en achtergrond en voer de 'Grow from Seeds' uit. Je creeërt zodoende het bot 3D model.
3. Zoek in de CT de pivot punten van het NDI Reference Frame (RigidBodyPoints_Image) en zoek ze ook in het model op (RigidBodyPoints_Model).
4. Voer een puntenregistratie van het model naar de image uit om zo het NDI Reference Frame naar de juiste locatie in de CT te transformeren. Check middels de 2D overlay of de positie goed is en pas zo nodig aan.
5. Merge zowel het botmodel als het NDI Reference Model en exporteer het geheel als .stl.
6. Importeer het gecreeërde model in MeshMixer en plaats de origin in het centrum van het NDI Reference Frame en exporteer weer als .st. voor de import in je Slicer Scene.
7. Je wilt nu je CT naar het nieuwe botmodel transformeren. Je hebt nu het botmodel plus CT op de oude locatie en een op de nieuwe locatie. Volg onderstaande stappen:
    a. Zoek nogmaals de pivot punten uit het NDI Reference Frame op in het nieuwe model (RigidBodyPoints_Model_new)
    b. Maak een transformatie van ImageToModelNew waarbij je zowel de CT als het oude botmodel naar het nieuwe botmodel transformeert.
    c. Harden het oude botmodel en de CT.
    d. Voer een kleine correctie uit genaamd ModelToModelNew. Hiervoor is je getransformeerde oude botmodel moving en je nieuwe botmodel fixed.
    e. Hang ModelToModelNew aan je CT en harden deze vervolgens. Het oude botmodel kan nu verwijderd worden.
8. Creeër de volgende pivot punten om je PointRegistration genaamd ModelToModelRef uit te voeren:
    a. Pivotpunten NDI Reference Frame
    b. Schroefgaten op plastic reference frame
    c. Distale schroeven op zowel het distale uiteinde of de insertie plaats in bot.
9. Creeër de surgicaltargets, tumor, osteotomievlakken etc.

10. Kopieer nu alle 3D modellen zodat je alle modellen in zowel US coordinaten als CT coordinaten kan weergeven.

iUS 3D volume reconstructive en registratie

Ook hier wil je alles omschrijven in tracking coordinaten.

1. Voer je US calibratie uit en creëer de ImageToProbe transformatie. Deze hang je uiteindelijk ProbeToTracker aan je ImageReference.
2. Creëer de inverse van je PatientToTracker genaamd TrackerToPatient.
3. Hang TrackerToPatient aan je ImageReference om zodoende beeld op te nemen in de trackingcoordinaten van je patient.
4. Creëer het botvolume in het patientenframe en maak er een model van.
5. Exporteer het model in Meshlab, verfijn het oppervlak en reduceer de mesh.
6. Importeer het model en hang de transform 'PatientToTracker' aan. Je US segmentatie staat nu aan de trackingscoordinaten
7. Haal TrackerToPatient van je ImageReference af en hang er ProbeToTracker aanvast.
8. Voer nu een 'pre-registratie' uit op basis van punten die je vind op de US. Wijs de punten aan en hang vervolgens TrackerToPatient aan je punten, harden ze en creëer je transformatie.
9. Voer nu de modelregistratie uit en vervang je preregistratie met die. PatientRefToPatient

Handleiding validatie intraoperatieve navigatie:

1. Introductie mbv presentatie
2. Plaats de K-draden in het distale tibia met de K-draden richting distaal om zodoende ruimte te houden voor de US probe
3. Gouden standaard registratie:
    a. Plaats de reflecterende balletjes op je model
    b. Creëer de inverse van RefModelToTracker genaamd TrackerToRefModel via TransformProcessor
    c. Wijs de volgende 'To' punten aan met de stylus in TrackerToRefModel coordinaten:
        i. Fiducials rigid body
        ii. Schroefkoppen 'K-draden'
        iii. Schroefkop distale tibia (als deze niet zichtbaar is op de scan, dan snijd je weefsel weg tot je het insertie punt vind)
    d. De 'from' punten vind je vanuit de voorbereiding
    e. Fiducial registration om zo de ModelToRefModel te berekenen
    f. Haal de TrackerToRefModel van de Stylus af en hang ModelToRefModel incl. RefModelToTracker aan je model
4. US Sweep:
    a. Bereken de inverse van PatientRefToTracker genaamd TrackerToPatientRef via TransformProcessor
    b. Hang aan je ImageReference: ImageToProbe->ProbeToTracker->TrackerToPatientRef
    c. Creëer een sequence met: ImageReference, TrackerToPatientRef & ProbeToTracker
    d. Voer een US Sweep uit op de vlakke delen, heel langzaam. Let op, hij neemt maar 10 frames per seconden op!
    e. Sla de sequences & het patientmodel op in de map, sluit de huidige scene
5. 3D Volume Reconstruction & registratie in nieuwe scene
    a. Importeer de sequences, Patientmodel & ImageToProbe in een losse Slicer Scene
    b. Hang via de sequence module de TrackerToPatienRef en ProbeToTracker sequences aan je ImageReference sequence
    c. Bepaal het 3D volume via 3D volume Reconstruction
    d. Pre-registratie
        i. Klik in je US beeld een paar punten op het bot model aan: 'To'
        ii. Wijs deze punten ook aan in je originele model: 'From'
        iii. Bereken een transformatie: Pre-Registratie

iv. Harden deze transformatie, het patientmodel zit nu in de patientRef coordinaten
   e. Segmenteer het volume via Treshholding
   f. Exporteer als STL en verwijder de segmentatie uit de scene
   g. Importeer het STL in Meshlab en reduceer het
   h. Maak het Tibia model 'passend'
   i. Voer nu de modelregistratie en bereken PatientToPatientRef met US segmentatie als fixed en je Tibia model als Moving.

6. Importeer PatientToPatientRef en botsegmentatie in je main scene
   a. Hang nu je TrackerToPatientRef aan je botsegmentatie en patient_model
   b. Hang via TrackerToPatient de PatientToPatientRef aan je PatientModel_US
   c. Dit alles bevindt zich nu in het PatienRef domein

7. Zet de sequence aan voor tijdens het experiment!! (StylusToReference, ProbeToReference ,ModelRefToReference, PatientRefToReference) Let op dat je ook 'save changes' aan hebt staan.

8. Chirurgische punten aanwijzen
   a. **Let op dat je via TransformProcessor je de TrackerToModel aan hebt staan**
   b. **Let op dat je via 'Volume Reslice Driver' je de CT met de styluspunt goed hebt gekoppeld, dus ook in het juiste coordinaten frame (CT of US)**
   c. Navigeer naar het punt toe
   d. Hang de ModelToTracker aan je punten
   e. Moment dat je bent 'gearriveerd' hang je TrackerToModel aan de stylus
   f. Wijs het punt aan of harden de transform
   g. Je definieert nu de punten aangewezen met de nieuwe needle in model coordinaten

9. Osteotomievlak aanwijzen
   a. Hang TrackerToPatientRef aan je stylusToTracker
   b. Navigeer naar het punt toe
   c. Hang de ModelToTracker aan je punten
   d. Moment dat je bent 'gearriveerd' klik je het punt aan via de Fiducial Wizzard module of je hardend het model en hangt er ModelToTracker aan

10. Save data scene

Appendix E: Different US parameters

(a) 7 MHz

(b) 11 MHz

(c) 14 MHz

Bone segmentation image 10

(d) 7 MHz

Bone segmentation image 12

(e) 11 MHz

Bone segmentation image 11

(f) 14 MHz

(g) DR = 30

(h) DR = 50

(i) DR = 70

(j) DR = 90

Bone segmentation image 19

(k) DR = 30

Bone segmentation image 17

(m) DR = 50

Bone segmentation image 15

(n) DR = 70

Bone segmentation image 13

(o) DR = 90

(p) -20 dB

(q) -10 dB

(r) +10 DB

(s) +20 dB

Bone segmentation image 27

(t) -20 dB

Bone segmentation image 25

(u) -10 dB

Bone segmentation image 23

(v) +10 dB

Bone segmentation image 21

(w) +20 dB

Figure 37: Effect of different UL parameters on image quality and segmentation

Appendix F: Conventional Segmentation Methods
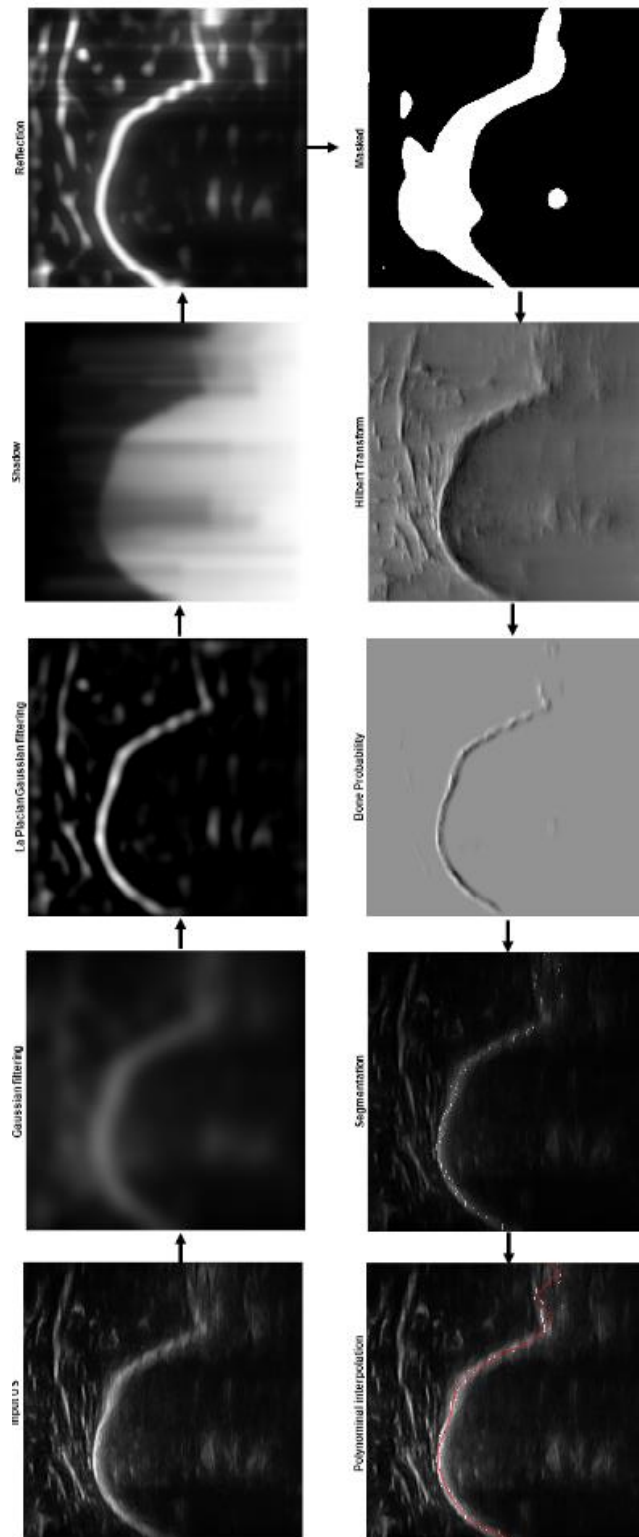
Figure 38: Bone probability segmentation using a phase-based approach for automatic bone segmentation

Appendix G: Rotational Performance
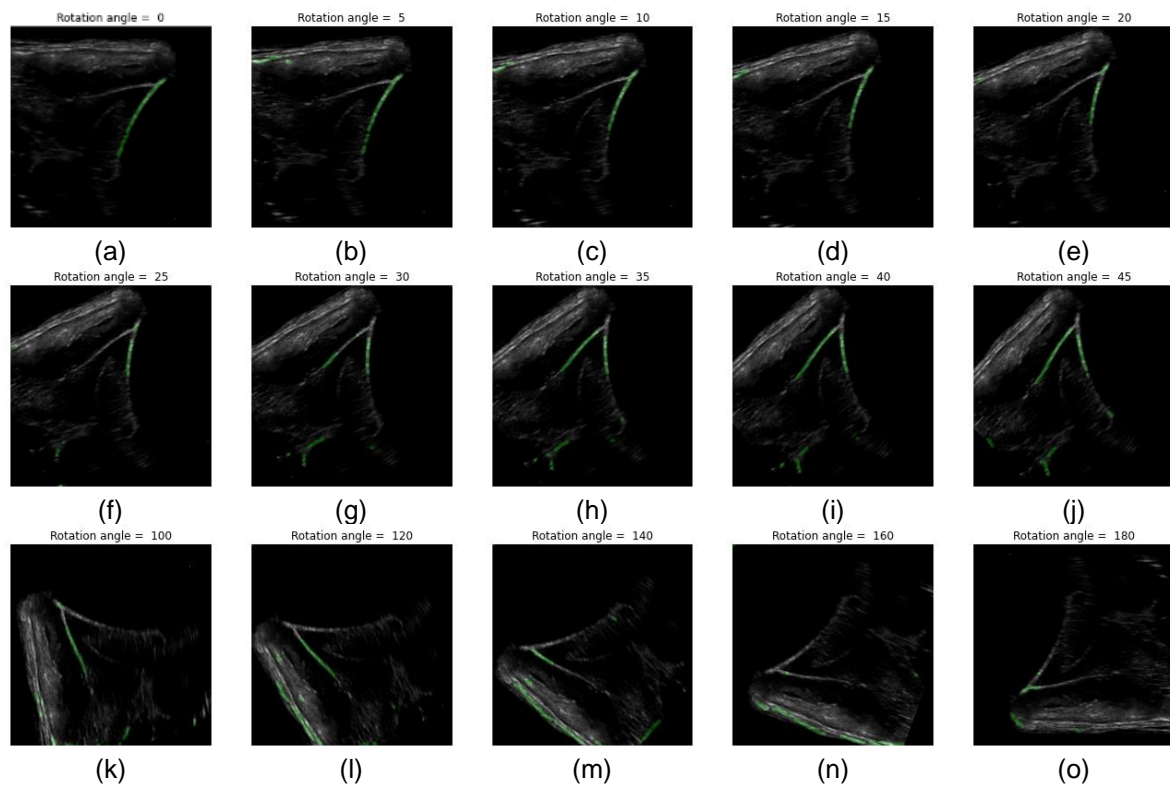
Figure 39: Effect of rotation on the performance of the network. (a-j) Rotation angle increases from 0 up to 45^0 degrees until (o) a vertical flip, 180^0 angle, was derived.

Appendix H: Hyperparameters

(a) Different learning rates

(b) Different learning rates

(c) Different batch sizes

(d) Different batch sizes

(e) Different epoch and batch sizes

(f) Different epoch and batch sizes
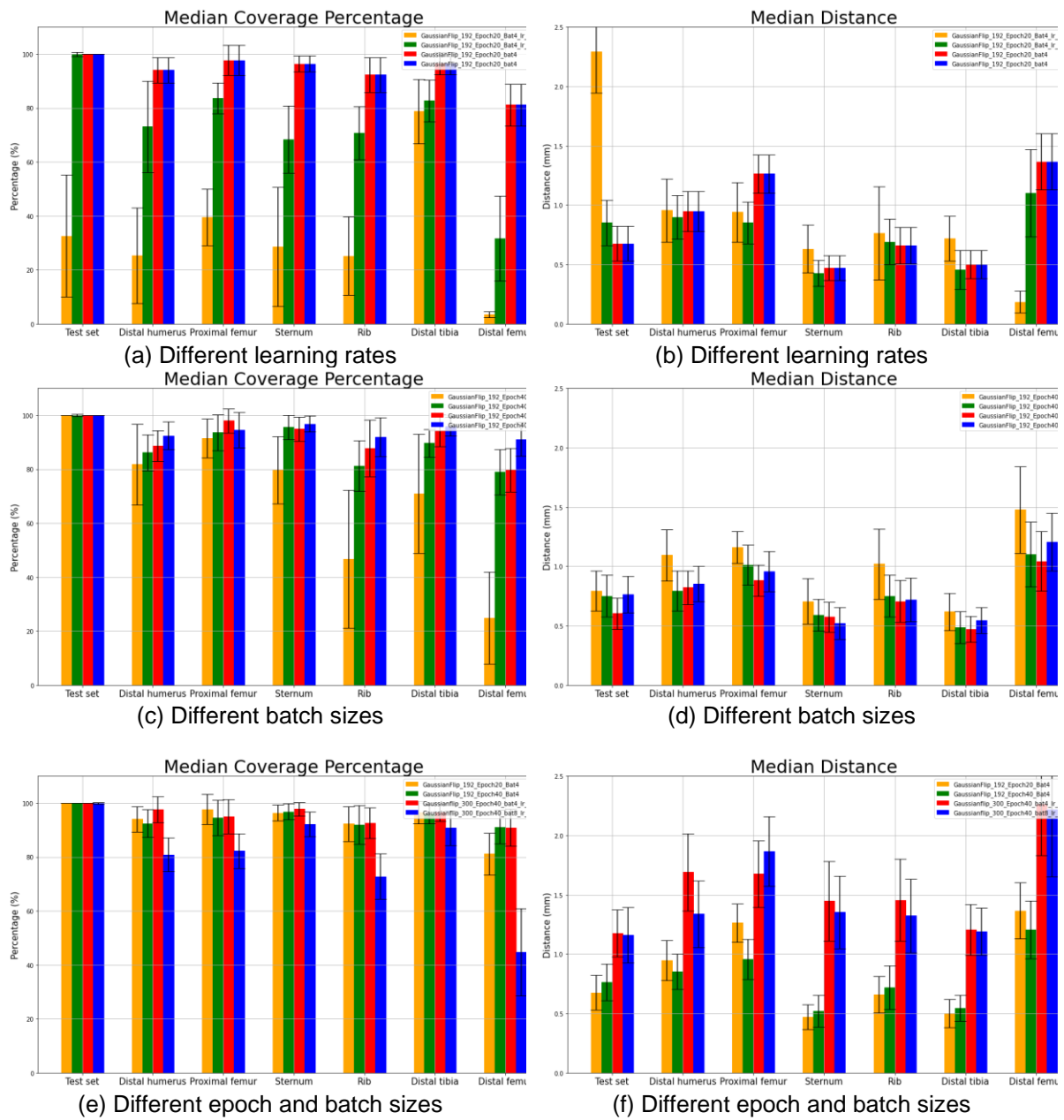
Figure 40: Effect of different hyperparameters

Appendix I: TRE Results

Table 13: Target Registration Errors per cadaver per surgical target

	Cadaver 1	Cadaver 2	Cadaver 3	Cadaver 4	Cadaver 5	Cadaver 6	Cadaver 7	Cadaver 8	Cadaver 9	
Point 1	2.60	16.80	7.10	7.10	9.60	17.00	9.70	7.60	3.20	
Point 2	2.70	15.60	7.40	5.10	10.50	21.30	7.90	8.10	2.30	
Point 3	1.70	15.00	6.60	4.80	9.50	17.00	6.60	7.60	2.40	
Point 4	0.50	12.40	7.20	3.40	9.00	18.70	8.70	8.60	2.30	
Point 5	1.30	12.50	6.60	4.00	8.80	17.40	7.30	8.80	2.40	
Point 6	1.00	8.70	8.00	2.30	8.70	13.70	5.80	9.80	2.30	
Point 7	2.80	11.80	6.90	2.80	8.70	15.80	5.00	9.40	2.00	
Point 8	1.50	13.30	8.00	2.70	8.40	12.50	5.10	9.80	2.50	
Point 9	1.50	9.80	7.30	3.80	8.40	15.20	7.80	10.70	2.90	
Point 10	ND	16.80	8.50	6.90	8.90	13.20	6.90	10.30	1.90	**ALL**
Mean	1.73	13.27	7.36	4.29	9.05	16.18	7.08	9.07	2.42	7.83
Std	0.76	2.64	0.60	1.60	0.62	2.55	1.44	1.04	0.37	0.79
Max	2.80	16.80	8.50	7.10	10.50	21.30	9.70	10.70	3.20	21.30
Min	0.50	8.70	6.60	2.30	8.40	12.50	5.00	7.60	1.90	0.50
P-Value	0.44	0.60	0.46	0.27	0.09	0.83	0.87	0.56	0.26	

Table 14: Target Registration Errors cumulative for each surgical target and in order of the experiment

	Mean	Std	Max	min	P-value
Point 1	8.97	4.64	17.00	2.60	0.19
Point 2	8.99	5.60	21.30	2.30	0.27
Point 3	7.91	4.79	17.00	1.70	0.36
Point 4	7.87	5.14	18.70	0.50	0.62
Point 5	7.68	4.64	17.40	1.30	0.70
Point 6	6.70	3.85	13.70	1.00	0.53
Point 7	7.24	4.21	15.80	2.00	0.51
Point 8	7.09	4.02	13.30	1.50	0.44
Point 9	7.49	3.92	15.20	1.50	0.84
Point 10	9.18	3.36	16.80	1.90	0.71

Figure 41: Mean target registration errors from proximal to distal.

Appendix J: PLE-1 Results

Table 15: PLE-1 per cadaver per surgical target

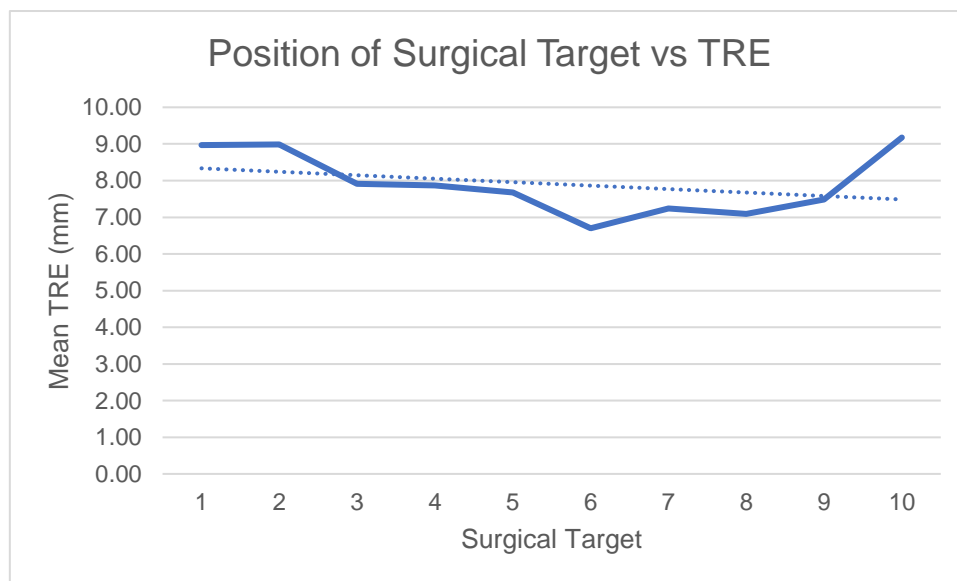|	Cadaver 1	Cadaver 2	Cadaver 3	Cadaver 4	Cadaver 5	Cadaver 7	Cadaver 8	Cadaver 9	
Point 1	12.90	22.40	13.70	19.60	8.00	7.50	18.20	6.00	
Point 2	17.00	16.00	10.30	9.50	8.70	3.80	15.30	6.30	
Point 3	15.70	18.00	21.40	9.10	9.40	7.40	14.40	5.00	
Point 4	10.20	9.30	11.30	11.90	7.80	2.60	10.00	9.30	
Point 5	11.80	13.00	9.60	8.70	9.40	4.30	8.60	6.40	
Point 6	14.80	10.40	13.70	5.40	9.80	7.00	8.90	4.10	
Point 7	18.20	15.40	10.90	5.10	8.80	5.80	5.10	7.60	
Point 8	11.30	16.50	15.40	8.40	11.20	4.60	2.70	6.10	
Point 9	14.80	12.10	15.40	3.10	9.30	6.40	13.70	6.50	
Point 10	14.80	12.10	11.60	17.30	8.80	3.00	5.90	3.80	**All**
P-value	0.81	0.73	0.10	0.31	0.44	0.38	0.85	0.58	ND
median	14.80	14.20	12.65	8.90	9.05	5.20	9.45	6.20	9.25
Q1	11.68	11.68	10.75	5.33	8.53	3.60	5.70	4.78	4.91
Q3	16.03	16.88	15.40	13.25	9.50	7.10	14.63	6.78	13.81
IQR	4.35	5.20	4.65	7.93	0.98	3.50	8.93	2.00	8.90
Max	18.20	22.40	21.40	19.60	11.20	7.50	18.20	9.30	14.80
Min	10.20	9.30	9.60	3.10	7.80	2.60	2.70	3.80	5.20

Table 16: PLE-1 cumulative for each surgical target and in order of the experiment

|	P-value	Median	Q1	Q3	IQR	Max	Min
Point 1	0.67	13.30	7.63	19.25	11.63	22.40	6.00
Point 2	0.72	9.90	6.90	15.83	8.93	17.00	3.80
Point 3	0.48	11.90	7.83	17.43	9.60	21.40	5.00
Point 4	0.04	9.65	8.18	11.03	2.85	11.90	2.60
Point 5	0.79	9.05	6.95	11.25	4.30	13.00	4.30
Point 6	0.62	9.35	5.80	12.88	7.08	14.80	4.10
Point 7	0.24	8.20	5.28	14.28	9.00	18.20	5.10
Point 8	0.54	9.80	4.98	14.38	9.40	16.50	2.70
Point 9	0.31	10.70	6.43	14.53	8.10	15.40	3.10
Point 10	0.77	10.20	4.33	14.13	9.80	17.30	3.00
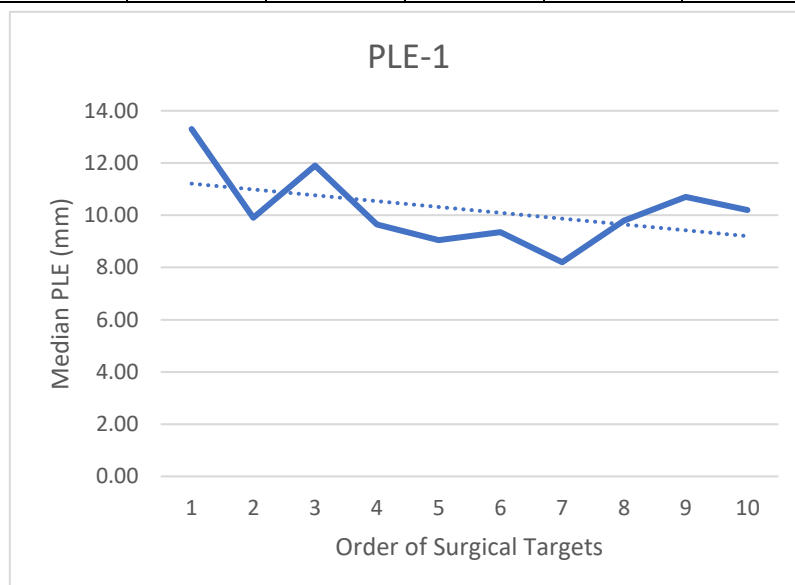
Figure 42: PLE-1 for each surgical target in order of the experiment

Appendix K: PLE-1 Results [Improved]

Table 17: PLE-1 after improvements per cadaver per surgical target

	Cadaver 1	Cadaver 2	Cadaver 3	Cadaver 4	Cadaver 5	Cadaver 7	Cadaver 8	Cadaver 9	
Point 1	6.60	22.40	11.60	16.80	8.00	7.50	13.40	7.70	
Point 2	12.50	16.00	8.10	8.70	8.70	3.80	12.50	6.00	
Point 3	11.30	18.00	19.10	7.40	9.40	7.40	11.10	4.90	
Point 4	5.50	9.30	7.50	10.10	7.80	2.60	7.30	8.60	
Point 5	5.60	13.00	6.40	5.60	9.40	4.30	4.50	5.70	
Point 6	8.00	10.40	9.30	3.50	9.80	7.00	4.00	4.40	
Point 7	11.00	15.40	7.40	3.90	8.80	5.80	3.30	6.90	
Point 8	4.30	16.50	10.20	8.60	11.20	4.60	1.50	5.60	
Point 9	10.90	12.10	10.00	3.90	9.30	6.40	9.50	7.60	
Point 10	8.00	12.10	7.00	12.90	8.80	3.00	3.70	2.60	**All**
P-value	0.36	0.73	0.01	0.32	0.44	0.38	0.28	0.93	ND
median	8.00	14.20	8.70	8.00	9.05	5.20	5.90	5.85	8.00
Q1	5.58	11.68	7.30	3.90	8.53	3.60	3.60	4.78	3.68
Q3	11.08	16.88	10.55	10.80	9.50	7.10	11.45	7.63	8.96
IQR	5.50	5.20	3.25	6.90	0.98	3.50	7.85	2.85	5.29
Max	12.50	22.40	19.10	16.80	11.20	7.50	13.40	8.60	14.20
Min	4.30	9.30	6.40	3.50	7.80	2.60	1.50	2.60	5.20

Table 18: PLE-1 after improcements cumulative for each surgical target and in order of the experiment

|	P-value	Median	Q1	Q3	IQR	Max	Min
Point 1	0.26	9.80	7.55	15.95	8.40	22.40	6.60
Point 2	0.77	8.70	6.53	12.50	5.98	16.00	3.80
Point 3	0.14	10.25	7.40	16.33	8.93	19.10	4.90
Point 4	0.01	7.65	5.95	9.13	3.18	10.10	2.60
Point 5	0.02	5.65	4.78	8.65	3.88	13.00	4.30
Point 6	0.48	7.50	4.10	9.68	5.58	10.40	3.50
Point 7	0.78	7.15	4.38	10.45	6.08	15.40	3.30
Point 8	0.74	7.10	4.38	10.95	6.58	16.50	1.50
Point 9	0.95	9.40	6.70	10.68	3.98	12.10	3.90
Point 10	0.37	7.50	3.18	11.28	8.10	12.90	2.60
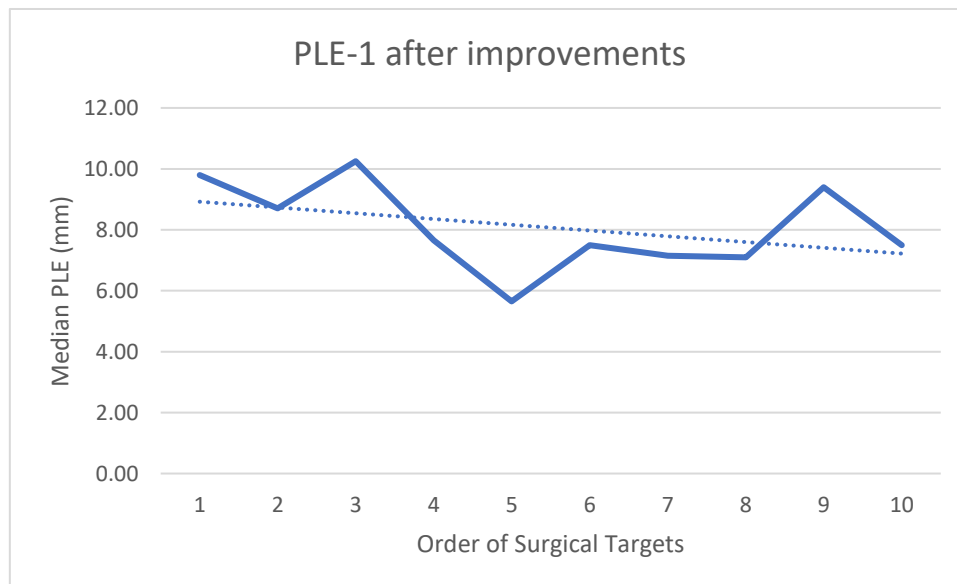
Figure 43: PLE-1 after improvements for each surgical target in order of the experiment

Appendix L: PLE-2 Results

Table 19: PLE-1 per cadaver per surgical target

	Cadaver 1	Cadaver 2	Cadaver 3	Cadaver 4	Cadaver 5	Cadaver 7	Cadaver 8	Cadaver 9	
Point 1	5.10	5.60	6.60	11.90	6.90	6.00	8.80	2.40	
Point 2	11.00	6.20	3.50	10.50	4.60	6.10	5.90	3.00	
Point 3	10.40	13.30	18.90	8.80	2.80	5.80	6.60	2.10	
Point 4	5.90	4.00	0.70	7.30	6.30	5.60	3.30	4.80	
Point 5	4.90	4.10	4.20	8.50	4.00	6.80	6.80	5.50	
Point 6	7.00	4.20	4.80	4.50	1.80	4.70	7.80	0.80	
Point 7	9.30	13.60	5.00	3.40	1.20	8.50	9.40	4.60	
Point 8	3.20	7.00	2.60	5.00	3.00	5.00	8.70	2.50	
Point 9	10.50	7.00	3.70	4.40	2.70	6.90	2.40	2.20	
Point 10	7.00	1.60	0.40	9.10	2.90	2.60	6.20	2.20	**All**
P-value	0.41	0.08	0.00	0.51	0.36	0.75	0.36	0.23	ND
median	7.00	5.90	3.95	7.90	2.95	5.90	6.70	2.45	5.90
Q1	5.05	4.08	2.13	4.48	2.48	4.93	5.25	2.18	2.25
Q3	10.43	8.58	5.40	9.45	5.03	6.83	8.73	4.65	6.93
IQR	5.38	4.50	3.28	4.98	2.55	1.90	3.48	2.48	4.68
Max	11.00	13.60	18.90	11.90	6.90	8.50	9.40	5.50	7.90
Min	3.20	1.60	0.40	3.40	1.20	2.60	2.40	0.80	2.45

Table 20: PLE-2 cumulative for each surgical target and in order of the experiment

	P-value	Median	Q1	Q3	IQR	Max	Min
Point 1	0.74	6.30	5.23	8.33	3.10	11.90	2.40
Point 2	0.16	6.00	3.78	9.43	5.65	11.00	3.00
Point 3	0.80	7.70	3.55	12.58	9.03	18.90	2.10
Point 4	0.00	5.20	3.48	6.20	2.73	7.30	0.70
Point 5	0.25	5.20	4.13	6.80	2.68	8.50	4.00
Point 6	0.57	4.60	2.40	6.45	4.05	7.80	0.80
Point 7	0.87	6.75	3.70	9.38	5.68	13.60	1.20
Point 8	0.06	4.10	2.70	6.50	3.80	8.70	2.50
Point 9	0.06	4.05	2.48	6.98	4.50	10.50	2.20
Point 10	0.19	2.75	1.75	6.80	5.05	9.10	0.40

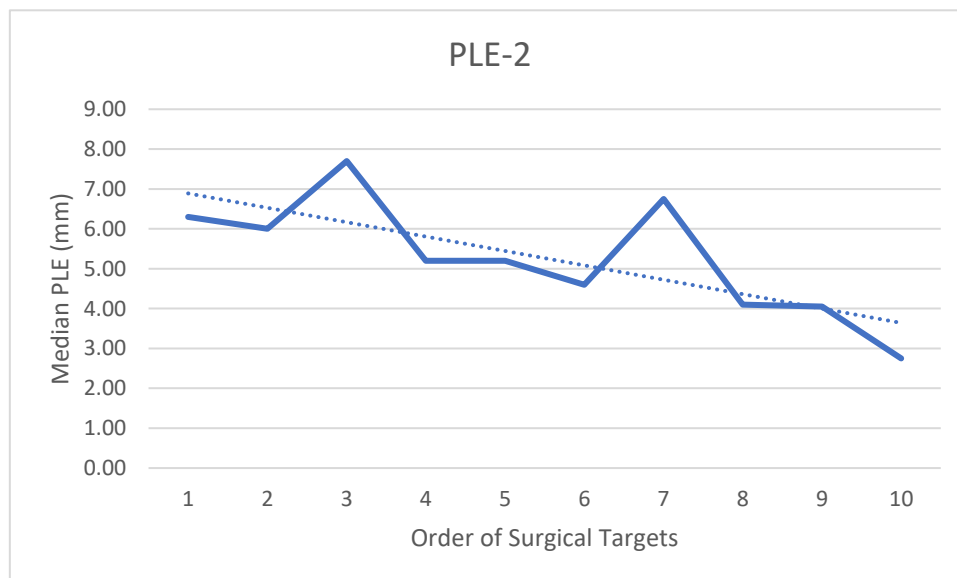Figure 44: PLE-2 for each surgical target in order of the experiment

Appendix M: PLE-3 Results

Table 21: PLE-1 per cadaver per surgical target

	Cadaver 4	Cadaver 5	Cadaver 6	Cadaver 7	Cadaver 8	Cadaver 9	
Point 1	5.60	6.10	7.70	5.20	7.50	3.90	
Point 2	5.70	2.40	4.60	3.90	2.60	2.50	
Point 3	6.70	3.00	8.30	4.00	1.70	3.20	
Point 4	9.90	5.00	5.20	3.50	0.90	2.60	
Point 5	6.60	3.30	7.30	1.40	2.90	2.30	
Point 6	5.50	2.50	3.90	4.70	15.70	3.80	
Point 7	4.10	2.00	4.10	2.60	5.70	2.00	
Point 8	9.20	2.00	9.60	4.30	2.40	1.70	
Point 9	10.20	3.10	2.60	1.50	2.80	2.90	
Point 10	5.60	2.80	5.70	5.80	10.80	3.80	**All**
p-value	0.10	0.03	0.83	0.60	0.03	0.45	ND
median	6.15	2.90	5.45	3.95	2.85	2.75	3.43
Q1	5.58	2.30	4.05	2.33	2.23	2.23	2.83
Q3	9.38	3.73	7.85	4.83	8.33	3.80	4.43
IQR	3.80	1.43	3.80	2.50	6.10	1.58	1.61
Max	10.20	6.10	9.60	5.80	15.70	3.90	15.70
Min	4.10	2.00	2.60	1.40	0.90	1.70	0.90

Table 22: PLE-3 cumulative for each surgical target and in order of the experiment

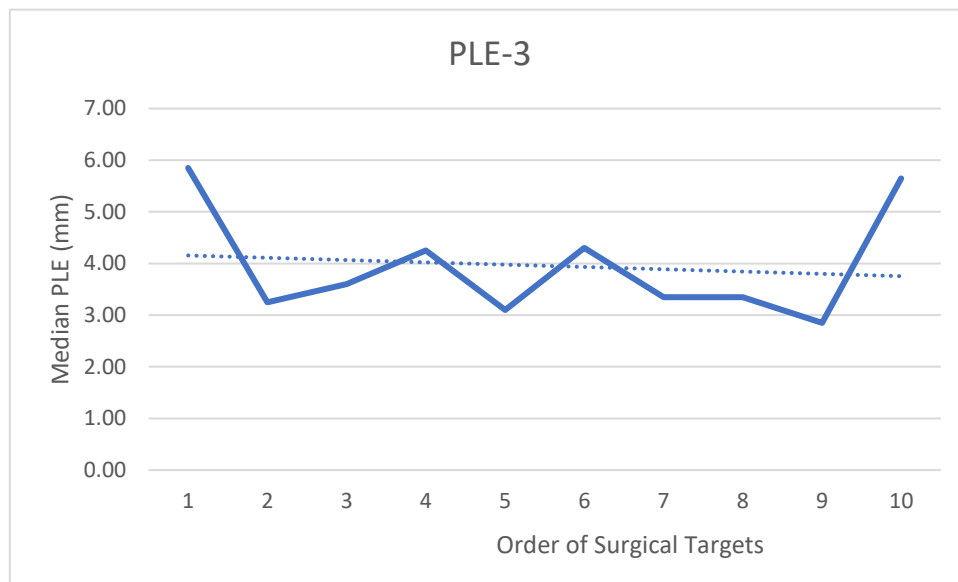|	P-value	Median	Q1	Q3	IQR	Max	Min
Point 1	0.72	5.85	4.88	7.55	2.68	7.70	3.90
Point 2	0.24	3.25	2.48	4.88	2.40	5.70	2.40
Point 3	0.47	3.60	2.68	7.10	4.43	8.30	1.70
Point 4	0.59	4.25	2.18	6.38	4.20	9.90	0.90
Point 5	0.25	3.10	2.08	6.78	4.70	7.30	1.40
Point 6	0.01	4.30	3.48	8.05	4.58	15.70	2.50
Point 7	0.31	3.35	2.00	4.50	2.50	5.70	2.00
Point 8	0.06	3.35	1.93	9.30	7.38	9.60	1.70
Point 9	0.00	2.85	2.33	4.88	2.55	10.20	1.50
Point 10	0.18	5.65	3.55	7.05	3.50	10.80	2.80

Figure 45: PLE-3 for each surgical target in order of the experiment